



HAL
open science

Electrochemiluminescence: from materials to new analytical strategies

Jing Yu

► **To cite this version:**

Jing Yu. Electrochemiluminescence: from materials to new analytical strategies. Other. Université de Bordeaux, 2022. English. NNT: 2022BORD0188 . tel-04187124

HAL Id: tel-04187124

<https://theses.hal.science/tel-04187124v1>

Submitted on 24 Aug 2023

HAL is a multi-disciplinary open access archive for the deposit and dissemination of scientific research documents, whether they are published or not. The documents may come from teaching and research institutions in France or abroad, or from public or private research centers.

L'archive ouverte pluridisciplinaire **HAL**, est destinée au dépôt et à la diffusion de documents scientifiques de niveau recherche, publiés ou non, émanant des établissements d'enseignement et de recherche français ou étrangers, des laboratoires publics ou privés.

THÈSE PRÉSENTÉE
POUR OBTENIR LE GRADE DE
**DOCTEUR DE
L'UNIVERSITÉ DE BORDEAUX**

ÉCOLE DOCTORALE
SPÉCIALITÉ CHIMIE-PHYSIQUE

Par Yu Jing

**Electrochemiluminescence: from materials to new analytical
strategies**

Sous la direction du Professeur Neso Sojic

Soutenue le 09/06/2022

Membres du jury:

Yanxia Hou-Broutin	Chargée de recherche CNRS, CEA, Université Grenoble Alpes	Rapporteur
Federico Polo	Professeur, Ca' Foscari University of Venice	Rapporteur
Gabriel Loget	Chargé de recherche CNRS, Institut des Sciences Chimiques de Rennes	Examineur
Nicolas Mano	Directeur de recherche CNRS, Centre de Recherche Paul Pascal	Examineur
Neso Sojic	Professeur, Bordeaux INP	Directeur de thèse

Résumé

La chimiluminescence électrogénérée, également appelée électrochimiluminescence (ECL), qui appartient à la famille des phénomènes de luminescence, fait intervenir des intermédiaires réactionnels produits électrochimiquement à la surface d'une électrode. Par une réaction de transfert d'électrons hautement exergonique, ils génèrent l'état excité du luminophore, qui retourne à l'état fondamental en émettant un photon. Ainsi, l'ECL est initiée par une étape électrochimique, se poursuit par une réaction chimique homogène et se termine par une étape photochimique. Cette combinaison de la chimiluminescence (CL) et de l'électrochimie présente de nombreux avantages potentiels, à savoir qu'elle ne nécessite pas de source de lumière externe, ni l'ajout de réactifs et élimine l'utilisation de réactifs toxiques ou corrosifs. Pour déclencher la génération de l'ECL, l'électrochimie offre un grand contrôle de la position de l'émission et du temps des réactions ECL. Le signal ECL est en général moins intense que la CL car la réaction se produit à proximité de la surface de l'électrode, et non au sein de la solution (« bulk »). Au cours des trois dernières décennies, l'ECL s'est développée rapidement et est devenue une technique puissante pour les immunodosages, les diagnostics cliniques, les tests environnementaux, la détection d'agents de guerre biologique et la visualisation de systèmes dynamiques.

Le chapitre 1 présente une vue générale de l'ECL dans le contexte de la luminescence et de l'électrochimie. Après une introduction historique, l'ECL et d'autres formes d'émission de lumière sont présentées dans leurs contextes respectifs. Ensuite, les principaux mécanismes d'annihilation et ceux impliquant un co-réactif, les luminophores organiques et inorganiques et les applications analytiques sont détaillés.

Dans le chapitre 2, le nouveau concept d'électrochimiluminescence photo-induite (ou P-ECL) est introduit pour la première fois avec deux types d'électrodes de semi-conducteurs de type n en utilisant des systèmes ECL modèles. La P-ECL combine la photoélectrochimie des semi-conducteurs (SC) avec l'ECL. L'émission ECL est déclenchée par des trous (h^+) photogénérés dans une électrode semi-conductrice de type n, qui peut produire une émission P-ECL à un faible potentiel anodique. Dans la première partie de ce chapitre, la P-ECL est générée sur des électrodes à base de Si, protégées par des films minces de SiO_x et de Ni de quelques nanomètres d'épaisseur, avec le système ECL modèle impliquant l'oxydation simultanée de $[Ru(bpy)_3]^{2+}$ et de la tri-n-propylamine (TPrA) dans l'eau.¹ Le système $[Ru(bpy)_3]^{2+}/TPrA$ nécessite classiquement des potentiels fortement anodiques supérieurs à +1 V vs ECS pour la génération de l'ECL. Cependant, le système développé à base de silicium repose sur un processus de conversion haute (ou « upconversion »). En effet, l'absorption de lumière à 810 nm induit une émission ECL (635 nm) à un faible potentiel électrochimique de

0,45 V vs ECS. Ni cette longueur d'onde d'excitation ni ce faible potentiel appliqué ne sont capables de stimuler la lumière ECL s'ils sont appliqués seuls, mais leurs actions conjointes conduisent à une émission ECL stable et intense en milieux aqueux.

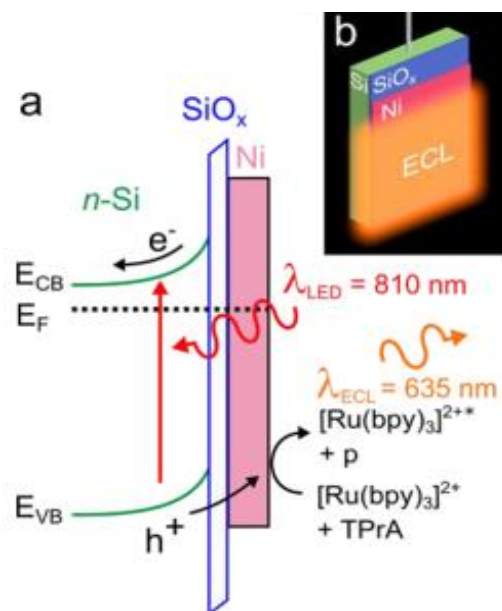


Figure 1. Schéma montrant une photoanode MIS n-Si/SiO_x/Ni pendant PECL (le produit secondaire des radicaux TPrA formés pendant le processus ECL est désigné par p). (b) Schéma montrant les électrodes Si/SiO_x/Ni utilisées dans ce travail avec émission ECL (λ_{ECL}).

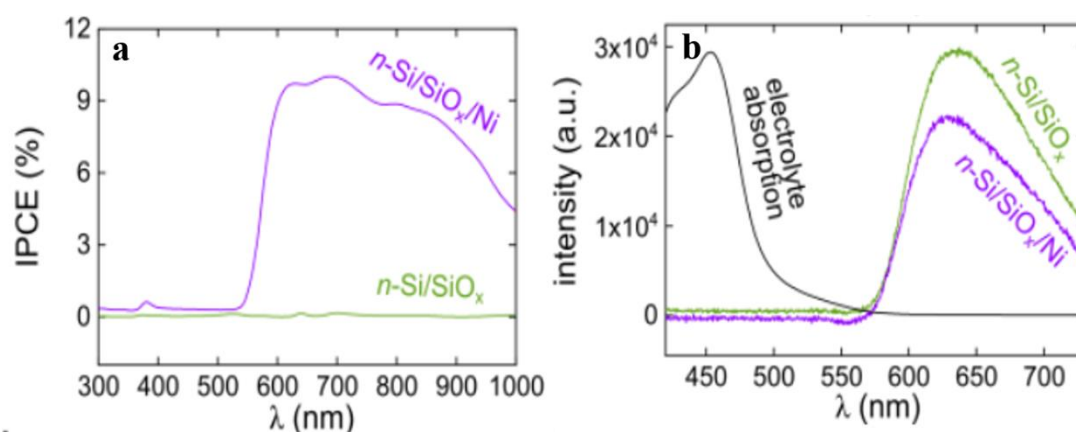


Figure 2. (a) Spectres IPCE enregistrées sur des électrodes n-Si/SiO_x (courbe verte) et n-Si/SiO_x/Ni (1.5 nm) (courbe violette) à un potentiel de 0.7 V vs SCE. (b) Spectre d'absorption normalisé de l'électrolyte (courbe noire), de l'émission P-ECL obtenue sur n-Si/SiO_x (courbe verte) et sur n-Si/SiO_x/Ni (1.5 nm) (courbe violette) à 0.6 V vs SCE sous illumination à $\lambda_{LED} = 810$ nm. Les expériences ont été réalisées dans une solution PBS (pH 7.3) contenant 5 mM [Ru(bpy)₃]²⁺ et 100 mM TPrA.

Les expériences P-ECL ont été réalisées dans une cellule spécifiquement conçue comprenant une fenêtre en quartz devant laquelle était localisée la photoélectrode. Le spectre d'efficacité photon-courant incident (IPCE) du n-Si/SiO_x/Ni a d'abord été enregistré (1,5 nm) (Figure 2a, courbe violette). Il montre une photoconversion efficace à des longueurs d'onde supérieures à 550 nm, avec une efficacité de conversion maximale de ~10% aux alentours de 700 nm. La baisse en dessous de 550 nm s'explique par l'absorption du [Ru(bpy)₃]²⁺ présent dans l'électrolyte, comme le confirme le spectre d'absorption de l'électrolyte (courbe noire de la Figure 2b). Le spectre IPCE enregistré sur n-Si/SiO_x dans les mêmes conditions (Figure 2a, courbe verte) ne présente aucune photoconversion. Ce comportement indique que la passivation de cette dernière électrode s'est produite lors de cette expérience et confirme l'importance de la couche mince de Ni pour promouvoir un transfert de charge stable à l'interface solide-liquide. Pour enregistrer l'ECL en temps réel sur les surfaces n-Si/SiO_x/Ni illuminées, une longueur d'onde incidente de 810nm, qui correspond à un IPCE raisonnable de 9% (Figure 2a), a été employée et est suffisamment éloignée du pic d'émission de l'ECL ($\lambda_{\text{ECL}} = 635 \text{ nm}$, Figure 2b).

Le voltamogramme cyclique (CV) et l'intensité ECL correspondante ont été enregistrés sur n-Si/SiO_x/Ni (1,5 nm) dans l'obscurité et sous éclairage (Figure 3a et b). On peut noter l'absence de signaux de courant et d'ECL dans l'obscurité (courbe noire), ce qui montre le comportement redresseur de la jonction dans cette gamme de potentiel. En revanche, lorsque l'électrode a été éclairée, une densité de photocourant de l'ordre de 1 mA cm⁻² couplée à l'ECL est apparue à des potentiels supérieurs à 0,45 V (courbes violettes de la figure 3a, b), sans baisse pendant six cycles consécutifs. La stabilité a été confirmée par chronopotentiométrie (CP) sous illumination, où une densité de courant constante de 1 mA cm⁻² a été appliquée pendant 15min, au cours desquelles seules des variations négligeables de l'ECL ont été enregistrées (Figure 3c, courbes violettes). En revanche, le n-Si/SiO_x a présenté une désactivation rapide pendant les mesures de CP (Figure 3c, courbe verte). Ce test de stabilité confirme l'importance de la couche de Ni. La comparaison des courbes d'intensité ECL en fonction du potentiel obtenues sur le n-Si/SiO_x/Ni (1.5 nm) photoactif illuminé avec celles enregistrées sur le p⁺-Si/SiO_x/Ni (1.5 nm) non-photoactif (Figure 3e) permet d'estimer un photovoltage (V_{oc}) considérable de 410 mV. Ensuite, l'effet de la couche de Ni est étudié en employant une électrode n-Si/SiO_x/Ni (25 nm). Ce système était également actif en P-ECL, bien qu'il ait présenté une densité de photocourant et une intensité ECL plus faibles. En outre, l'épaississement du film de Ni était également associé à une diminution considérable du photovoltage ($V_{\text{oc}}=150 \text{ mV}$), en bon accord avec les rapports récents montrant que les films métalliques ultraminces sur les photoélectrodes à jonction Schottky à base de n-Si augmentent considérablement la hauteur de la barrière de jonction.^{2,3} Ces résultats

démontrent pour la première fois la génération de P-ECL dans l'eau et ce concept permet l'émission ECL du système $[\text{Ru}(\text{bpy})_3]^{2+}/\text{TPrA}$ à un potentiel proche de 0,45 V, ce qui, à notre connaissance, n'a jamais été rapporté auparavant.

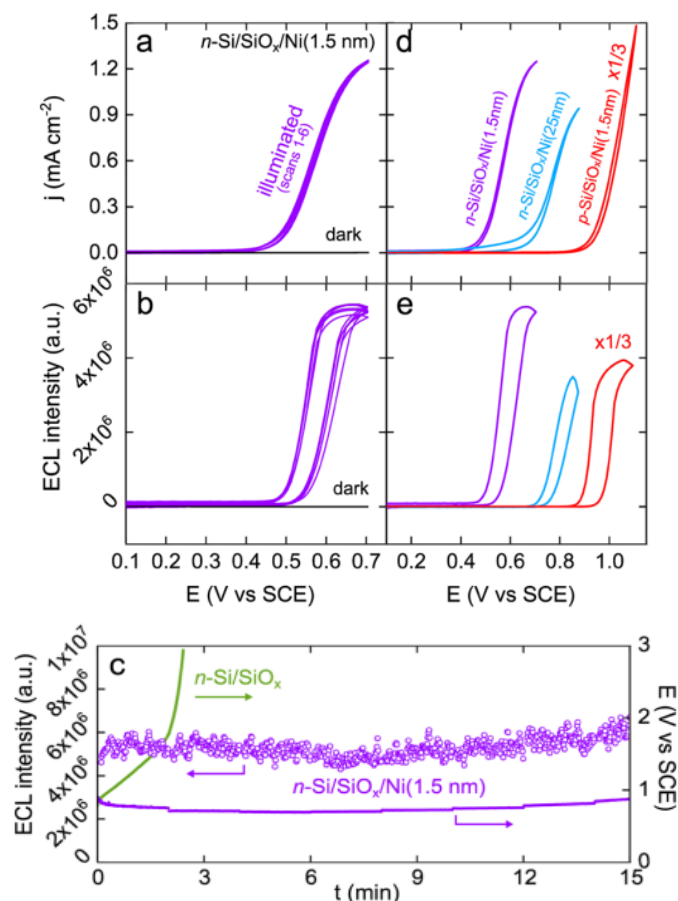


Figure 3 (a) CV enregistrés sur $n\text{-Si/SiO}_x/\text{Ni}$ (1.5 nm) sous éclairage LED à 810 nm (six balayages consécutifs, courbes violettes) et dans l'obscurité (courbe noire). (b) Intensité ECL correspondante vs courbes E. (c) Courbes CP (lignes) enregistrées à 1 mA cm^{-2} sur $n\text{-Si/SiO}_x/\text{Ni}$ (1.5 nm) (courbe violette) et $n\text{-Si/SiO}_x$ (courbe verte) sous illumination à 810 nm. L'évolution de l'intensité ECL sur $n\text{-Si/SiO}_x/\text{Ni}$ (1,5 nm) est représentée par des cercles violets. (d) CV enregistrés dans l'obscurité sur $p^+\text{-Si/SiO}_x/\text{Ni}$ (1.5 nm) (courbe rouge) et sous illumination sur $n\text{-Si/SiO}_x/\text{Ni}$ (1.5 nm) (courbe violette) et $n\text{-Si/SiO}_x/\text{Ni}$ (25 nm) (courbe bleue). (e) Intensité ECL correspondante vs courbes E. Ces mesures ont été réalisées dans du PBS (pH 7.3) avec 5 mM de $[\text{Ru}(\text{bpy})_3]^{2+}$ et 100 mM de TPrA à 20 mV s^{-1} . Les courbes rouges en (d) et (e) ont été divisées par 3 pour plus de clarté.

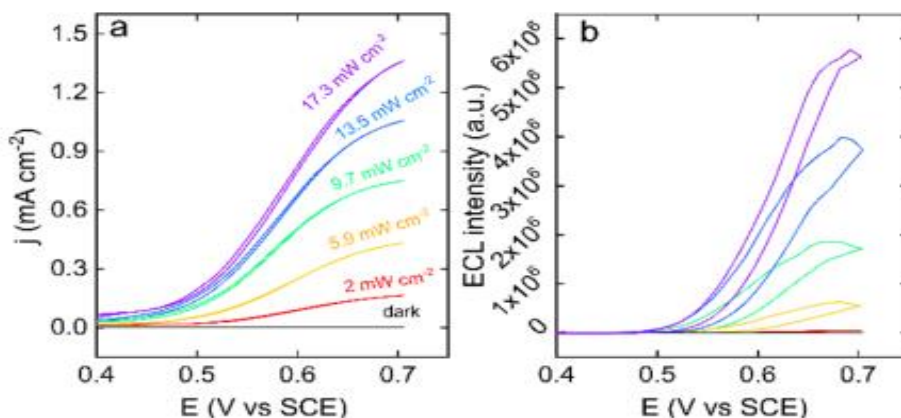


Figure 4. (a) CV enregistrés sur n-Si/SiO_x/Ni (1.5 nm) à différentes densités de puissance LED. (b) Intensité ECL correspondante vs courbes E. Ces mesures ont été effectuées dans une solution PBS (pH 7.3) contenant 5 mM de [Ru(bpy)₃]²⁺ et 100 mM de TPrA avec une lumière incidente de 810 nm à une vitesse de balayage de 20 mV s⁻¹.

L'effet de la puissance d'illumination sur le signal P-ECL a finalement été étudié, comme le montre la figure 4. Dans l'obscurité, il n'y a pas de photocourant et de signal ECL correspondant (courbe noire dans (a) et (b)). Dans ces expériences, les CV et les profils d'intensité ECL correspondants ont été enregistrés à différentes valeurs de puissance d'illumination, montrant que les deux signaux dépendent de la puissance d'illumination incidente. Pour une illumination de 17,3 mW cm⁻², le plus grand photocourant et la lumière ECL la plus forte ont été obtenus. Cette stratégie P-ECL peut être étendue à d'autres types de réactions sur une variété de SCs de types n- et p-, et peut trouver des applications pour la conception de nouvelles stratégies de détection, de systèmes adressables par la lumière ou de dispositifs d'imagerie infrarouge.

Dans le cas de la P-ECL, la lumière incidente est convertie en une longueur d'onde différente par une réaction électrochimique sur une photoélectrode SC et permet de déclencher l'ECL à de faibles potentiels. Ce concept a été utilisé pour concevoir des systèmes de conversion haute. Cependant, la P-ECL souffre fortement de l'instabilité photoélectrochimique de ces SCs à faible bande interdite. La deuxième partie de ce chapitre rapporte pour la première fois une stratégie originale de conversion de la lumière basée sur la P-ECL d'un dérivé du luminol (L-012) sur des photoanodes BiVO₄ à large bande interdite dans l'eau.⁴ La lumière incidente de 375 nm photoexcite simultanément la fluorescence du L-012 et la photoanode. Cependant, le signal résultant est dominé par l'émission P-ECL. L'émission P-ECL peut être induite à un potentiel aussi bas que -0,4 V pendant plusieurs heures et peut être utilisée pour régler finement la luminescence de L-012 (Figure 5). Ces développements de l'ECL sont prometteurs pour la conception de nouveaux dispositifs analytiques luminescents.

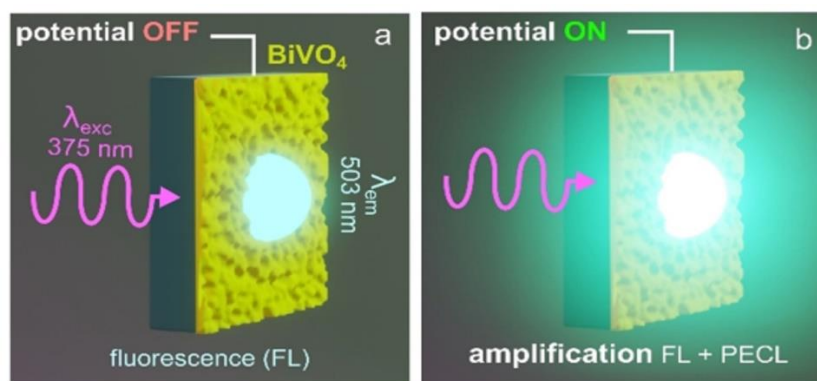


Figure 5. a,b) Schéma de principe illustrant l'amplification de la luminescence. (a) FL est générée à une interface BiVO₄/liquide lors d'une illumination à 375 nm. (b) La luminescence est amplifiée en imposant un potentiel à la surface qui déclenche l'émission P-ECL.

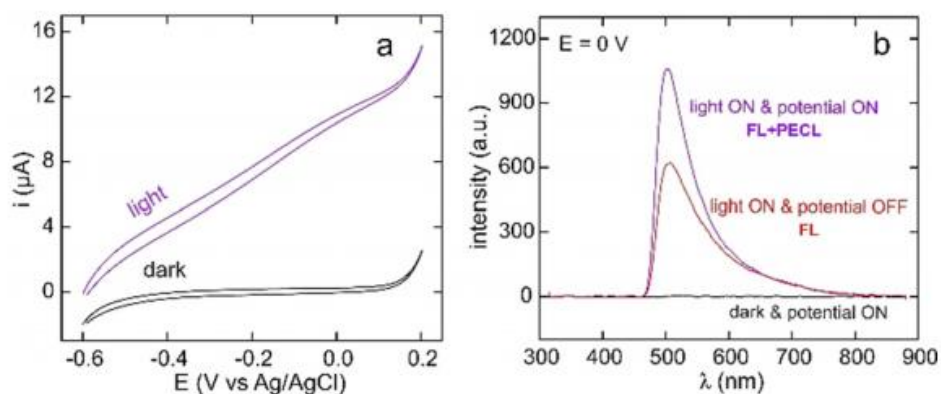


Figure 6. a) CV enregistrés au BiVO₄ à 20 mVs⁻¹ dans l'obscurité (noir) et sous éclairage (violet). b) Spectres de luminescence enregistrés à 0 V dans l'obscurité (courbe noire), à circuit ouvert sous éclairage LED (courbe rouge, FL) et à 0 V sous éclairage LED (courbe violette, FL+P-ECL). Les mesures ont été enregistrées avec P_{LED} = 15.3 mW (λ_{exc} = 375 nm) dans du NaOH 0.1 M avec une concentration en L-012 de 10 mM.

Les CVs ont été enregistrés soit dans l'obscurité soit sous illumination LED. Alors que des courants négligeables ont été mesurés dans l'obscurité, un photocourant anodique est apparu sous illumination par la LED, suggérant la consommation des trous photogénérés dans un processus d'oxydation. Cette CV démontre la photoactivité de la surface du BiVO₄ sous illumination (Figure 6a). L'influence du potentiel appliqué sur la luminescence est clairement illustrée par la figure 6b. Dans l'obscurité, aucun signal ECL n'est apparu. Inversement, sous illumination, des pics ECL intenses sont apparus sur la surface. L'émission en circuit ouvert (courbe rouge) est causée par le L-012 FL et présente un maximum à λ_{em} = 503 nm. De manière remarquable, l'application d'un potentiel de 0 V à la surface du BiVO₄ amplifie considérablement la luminescence, entraînant une augmentation de l'intensité de la luminescence (c'est-à-dire λ_{em}) de plus de 70% (spectre violet).

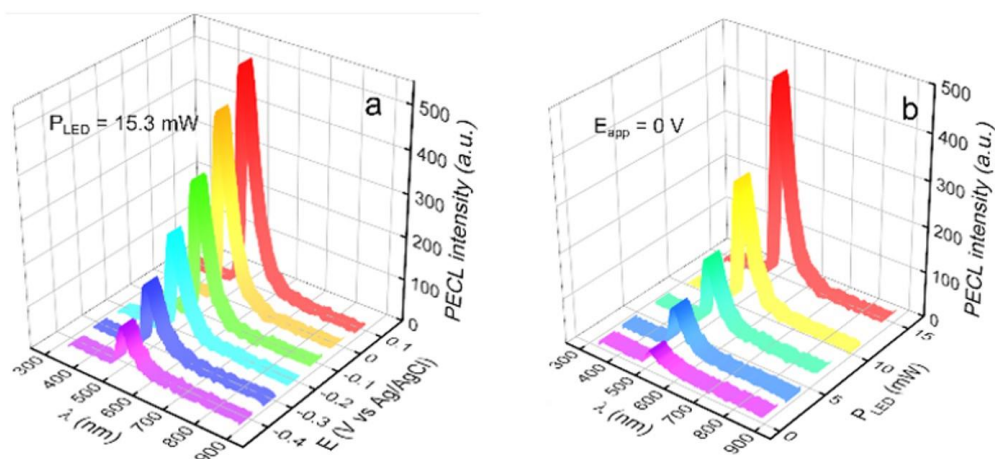


Figure 7. a) Spectres P-ECL obtenus sous illumination LED constant à différents potentiels imposés. b) Spectres P-ECL obtenus constant à un potentiel constant (0 V) sous différents puissances d'illumination de la LED (P_{LED}).

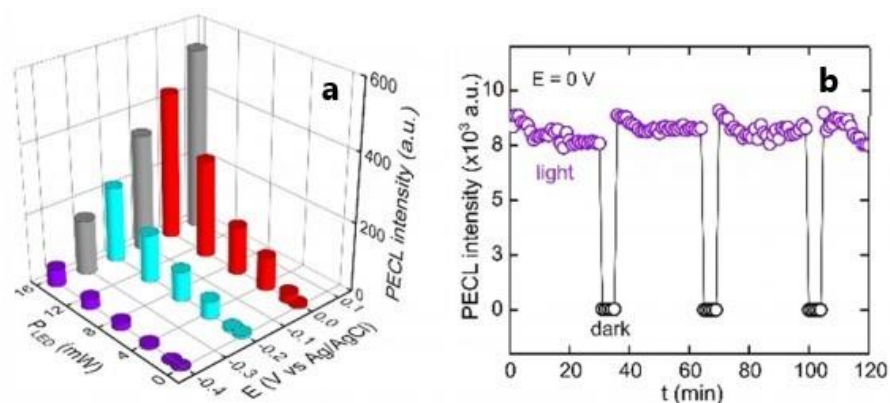


Figure 8. a) Graphe montrant l'évolution de l'intensité du signal P-ECL en fonction du potentiel appliqué et de la puissance d'illumination. b) Variations de l'intensité du signal P-ECL en fonction du temps à 0 V sous illumination intermittente. Les spectres P-ECL sont obtenus en soustrayant aux spectres globaux lumineux (FL+PECL) les spectres FL enregistrés à circuit ouvert. Les mesures (b) ont été obtenus à $P_{LED}=15.3$ mW. Toutes les mesures ont été réalisées à $\lambda_{exc}=375$ nm dans 0.1M NaOH contenant 10 mM L-012.

La figure 7a montre l'effet du potentiel sur l'intensité du signal P-ECL dans la plage de -0,4 à 0,1 V et révèle que la P-ECL augmente avec l'augmentation du potentiel. Plus précisément, son intensité a été multipliée par 5,5 dans cette plage de potentiel. Il est également frappant d'observer que la P-ECL a pu être mesurée à un potentiel aussi bas que -0,4 V (Figure 7 a, spectre violet), qui est, à notre connaissance, le potentiel le plus bas jamais rapporté pour la génération d'ECL d'un dérivé du luminol. Dans la figure 7b, l'effet de la puissance d'illumination de la LED est clairement démontré. La puissance de la LED varie de 1,3 à 15,3 mW et le potentiel est maintenu constant ($E =$

0 V) ; la P-ECL a une réponse cohérente avec l'augmentation de la puissance de la LED. Ainsi, cela prouve clairement que la puissance d'illumination par la LED a une forte influence sur le signal P-ECL et a conduit à une augmentation de son intensité de plus de 13 fois.

Une série de résultats, obtenus en faisant varier le potentiel et la puissance de la LED (P_{LED}), est rassemblée dans la figure 8 a, qui montre l'intensité maximale de P-ECL en fonction de ces paramètres, et illustre clairement comment ils influencent le signal P-ECL. Alors que l'émission PECL n'est pas générée à faibles valeurs de P_{LED} , elle devient très élevée pour des valeurs importantes de potentiel et de P_{LED} . Quantitativement, la plus forte amplification a été obtenue pour + 0,1 V et 15,3 mW. La stabilité de cette électrode a été testée en mesurant l'intensité P-ECL en fonction du temps sous illumination intermittente. Comme le montre la figure 8b, la P-ECL répond instantanément à l'illumination et est plutôt stable à 0 V sur 2 heures. Ce système peut être employé pour adapter précisément l'émission de L-012 et ce rapport constitue le premier exemple de PECL où $\lambda_{exc} < \lambda_{em}$. Ce concept prometteur pourrait trouver des applications potentielles dans la biodétection et les dispositifs adressables par la lumière.

Le chapitre 3 présente des surfaces d'alliage mésoporeux Pt-Ir à impression chirale combinées à l'ECL pour la détection sélective des deux énantiomères de la phénylalanine (PA). Cet acide aminé peut agir simultanément comme une cible chirale et comme un co-réactif pour générer des différences significatives dans les signaux ECL dans des conditions physiologiques (Figure 9).

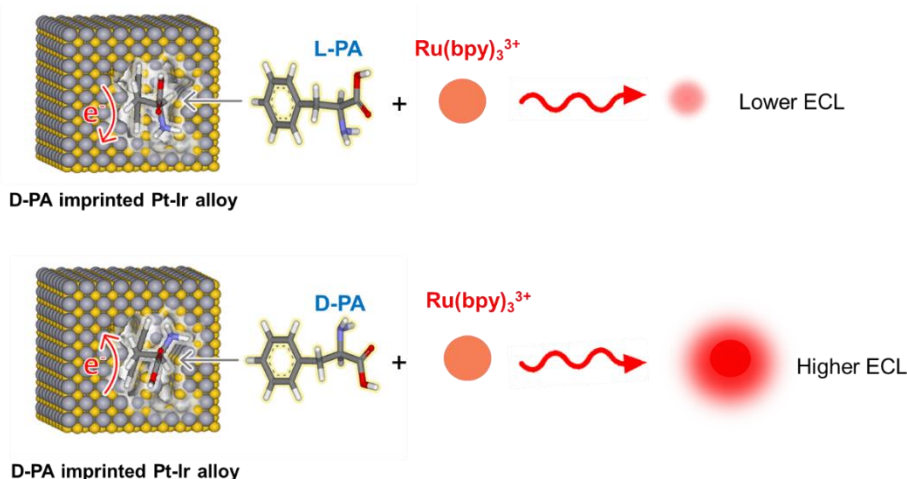


Figure 9. Représentation schématique de la réaction entre $[Ru(bpy)_3]^{3+}$ et le radical PA généré par oxydation sur les surfaces d'électrode d'alliage mésoporeux Pt-Ir imprimées avec D-PA.

L'information structurelle chirale codée dans l'alliage mésoporeux est convertie en une électrogénération énantiosélective de l'état excité du luminophore $[Ru(bpy)_3]^{2+}$,

qui produit *in fine* l'émission lumineuse différenciée. Par conséquent, cette stratégie peut être appliquée efficacement pour la discrimination chirale, sur la base d'une différence d'émission lumineuse jusqu'à 20 fois supérieure pour les deux énantiomères.

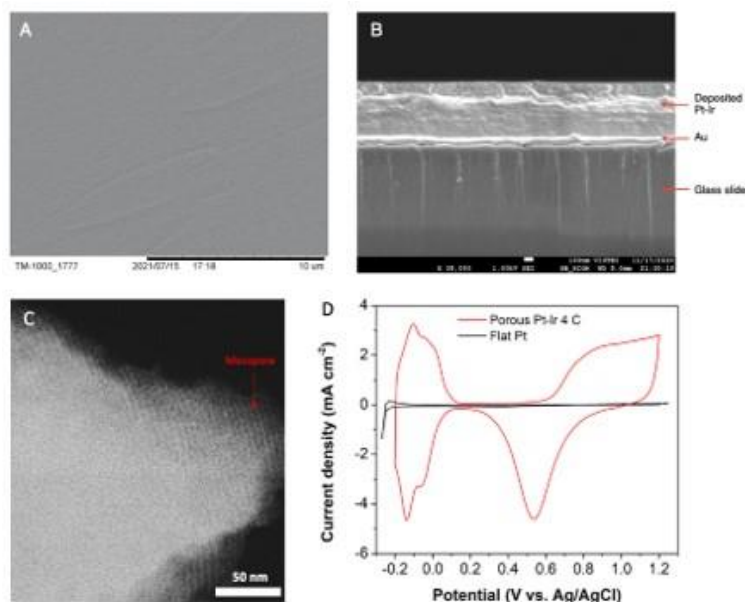


Figure 10. Caractérisation des surfaces d'électrode chirale d'alliage mésoporeux Pt-Ir imprimées par imagerie MEB avec a) Vue du dessus (barre d'échelle : 10 μm), b) Vue de profil (barre d'échelle : 100 nm). c) Images du film mésoporeux Pt-Ir (barre d'échelle : 50 nm); d) CVs du Pt-Ir mésoporeux (courbe rouge) et d'une surface plane de Pt commercial (courbe noire) enregistrés dans une solution de 0.5 M H_2SO_4 à la vitesse de balayage de 100 mV s^{-1} . Le dépôt de l'alliage Pt-Ir est obtenu par électrodéposition en faisant passer une densité de charge de 4 C cm^{-2} .

L'alliage Pt-Ir déposé est obtenu en faisant circuler une densité de charge de 4 C cm^{-2} . Il présente des propriétés exceptionnelles telles qu'une surface extérieure parfaitement lisse (Figure 10a) et une épaisseur uniforme du film Pt-Ir déposé d'environ 500 nm (Figure 10b).⁵ L'image de microscopie électronique à transmission (Figure 10c) révèle une disposition des pores très ordonnée avec un diamètre moyen des pores d'environ 5 nm.⁶ La porosité élevée de l'électrode Pt-Ir poreuse préparée est encore soulignée par une courbe de voltampérométrie cyclique significativement plus grande que celle du Pt commercial plat. Typiquement, la surface électrochimiquement active est estimée dans la région d'adsorption/désorption d'hydrogène dans une fenêtre de potentiel entre 0,0 et -0,25 V vs Ag/AgCl,⁷ et ces mesures permettent de calculer un facteur de rugosité allant jusqu'à 100 (Figure 10d), indiquant que la structure mésoporeuse a été générée avec succès à la surface de l'électrode.

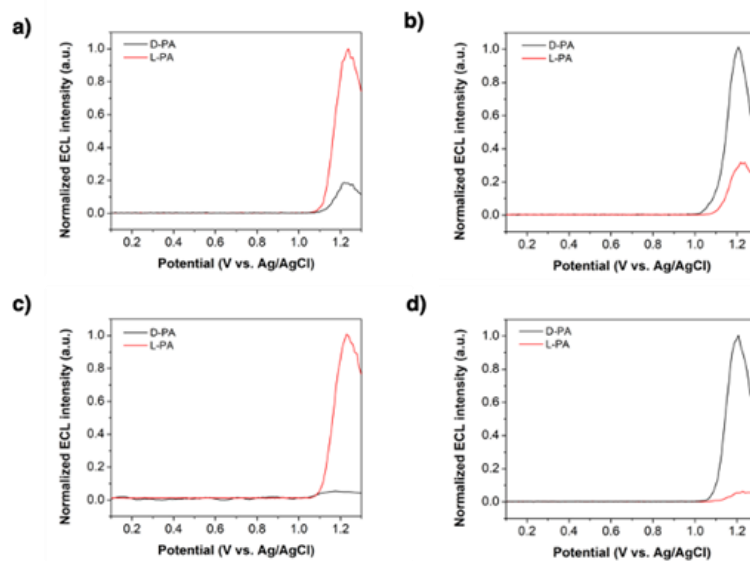


Figure 11. Discrimination chirale par ECL sur des surfaces d'électrode chirale d'alliage mésoporeux Pt-Ir imprimées avec a), c) L-PA, and b), d) D-PA soit fraîches (haut) ou activées (bas). Cela montre la bonne discrimination des 2 énantiomères de PA. Les expériences ont été réalisées avec 10 mM L-PA ou D-PA/1 mM $[\text{Ru}(\text{bpy})_3]^{2+}$ dissous dans une solution de 0.1 M PBS.

La voltamétrie différentielle à impulsions (ou differential pulse voltammetry, DPV) combinée à une émission ECL énantiosélective peut conduire à une amélioration très significative du signal, par rapport à la DPV seule. L'alliage Pt-Ir mésoporeux imprimé avec le L-PA révèle des propriétés de reconnaissance chirale prononcées avec un signal ECL cinq fois plus élevé pour le L-PA par rapport au D-PA (Figure 11a). De même, le D-PA donne un signal ECL beaucoup plus fort sur les électrodes de Pt-Ir mésoporeux imprimées avec D-PA par rapport à une solution de L-PA (Figure 11b). Même si les électrodes Pt-Ir fraîchement préparées peuvent distinguer les énantiomères de PA, la sensibilité de cette analyse ECL reste limitée car la surface peut être progressivement passivée par l'adsorption de molécules. Afin d'améliorer le signal ECL, une technique de régénération de surface induite par le potentiel a été développée. La surface métallique a été activée et nettoyée en utilisant la chronoampérométrie, par application d'un potentiel négatif constant de -0,1 V pendant 30 s pour éliminer toute espèce physisorbée sur la surface métallique mésoporeuse avant l'analyse ECL.⁸ Il est intéressant de noter que la capacité de discrimination est considérablement améliorée dans ce cas (Figure 11c et d). L'énantiosélectivité, exprimée par le rapport des signaux ECL respectifs, atteint des valeurs supérieures à 20. Ces valeurs sont environ cinq fois $4,9(\pm 1,6)$ plus élevées que celles des électrodes Pt-Ir imprimées PA non activées. Cette meilleure énantiosélectivité pourrait être attribuée au fait que l'étape de nettoyage affecte également la surface interne énantiosélective des mésopores et la surface externe non sélective de la couche de Pt-Ir. Comme les mésopores représentent une fraction

plus élevée de la surface totale disponible, cela conduit à une augmentation relative du signal de l'espèce imprimée, qui réagit préférentiellement à l'intérieur des pores. Il en résulte une plus grande probabilité pour que la réaction bimoléculaire entre le $[\text{Ru}(\text{bpy})_3]^{2+}$ oxydé et l'espèce PA se produise de manière stéréosélective, et génère par conséquent un signal ECL significativement plus important pour l'énantiomère imprimé.

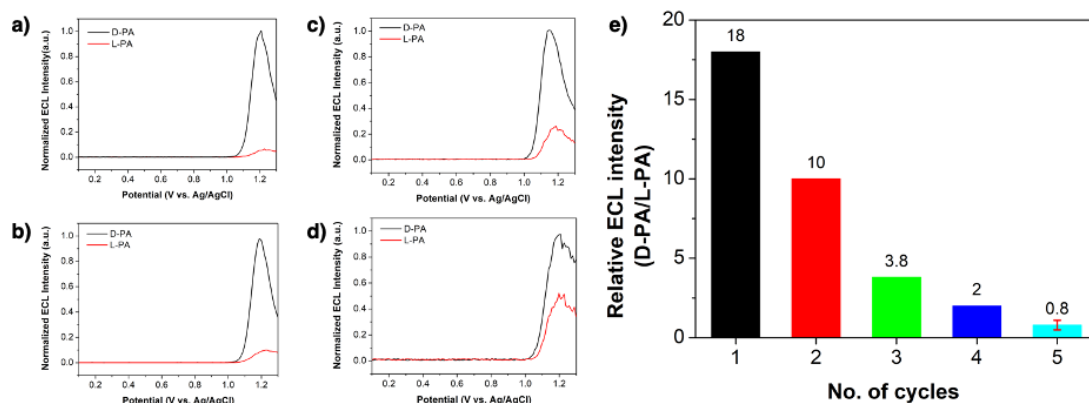


Figure 12. Test de stabilité d'un alliage Pt-Ir imprimé avec D-PA pour la discrimination des énantiomères de PA à l'aide de l'ECL. a) - d) Courbes ECL normalisées enregistrées avec les deux énantiomères d'acides aminés lors de quatre cycles voltampérométriques consécutifs ; e) Rapport des signaux ECL respectifs en fonction du nombre de cycles. Les expériences ont été réalisées par balayage voltampérométrique dans des solutions de L-PA et de D-PA/1 mM de $[\text{Ru}(\text{bpy})_3]^{2+}$ dissoutes dans des solutions PBS 0,1 M, en utilisant une électrode mésoporeuse Pt-Ir imprimée avec D-PA. Une régénération de surface induite par le potentiel a été réalisée avant chaque analyse.

La stabilité et la réutilisabilité des surfaces d'alliage Pt-Ir à empreinte chirale ont été étudiées. La figure 12a montre la réponse ECL d'une surface Pt-Ir imprimée au D-PA en présence de D- et L-PA pendant le premier balayage anodique d'électrodes fraîches. Les figures 12b-d montrent les signaux ECL enregistrés pendant trois balayages anodiques ultérieurs avec la même électrode. L'intensité ECL relative mesurée dans la solution contenant du L-PA a tendance à augmenter par rapport au D-PA (Figure 12a-d). Cela montre que la surface Pt-Ir imprégnée de D-PA peut être réutilisée jusqu'à quatre cycles de détection, malgré une diminution de l'énantiosélectivité comme le résume la figure 12e. Cette perte de sélectivité est liée à la formation d'oxyde métallique lors de l'application de potentiels fortement anodiques allant jusqu'à 1,3 V. L'oxyde métallique généré entrave partiellement l'électrooxydation du PA, ce qui entraîne une diminution significative des intensités ECL.⁹ Ces résultats démontrent pour la première fois que les métaux mésoporeux à empreinte chirale peuvent être utilisés pour l'énantio-discrimination par ECL. Comme l'activité ECL est basée sur la présence du groupe amine dans la molécule cible, il est facile d'imaginer que la stratégie peut être étendue à d'autres molécules ayant des fonctions amine, et

surtout à d'autres membres de la famille des acides aminés.

En conclusion, ce travail de thèse s'est concentré sur l'étude du phénomène ECL. Dans le chapitre 2, un nouveau concept, P-ECL, qui combine la photoactivation de SC avec l'ECL est développé. La stratégie P-ECL est rapportée pour la première fois sur les semi-conducteurs de type n sous illumination, donnant une émission ECL remarquablement stable et intense dans l'eau. La première partie de ce chapitre a démontré que l'émission ECL à 635 nm a été obtenue sur une électrode n-Si/SiO_x/Ni(1,5 nm) sous une illumination à 810 nm dans le système [Ru(bpy)₃]²⁺/TPrA à un potentiel assez bas, 0,45 V vs ECS. De plus, le signal ECL obtenu sur le n-Si/SiO_x/Ni photoactif était plus brillant que celui obtenu sur le n-Si/SiO_x photoactif et peut rester constant pendant 15 minutes, ce qui confirme que la couche de Ni peut stabiliser l'électrode et favoriser un transfert de charge stable à l'interface solide-liquide. Dans cette partie, le concept PECL a été utilisé pour concevoir des systèmes de conversion ascendante. Cependant, la P-ECL souffre fortement de l'instabilité photoélectrochimique de ces SCs à faible bande interdite. Dans la deuxième partie de ce chapitre, une stratégie originale de conversion de la lumière basée sur la P-ECL générée sur un autre SC à large bande interdite a d'abord été présentée. La PECL n'a pas seulement été induite à des potentiels assez bas, mais elle peut également répondre instantanément à une illumination pendant plus de 2 heures à un potentiel constant. Dans ce travail, BiVO₄ a été utilisé comme photoanode dans le système ECL L-012/NaOH avec une source de lumière à 375 nm pour la luminescence de L-012 ainsi que la génération de P-ECL. En raison du faible potentiel d'oxydation du L-012, du photovoltage élevée de l'électrode et de la stabilité chimique de BiVO₄, une luminescence amplifiée induite par des trous photogénérés à la surface de la photoanode BiVO₄ sous une illumination de 375 nm a été observée, lorsque le potentiel appliqué est aussi bas que -0,4 V par rapport à Ag/AgCl. Une émission plus intense est obtenue avec une contribution significative de P-ECL, qui augmente avec le potentiel, à l'intensité lumineuse globale. En raison de la stabilité chimique du BiVO₄, la P-ECL peut être induite à la surface de l'électrode pendant plus de 2 heures à 0 V. Cette stratégie peut être employée pour adapter précisément l'émission de L-012 et ce travail constitue le premier exemple de PECL de " type fluorescence " où $\lambda_{exc} < \lambda_{emi}$. Au total, le concept de P-ECL peut être appliqué à d'autres types de réactions (y compris les réactions cathodiques) sur une variété de SCs de type n et p, et ainsi, une large gamme de systèmes P-ECL avec différentes caractéristiques d'absorption/émission devrait être facilement accessible. En plus d'être bénéfiques en termes de gain de potentiel électrochimique, les systèmes P-ECL peuvent être conçus comme de nouvelles stratégies de détection, utilisées en biodétection ou pour des dispositifs d'imagerie infrarouge ou adressables par la lumière.

Le chapitre 3 présente pour la première fois un nouveau concept d'ECL chirale

utilisé pour la discrimination énantiomérique. Les énantiomères sélectionnés d'acides aminés, L et D-PA, utilisés comme composés chiraux et comme co-réactifs pour générer l'émission stéréosélective de signaux ECL dans le système $[\text{Ru}(\text{bpy})_3]^{2+}/\text{PBS}$, ont été discriminés par ECL sur des alliages mésoporeux Pt-Ir imprimés avec la PA. L'adsorption énantiosélective de molécules chirales sur des surfaces métalliques est contrôlée par la chiralité des sites de reconnaissance imprimés dans la structure des alliages métalliques, ce qui conduit à la différence des signaux ECL. Ces métaux mésoporeux à impression chirale, combinés à la mésoporosité qui peut augmenter le transport de masse, et aux sites de reconnaissance qui peuvent améliorer la durée de vie des molécules préférées pour augmenter l'intensité de l'ECL, ont démontré une discrimination énantiomérique efficace par la différence de sensibilité de l'ECL et une stabilité exceptionnelle après de nombreux cycles catalytiques. Cette stratégie illustre la puissance de l'utilisation d'une lecture basée sur l'ECL, étendant l'application de la technique ECL et ce concept en tant que détection chirale présente de nombreux avantages, comme un fonctionnement simple, un faible signal de fond, une sensibilité élevée à faible concentration. Ce concept permet de surmonter les nombreuses limitations des autres techniques, comme le coût élevé des instruments avancés, les processus analytiques longs, etc. Les résultats de ces premières expériences de preuve de principe ouvrent des perspectives intéressantes pour le développement d'autres structures métalliques à codage moléculaire pouvant être utilisées pour une telle détection optique. En outre, elle peut être développée comme une technique de détection efficace pour la discrimination des énantiomères en (bio)analyse.

Reference:

1. Zhao, Y.; Yu, J.; Xu, G.; Sojic, N.; Loget, G., *Journal of the American Chemical Society* 2019, 141 (33), 13013-13016.
2. Kenney, M. J.; Gong, M.; Li, Y.; Wu, J. Z.; Feng, J.; Lanza, M.; Dai, H., *Science* 2013, 342 (6160), 836-840.
3. Laskowski, F. A.; Nellist, M. R.; Venkatkarthick, R.; Boettcher, S. W., *Energy & Environmental Science* 2017, 10 (2), 570-579.
4. Yu, J.; Saada, H.; Abdallah, R.; Loget, G.; Sojic, N., *Angewandte Chemie International Edition* 2020, 59 (35), 15157-15160.
5. Miao, W.; Choi, J.-P.; Bard, A. J., *Journal of the American Chemical Society* 2002, 124 (48), 14478-14485.
6. Attard, G. S.; Bartlett, P. N.; Coleman, N. R.; Elliott, J. M.; Owen, J. R.; Wang, J. H., *Science* 1997, 278 (5339), 838-840.
7. Łukaszewski, M.; Soszko, M.; Czerwiński, A., *Journal of Electrochemistry Science* 2016, 11 (6), 4442-4469.

-
8. Devadas, B.; Periasamy, A. P.; Bouzek, K., *Coordination Chemistry Reviews* 2021, 444, 214062.
 9. Olsson, L.; Fridell, E., *Journal of Catalysis* 2002, 210 (2), 340-353.

Abstract

Electrogenerated chemiluminescence (ECL) is a light emission phenomenon initiated by electrochemically generated radical species, which then undergo a series of electron transfer reactions. It leads to the final generation of an excited state that radiatively decays to the ground state. In this work, my goal was to develop fundamental aspects of ECL at different scales. In the first part, the novel concept of photo-induced electrochemiluminescence (P-ECL) was introduced on two kinds of n-type semiconductor electrodes. The ECL was generated in the model ECL system involving the simultaneous oxidation of $[\text{Ru}(\text{bpy})_3]^{2+}/\text{TPrA}$ and L-012. The ECL emission is triggered by photogenerated holes (h^+) in an n-type semiconductor (SC) electrode, where can generate P-ECL at a low potential. This P-ECL strategy can be extended to other types of reactions on a variety of absorbing n- and p-type semiconductors and can also be developed to use other luminophores and is a promising technique for ultrasensitive detection, light-addressable and imaging devices. In the second part of the thesis, a new ECL detection technique, chiral ECL is presented. The effective discrimination through ECL sensitivity between two enantiomers was observed on PA imprinted Pt-Ir alloy metal with cavities. In this system, PA is used as chiral target compound and the co-reactant, triggering bright and defined ECL on the preferable Pt-It metal surface with cavities which can enhance the lifetime, increasing the sensitivity of the preferable ECL.

吾生也有涯，而知也无涯。 -- 《庄子》

路漫漫其修远兮，吾将上下而求索。 -- 屈原《离骚》

星星之火，可以燎原。 -- 《尚书》

精诚所至金石为开。 -- 《后汉书·广陵思王荆传》

There is a limit to our life, but to knowledge, there is no limit.

-- 《ZhuangZi》

The road ahead is long and has no end, yet high and low I will search with my will unbending.

-- QuYuan 《LiSao》

a single spark can start a huge blaze (idiom), an insignificant cause can have a massive effect.

-- 《Shang》

Sufficient sincerity can break up hard gold and stone.

-- 《Houhan》

Table of contents

List of abbreviations	20
General introduction	21
Chapter 1. Overview of electrogenerated chemiluminescence	23
1.1 Introduction	24
1.2 Light emission phenomena	25
1.2.1 Photoluminescence	26
1.2.2 Chemiluminescence	27
1.2.3 Electroluminescence	29
1.3 ECL mechanisms	30
1.3.1 Annihilation pathway	30
1.3.2 Co-reactant pathway	34
1.4 Luminophores	41
1.4.1 Metal chelates	41
1.4.2 Organic luminophores	45
1.4.3 Nanoparticle systems	48
1.5 ECL applications	50
1.6 Conclusions	51
References	52
Chapter 2. Photoinduced electrochemiluminescence at depleted semiconductor electrodes in water	58
2.1 Introduction	59
2.2 PECL by Upconversion at Silicon Electrodes in Water	65
2.2.1 Principle of P-ECL on a Silicon Anode	66
2.2.2 Characterization of the Si-based anodes	67
2.2.3 Electrochemistry and PECL of Si/SiO _x /Ni	69
2.3 Luminescence Amplification at BiVO ₄ Photoanodes by PECL	74
2.3.2 Characterization of BiVO ₄ electrode	77
2.3.3 Electrochemistry and PECL on BiVO ₄	79
2.4 Conclusion	82
Experimental section	83
1. Photoinduced electrochemiluminescence at depleted semiconductor electrodes in water	83
1.1 Photoinduced electrochemiluminescence by Upconversion at Silicon Electrodes in Water	

.....	83
1.1.1 Material	83
1.1.2 Electrode preparation	83
1.1.3 Electrochemical and photoelectrochemical experiments	84
1.2 Luminescence Amplification at BiVO ₄ Photoanodes by Photoinduced Electrochemiluminescence	86
1.2.1 Material	86
1.2.2 Electrode preparation	86
1.2.3 Material characterization	87
1.2.4. Electrochemical, photoelectrochemical and optical characterization	87
References	88
Chapter 3. Electrochemiluminescent enantioselective detection with chiral-imprinted mesoporous metal surfaces	92
3.1 Introduction	92
3.2 Results and Discussion	97
3.3 Conclusion	104
Experimental section	105
2.1 Chemicals	105
2.2 Synthesis of phenylalanine (PA)-encoded mesoporous Pt-Ir alloy electrodes	105
2.3 Characterization of chiral-encoded mesoporous Pt-Ir alloy electrodes	106
2.4 Electrochemistry and electrochemiluminescence (ECL) analysis	106
References	107
Conclusions and Perspectives	111
Acknowledgements	113

List of abbreviations

AL	Anionic ligand
BPO	benzoyl peroxide
CA	chronoamperometry
CE	counter electrode
ACN	acetonitrile
CL	chemiluminescence
CV	cyclic voltammetry
DCM	dichloromethane
DPV	differential pulse voltammetry
ECL	electrochemiluminescence
EL	electroluminescence
E	potential
FL	fluorescence
FTO	fluorine doped tin oxide
GC	glassy carbon
L-012	8-amino-5-chloro-7-phenylpyrido[3,4-d]- pyridazine-1,4(2H, 3H)-dione]
LED	light-emitting diode
NL	neutral ligand
OH ⁻	hydroxide anion
OH [•]	hydroxyl radical
PA	phenylalanine
PECL	photo-induced electrochemiluminescence
P _{LED}	LED illumination power
PAH	polyaromatic hydrocarbons
PBS	phosphate buffer saline
PL	photoluminescence
PMT	photomultiplier tube
QRE	quasi reference electrode
RE	reference electrode
SC	semiconductor
SCE	saturated calomel electrode
TBAPF ₆	tetra- <i>n</i> -butylammonium hexafluorophosphate
TPrA	tri- <i>n</i> -propylamine
WE	working electrode

General introduction

Electrochemiluminescence (ECL) is a kind of luminescence produced during electrochemical reactions on the electrode surface. ECL is mostly used for analytical applications. Moreover, ECL combined with other techniques or different materials can be developed as a new detection technique or analytical method.

Chapter 1 presents the overview of ECL. ECL and other forms of light emission including photoluminescence, chemiluminescence and electroluminescence, were introduced. Then the general view of annihilation and co-reactant mechanisms, organic and inorganic luminophores and analytical applications were presented.

Chapter 2 presents photo-induced electrochemiluminescence of the model ECL systems in water on n-type semiconductors as photoanodes under an excited light source. The combination between ECL and photochemistry of semiconductors is termed as photo-induced electrochemiluminescence. This part introduces “up-conversion type” and “fluorescence type” P-ECL, which relied on employing photogenerated minority carriers within a depleted SC (holes in n-type SC photoanode) observed in a low potential.

Chapter 3 presents the chiral discrimination of two phenylalanine (PA) enantiomers on chiral-imprinted mesoporous Pt-Ir alloy surfaces combined with ECL. A amino acid, PA, acts as the chiral target compound and a co-reactant to obtain notable ECL signals in physiological conditions. The chiral information encoded in the mesoporous alloy is converted into the efficient electrogeneration of the excited state of the model $[\text{Ru}(\text{bpy})_3]^{2+}$ dye, which produces in fine light emission.



Chapter 1.

Overview of electrogenerated chemiluminescence

1.1 Introduction

Electrochemiluminescence (ECL), also referred to as electrogenerated chemiluminescence, belongs to the family of luminescence phenomena. It involves reactive intermediates produced electrochemically at the surface of an electrode and further generating an excited state of luminophore by undergoing a chemical step characterized by a highly exergonic electron-transfer reaction, followed by emission of a photon during relaxation from an excited state to the ground state.¹ Thus, ECL is initiated by an electrochemical step, continues with a homogeneous chemical reaction, and ends with a photochemical step. Such combination of chemiluminescence (CL) and electrochemistry, presents many potential advantages, i.e. it does not require an external light source, the regeneration of reactants to take part in ECL reactions with an excess of coreactants, eliminate the use of toxic or corrosive reagents.^{2, 3}

To trigger ECL generation, electrochemistry allowed greater control of the position of emission and time of ECL reactions and it is possible to electrochemically transform some compounds into species to take part in CL reaction. ECL is weaker than CL since the reaction occurs in the vicinity of the electrode surface, not in the bulk. Thus, sensitive light detectors are highly required.

The first report concerning light emission was initially published in the 1920s.⁴ Later, the electrochemically generated luminescence of fluorescent aromatic molecules in organic solvent was generated by the triplet-triplet annihilation mechanism.^{5,6} The ECL detailed investigations were then reported by Chandross *et al.* and Bard *et al.* in the mid-1960s,⁷ where the use of organic luminophores was limited to aprotic solvents. After these initial reports with aromatic hydrocarbons compounds, the ECL studies of the inorganic system, classic metal chelate $[\text{Ru}(\text{bpy})_3]^{2+}$ and its analogues, were investigated in 1970s, representing an essential breakthrough in this field. In 1972, Bard *et al.* showed that $[\text{Ru}(\text{bpy})_3]^{2+}$ ECL was generated by annihilation reaction between oxidized $[\text{Ru}(\text{bpy})_3]^{3+}$ and reduced $[\text{Ru}(\text{bpy})_3]^+$.⁸ After that, $[\text{Ru}(\text{bpy})_3]^{2+}$ became the most studied ECL luminophore, due to its strong luminescence and high solubility in aqueous and non-aqueous media and its stable generation of reduced and oxidized forms. Later, ECL generation with co-reactants was proposed. In 1981, the first report about ECL was generated in an aqueous solution involving $[\text{Ru}(\text{bpy})_3]^{2+}$ and the co-reactant oxalate ion ($\text{C}_2\text{O}_4^{2-}$), which was a great breakthrough in the ECL study.⁹ Afterwards, another co-reactant TPrA (tri-n-propylamine) was discovered, allowing to produce efficient ECL, not only in aqueous media but also at physiological pH conditions, which opened a new route to apply ECL in the bioanalytical field.

Over the next three decades, ECL has developed rapidly and became an essential and powerful technique

for immunoassays, other clinical diagnostics, environmental testing, biowarfare agent detection, and monitoring visualization of dynamic systems.¹⁰⁻¹⁴

1.2 Light emission phenomena

Luminescence is an emission of ultraviolet, visible or infrared photons from an electronically excited species. The word luminescence, which comes from the Latin “lumen”, describes ‘all those phenomena of light, which are not solely conditioned by the rise in temperature’. Luminescence is cold light and various type of it are classified according to the mode of excitation.

Table1 shows the family of luminescence. Typically, photoluminescence (fluorescence, phosphorescence or delayed fluorescence) is a particular case of luminescence. The mode of excitation is absorption of a photon, which brings the absorbing species into an electronic excited state. Light emission is initiated by photoexcitation (i.e. photons that excite electrons to a higher energy level in an atom or a molecule).¹⁵ CL is the light phenomenon provided by the homogeneous chemical reaction(s) between at least two reagents, it’s chemi-excitation.¹⁶ ECL is a specific case where the reaction of reactive species are produced electrochemically on the electrode surface, in other words, it is electro-chemi-excitation. The difference between CL and ECL is that, CL is produced in the bulk and is controlled by the fluid flow, while ECL is produced in *situ* by applying different potentials at the electrode. Bioluminescence is a form of chemiluminescence where light emission is produced by a living organism.¹⁷ Electroluminescence (EL) is an optical and electrical phenomenon in which a material emits non-thermal emission of visible light as a result of a current flow or in response to a strong electric field.¹⁸ Thermoluminescence is a form of luminescence in which certain crystalline materials emit light upon heating by absorbing energy from electromagnetic radiation or other ionizing radiation.¹⁹ Other light emission phenomena include triboluminescence²⁰ (light is generated when the material is mechanically pulled apart, ripped, scratched, crushed, or rubbed) and sonoluminescence²¹ (short bursts of light emission from imploding bubbles with clock-like precision in a liquid when excited by sound). In this table, to better understand the principles of luminescence, modes of excitation on luminescence phenomenon are described.

Table 1. Various type of luminescence

Phenomenon	Mode of excitation
------------	--------------------

Photoluminescence (fluorescence, phosphorescence, delayed fluorescence)	Absorption of light (photons)
Electroluminescence	Electric field
Thermoluminescence	Heating after prior storage of energy
Chemiluminescence	Chemical process(e.g.oxidation)
Bioluminescence	Biochemical process
Triboluminescence	Frictional and electrostatic forces
Sonoluminescence	Ultrasounds

1.2.1 Photoluminescence

Photoluminescence (i.e., fluorescence or phosphorescence), is the phenomenon of the emission of photons through the excitation of luminophores by ultraviolet or visible light photons.

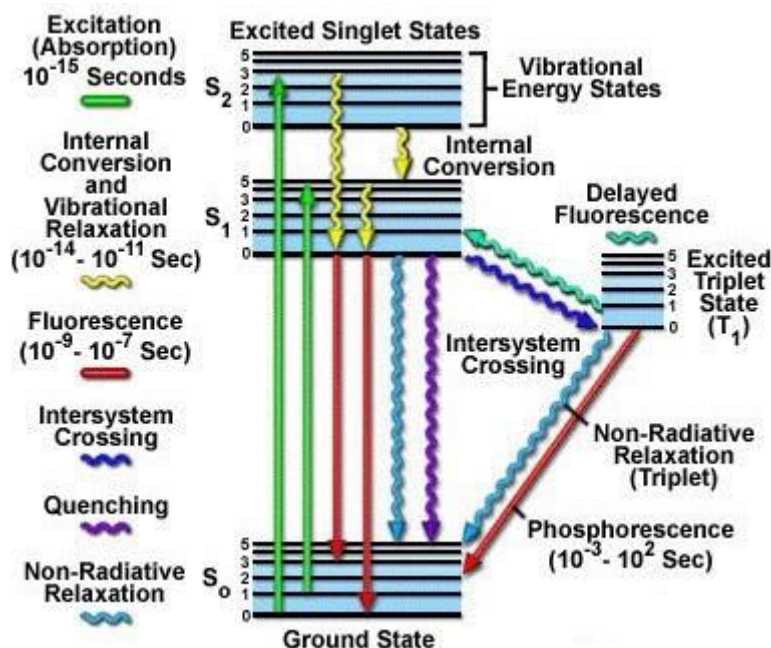


Figure 1. Schematic illustration of the Jablonski energy diagram.²²

This emission process can be represented by the Jablonski diagram (Figure 1). S_0 represents the singlet ground state, S_1 and S_2 represent the first and second electronic excited states, respectively. Triplet electronic excited states are named T_1 , presented on the right side, separated to distinguish their multiplicity. Each electronic energy level of the molecule constitutes many vibrational energy levels, named 0, 1, 2, etc. With the absorption of light, several processes can occur. When the molecule is excited by photon absorption, it can return to the ground state with the emission of fluorescence and phosphorescence or follow many other pathways of de-excitation, such as internal conversion (non-radiative transition between two electronic states with the same spin multiplicity), intersystem crossing (non-radiative transition between two isoenergetic vibrational levels belonging to electronic states with

different spin multiplicity), intramolecular charge transfer and conformational change. The photons emission produced by the lowest vibrational level of S_1 to S_0 relaxation is fluorescence. Due to vibrational relaxation, energy loss occurs in the excited state, where the fluorescence spectrum is located at a wavelength higher than the absorption spectrum. This phenomenon is called “Stokes shift”.

The transition from T_1 to S_0 is forbidden, but it can be observed due to the spin-orbit coupling and low radiative rate constant. This radiative de-excitation from the triplet state T_1 to S_0 is called phosphorescence. The phosphorescence spectrum wavelength is higher than the fluorescence spectrum, because the energy of the lowest vibrational level of the triplet state T_1 is lower than the one of the singlet state S_1 .

When the energy difference between S_1 and T_1 is small, the reverse intersystem crossing from T_1 to S_1 can occur. This results in the same emission as normal fluorescence but with a much longer decay time constant because the molecules stay in the triplet state before emitting from S_1 to S_0 . This fluorescence emission is thermally activated, named as delayed fluorescence of E-type. The other fluorescence is called delayed fluorescence of P-type, was observed with pyrene. In concentrated solutions, a collision occurred between two molecules in the T_1 state that can provide enough energy to allow one of the molecules to return to the S_1 state, and this triplet-triplet annihilation leads to a delayed fluorescence emission.

1.2.2 Chemiluminescence

In CL, the energy source is provided by the homogeneous chemical reactions between at least two reactive species. CL is produced in the bulk by mixing the reactive species and controlled by the fluid flow. It is usually considered as a fluorescence process rather than a phosphorescence process since the triplet state has a longer lifetime compared to the singlet state and shows radiationless deactivation in the presence of some molecules such as dioxygen (quencher). Some fractions of the product or intermediate are formed in an electronically excited state and then relax to the ground state, emitting photons. In general, CL reaction can be divided into two types: direct and indirect CL. The direct reaction²³ contains two steps. The first step comprises production of excited molecule. A substrate and an oxidant react to generate a product or intermediate in the presence of some cofactors. Cofactors can provide an efficient leaving group if bond cleavage is required to produce the excited state, or can transform one or more of

the substrates into a more active form, able to react and interact with the catalyst. Meanwhile, the use of enzymes or metal ions as catalysts could reduce the activation energy and generate an adequate environment for improving CL efficiency. The second step is concerning the excited products return to its ground state followed by several routes (e.g. emission of light, energy transfer or quenching). Another pathway is called indirect CL or energy transfer CL,²⁴ which is based on the energy transfer process that occurred from the excited species to a fluorophore. This process is possible for different molecules that are unable to be directly involved in CL reaction. These molecules transfer their excess energy to a fluorophore that in turn is excited, returning to its ground state with photon emission. During the indirect CL process, a substrate is converted into an electronically excited molecule, related to light emission or acting as the energy transfer donor.

A classical example of CL is luminol in an alkaline solution in the presence of hydrogen peroxide or dioxygen,²⁵ iron or copper,^{26, 27} or an auxiliary oxidant.²⁸ The rate of the luminol oxidation process varies with the oxidant and it has been found to be different for each particular system. The complete mechanism of luminol CL can be divided into two parts (Figure 2). In the first part, the pathway leads to the generation of the key intermediate hydroperoxide adduct (LO₂H) in a two oxidation steps. The first step involves the oxidation of the luminol anion (LH) to luminol radical anion (LH[•]), which could be achieved by different one-electron oxidants including horseradish peroxidase, copper, manganese, or iron. The second oxidation step is that LH[•] oxidized either to aminodiazquinone (L) or hydroperoxide adduct (LO₂H) directly (oxidized by O₂⁻). The second part is the decomposition of this key intermediate (LO₂H), from which molecular nitrogen is expelled, generating excited state 3-aminophthalate dianion. The formation of this key intermediate is heavily dependent upon the composition of the system, like the nature of the oxidant, overall concentrations, additives, buffer and pH. However, its decomposition only depends on the pH of bulk of the solution.

Merenyi²⁹ showed that in the second part, by adding OH⁻ or N₃⁻ to diazaquinone, a new intermediate-acyldiazene is obtained. Thus, the nucleophilic attacked by OH⁻ or N₃⁻ gives rise to the decomposition, and then produce the excited state 3-aminophthalate dianion, which can emit light.

The mechanism pattern is represented below,

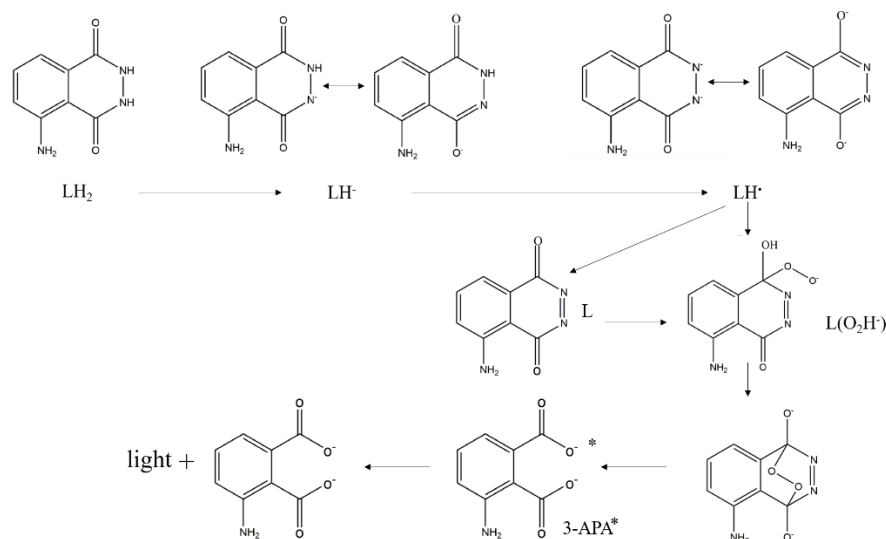


Figure 2. Mechanism of CL luminol oxidation processes.

In this system, the concentration of $O_2^{\bullet -}$ has a vital effect on the fate of the luminol radical. At the beginning of the reaction, $O_2^{\bullet -}$ is absent in the solution and the luminol radical will be oxidized to diazaquinone. Merenyi and Lind reported that luminol radical could slowly react with O_2 , generating $O_2^{\bullet -}$.³⁰ In the routine clinical laboratory, CL is used for immunoassay and DNA probe assays, for the formation of CL labels or for a chemiluminescent detection reaction for an enzyme labelling. CL detection techniques are commonly used to measure enzymatic activity expressed by cellular luminescence, blotted proteins and nucleic acids.

Many factors influence the emission efficiency of CL. The first one is the chemical structure of the CL precursor (substrate), not only the central part containing the electronically excited group, but also the side chain. The second one is the nature and concentration of other substrates, which affect the CL pathway and are beneficial to other non-radiative competition processes. The third factor is the hydrophobicity of the solvent and solution composition. One example shows the quantum yield of oxidized luminol in dimethyl sulfoxide (DMSO) is 0.05, which is smaller than in water (0.01). The color is blue-violet (425 nm) in DMSO and blue-green (480–502 nm) in water.

1.2.3 Electroluminescence

Electroluminescence (EL) is an optical and electrical phenomenon in which a material emits light when a high electric field is applied or when an electric current passes through it.³¹ This is the result of the radiative recombination of electrons and holes in a material, that usually appears on semiconductor

electrodes in the electrochemical cells. The excited electrons release their energy by emitting light. Electrons and holes are separated before the process of recombination either by doping the material, forming a new heterostructure material with a junction or through the excitation of high-energy electrons accelerated by a strong electric field. For example, when a cathodic current passes through an ZnS electrode doped with Mn in a peroxydisulfate ($S_2O_8^{2-}$) solution, an intense light emission centred at about 580 nm was observed.³² The emission was attributed to the injection of electrons into the conduction band of ZnS:Mn. The current flow leads to the reduction of $S_2O_8^{2-}$ and causing the formation of the strong oxidant $SO_4^{\cdot -}$, which can inject holes into the valence band of ZnS:Mn, resulting in electron-hole recombination and emission. This EL process is close to ECL if $S_2O_8^{2-}$ is used as a co-reactant.

Electroluminescent materials contain organic, inorganic, semiconductor or liquid crystal and so on, which can be employed to fabricate electroluminescent devices. Generally, the active materials are semiconductors with suitable bandwidth. Organic semiconductors with anthracene single crystals were first reported in the 1950s.³³ These early studies established that the process responsible for EL requires the injection of electrons from one electrode and holes from the other, the capture of oppositely charged carriers (so-called recombination), and the radiative decay of the excited electron-hole state (exciton) is produced by this recombination process.

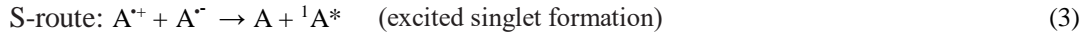
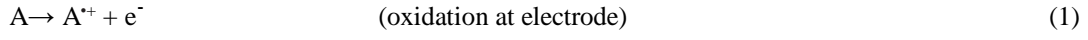
1.3 ECL mechanisms

In this section, the two dominant pathways for the excited states generation, annihilation and coreactant ECL pathways are summarized.

1.3.1 Annihilation pathway

Annihilation pathway involves the reaction between oxidized and reduced species which are generated on the electrode surface by a potential step or sweep. These species interact to produce a ground state and an electronically excited state, which then emits light by returning to its ground state. Most of aromatic compounds used for ECL, follow this kind of mechanism, such as rubrene,³⁴ phenanthrene,³⁵ anthracene.³⁶ Besides forming singlet and triplet excited states, ion annihilation reactions can lead to generating excimers (excited dimers) and exciplexes (excited complexes). In most cases, molecules with π -orbital overlapping are involved in the formation of excimers and exciplexes, for example, planar

polycyclic aromatic hydrocarbons (PAHs), such as pyrene and perylene.^{37, 38} TTA (triplet-triplet annihilation) process can also lead to the formation of excimers and/or exciplexes. The annihilation ECL is generally produced as follows, where $^1A^*$ and $^3A^*$ represent singlet state species and triplet state species, respectively.



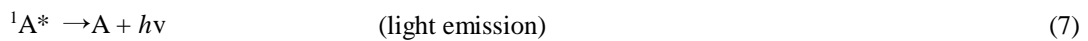
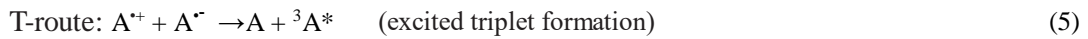
The enthalpy ($-\Delta H_{\text{ann}}$), which is directly related to the energy available in Eq.3 and Eq. 4, can be calculated from the redox potentials of reaction 1 and 2 as defined in Eq. 4. The value of $T \Delta S^0$ is usually estimated as 0.1 (0.1) eV. E_p is the cyclic voltammetric peak potential for each oxidation and reduction and 0.16 eV is a correction for $T \Delta S$ and the difference between E_p and the standard electrode potential.⁷

39

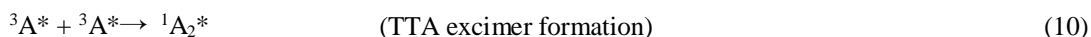
$$-\Delta H_{\text{ann}} = E^\circ(A^{+\bullet}, A) - E^\circ(A, A^{\bullet-}) - 0.1 \text{ eV} \quad (4)$$

The light emission process is defined as the singlet route ‘‘S-route’’ (Eqs. (1)–(3)),⁴⁰ if the ECL system has sufficient energy, which means the estimated enthalpy ($-\Delta H_{\text{ann}}$) is larger than the energy (E_s) required to produce the lowest excited singlet state from the ground state. The singlet state $^1A^*$ will be generated directly. When $E_s > -\Delta H_{\text{ann}}$, the triple state energy $^3A^*$ will be produced first, and $^1A^*$ will be generated by subsequent annihilation of $^3A^*$ (this energy transfer mechanism is named as triplet-triplet annihilation), following the so-called ‘‘T-route’’ (Eqs. (5)–(7)).⁴¹

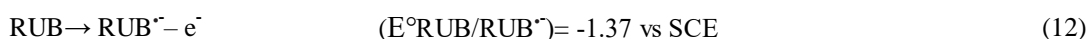
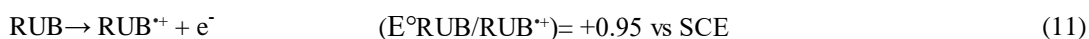
Or



When the reactions are related to the formation of excimers and exciplexes, the route is called ‘‘E-route’’ (Eqs. (8)–(10)):



The classic example of a molecule following the S-route is rubrene.^{5, 42} ECL spectrum is recorded when the potential was applied not only on the metal electrode (platinum and gold) but also on glassy carbon, producing the radical cation (RUB^{•+}) upon anodic oxidation and the radical anion (RUB^{•-}) upon cathodic reduction. The recombination of both electrogenerated radical ions (RUB^{•+} and RUB^{•-}) produce the excited state (RUB^{*}) which is able to emit light through the annihilation mechanism (Eq.13).



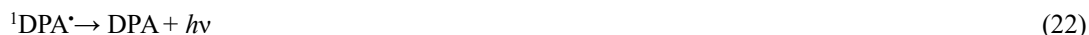
The ECL emission spectrum of rubrene (λ_{max} at ~540 nm) is identical to its fluorescence emission spectrum,⁴² which indicates that the ultimate product of the charge transfer is the lowest singlet RUB species, ¹RUB^{*}.

In addition, different ECL systems involving two different precursors can generate light emission. The “cross-reactions” mechanism between the radical cation of one species (A^{•+}) and the radical anion of a different species (D^{•-}) in order to produce ECL, is presented:



A classic example of triplet–triplet annihilation is the ECL of 9,10-diphenylanthracene (DPA)/TMPD (TMPD = N,N,N,N-tetramethyl-*p*-phenylenediamine) system in dimethylformamide.⁴³ The emitted ECL light is identical to DPA photoluminescence, indicating that ¹DPA^{*} is the ultimate product of charge transfer. This is due to the low enthalpy value required for the electron-transfer reaction of the DPA/TMPD system (2.03 eV), compared with the enthalpy value to reach the emitting species ¹DPA^{*}

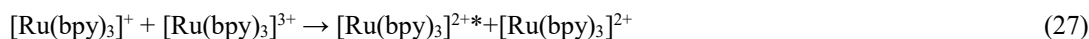
(3.00 eV). Therefore, such system is called “energy-deficient”¹⁸ and triplet intermediates are generated during the reaction process. In this case, the scheme is more complicated than the one depicted in Eqs. (19)-(22). The proposed mechanism involves triplet intermediates, called triplet or T-route (Eq. (5)).



The energy from the electro-oxidation and electro-reduction reactions is combined to provide sufficient energy to form the singlet excited state. The reactions of the DPA/TMPD system are present as below:



The ECL of many inorganic compounds, which include $[\text{Eu}(\text{bpy})_3]^{2+}/[\text{Os}(\text{bpy})_3]^{2+}$ or related species has been reported. In these metal complexes, because of spin-orbital coupling, spin-allowed excited states undergo rapid deactivation. The emitted light originates mainly from the lowest energy excited states via energy-sufficient routes. Other than ruthenium and osmium chelates, the ECL system of other inorganic species is inherently weak. For $[\text{Ru}(\text{bpy})_3]^{2+}$, an orange light ($\lambda_{\text{max}} = 610 \text{ nm}$) can be observed by generating electrochemically at the oxidized and reduced potential of the complex.⁴⁴ The reaction sequence is as follows (Eqs. (25)-(28)):



Annihilation ECL of $[\text{Ru}(\text{bpy})_3]^{2+}$ was reported for the first time on platinum electrode in acetonitrile solution.⁴⁵ Annihilation ECL has been extensively studied in different systems which include light-emitting electrochemical cells (LECs)⁴⁶ and microelectrodes to study sol-gel composites⁴⁷ containing $[\text{Ru}(\text{bpy})_3]^{2+}$ and diode-like CL⁴⁸ with polymer poly- $[\text{Ru}(\text{vbpy})_3](\text{PF}_6)_2$. To produce annihilation ECL, the potential window must be wide enough (from ~ 3.3 to 2 V), in order to generate the necessary radical

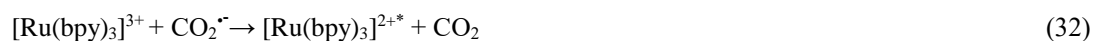
anions and cations via electrochemical reactions, and the related precursor molecules should be sufficiently stable to be evaluated via potentiodynamic measurement. In addition, the products with good PL efficiency often can be produced for the efficient generation of ion annihilation ECL. At last, sufficient exergonicity of the electron transfer reaction is required to produce the excited state.

1.3.2 Co-reactant pathway

ECL can be generated by a single potential step or one directional potential scanning in the presence of a luminophore and co-reactant. It depends on the polarity of the applied potential. Both the luminophore and the co-reactant species can first be oxidized or reduced at the electrode to form radicals, and an intermediate formed from the co-reactant, which then decompose to produce a powerful reducing or oxidizing species that can react with an oxidized or reduced luminophore to produce excited states with the concomitant light emission. This ECL mechanism is divided into two types, “oxidative-reduction” ECL and “reductive-oxidation” ECL. It is due to highly reducing intermediate species generated from the electrochemical oxidation of the co-reactant, or highly oxidizing ones produced by the electrochemical reduction of the related co-reactant.

1.3.2.1 Oxidative-reduction ECL

In 1977, Bard reported the oxalate and $[\text{Ru}(\text{bpy})_3]^{2+}$ system on a platinum electrode in acetonitrile as the first co-reactant ECL system.⁹ It showed that a new CL reaction occurred on the platinum electrode surface where oxalate and the fluorescent compound were oxidized. The electrochemical results suggest that $\text{CO}_2^{\cdot-}$ can be formed by an overall one-electron oxidation of oxalate, similar to the one observed in aqueous solutions.⁴⁹ The excitation process was based on the oxidation of oxalate to form $\text{C}_2\text{O}_4^{\cdot-}$, and its correspondent fast decomposition component are CO_2 and $\text{CO}_2^{\cdot-}$. The $\text{CO}_2^{\cdot-}$ can transfer an electron to $[\text{Ru}(\text{bpy})_3]^{3+}$ to produce $[\text{Ru}(\text{bpy})_3]^{2+*}$, which can emit light by returning to $[\text{Ru}(\text{bpy})_3]^{2+}$ (Eqs. (29)-(32)).



This co-reactant ECL reaction not only occurred in organic solution but also has been studied in an aqueous solution.⁵⁰ Oxalate can be oxidized as $C_2O_4^{\cdot-}$, then release CO_2 , producing a strongly reducing species $CO_2^{\cdot-}$ ($E^\circ = -1.9$ V vs. NHE).⁵¹ On carbon electrode, the oxidation peak of oxalate and $[Ru(bpy)_3]^{2+}$ was similar to that on oxide-covered Pt electrode, although with a higher overpotential compared to that on reduced Pt. In the presence of oxalate, the anodic current for $[Ru(bpy)_3]^{2+}$ was larger and the cathodic current, on the reverse scan, was smaller than in the absence of oxalate, showing that oxalate is not directly oxidized on the electrode surface directly, but in a catalytic reaction with $[Ru(bpy)_3]^{3+}$. The potential of oxalate oxidation is affected by pH and becomes less positive with an increase in pH. This report showed that the redox reaction occurred in 0.1M H_2SO_4 , but not in 1M H_2SO_4 . When the potential of oxalate is more positive than that for oxidation of $[Ru(bpy)_3]^{2+}$, orange light is emitted from Pt or carbon electrode surface in 0.1 M H_2SO_4 even at low concentrations of $[Ru(bpy)_3]^{2+}$ (0.1 mM) and at different concentrations of oxalate. Meanwhile, ECL intensity is strongly dependent on pH, as shown in Figure 3.⁵⁰ In neutral solution, ECL intensity is quite strong. No light was observed when only oxalate was oxidized and potentials sufficiently positive to trigger oxidation of $[Ru(bpy)_3]^{2+}$ are required. In total, the ECL intensity of $[Ru(bpy)_3]^{2+}$ -oxalate system is very stable, strong and constant in the aqueous solution.

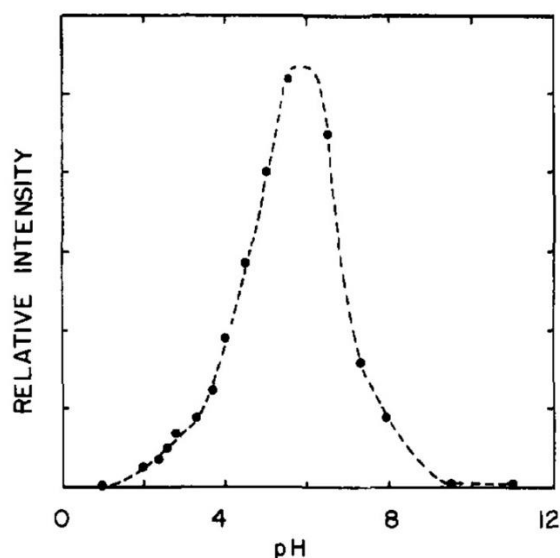


Figure 3. Dependence of the ECL intensity (at 610 nm) on the pH. The solution contained 1.0 mM $Ru(bpy)_3(ClO_4)_2$ and 6.0 mM $H_2C_2O_4$, with the pH adjusted by addition of NaOH to 0.1 M H_2SO_4 .⁵⁰

In an aqueous solution, ECL is generated via two pathways (Eqs. (33)-(39)). At first, $[Ru(bpy)_3]^{3+}$ is obtained by oxidation of $[Ru(bpy)_3]^{2+}$ on the electrode surface upon the anodic potential scanning. Then

$[\text{Ru}(\text{bpy})_3]^{3+}$ cation reacts with the oxalate ($\text{C}_2\text{O}_4^{2-}$) in the diffusion layer to form the oxalate radical anion ($\text{C}_2\text{O}_4^{\cdot-}$). This anion splits into a strong reductant ($\text{CO}_2^{\cdot-}$) and carbon dioxide (CO_2). $\text{CO}_2^{\cdot-}$ reduces the $[\text{Ru}(\text{bpy})_3]^{3+}$ to form the excited state $[\text{Ru}(\text{bpy})_3]^{2+*}$, or also reduces $[\text{Ru}(\text{bpy})_3]^{2+}$ to form $[\text{Ru}(\text{bpy})_3]^+$, which reacts with $[\text{Ru}(\text{bpy})_3]^{3+}$ to generate the excited state $[\text{Ru}(\text{bpy})_3]^{2+*}$. Orange light with $\lambda_{\text{max}} \sim 620$ nm was observed. The proposed mechanism of reaction between oxalate and $[\text{Ru}(\text{bpy})_3]^{2+}$ can be explained as follow.

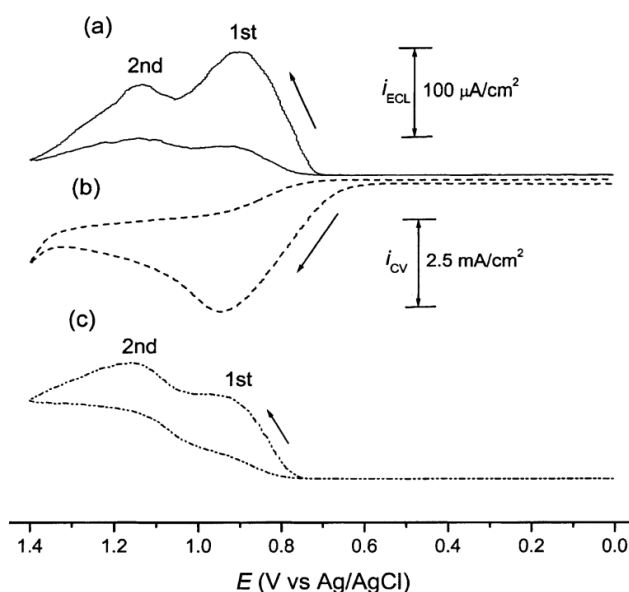
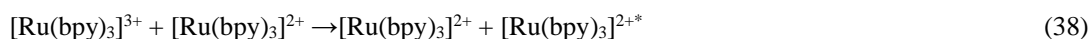


Figure 4. (a) ECL and (b) cyclic voltammogram of 1.0 nM $[\text{Ru}(\text{bpy})_3]^{2+}$ in the presence of 0.10 M TPrA with 0.10 M Tris/0.10 M LiClO_4 buffer (pH=8) at a 3 mm diameter glassy carbon electrode at a scan rate of 50mV/s. (c) As (a) but with 1.0 μM $[\text{Ru}(\text{bpy})_3]^{2+}$. The ECL intensity scale is given for (c) and should be multiplied by 100 for (a).⁵⁷

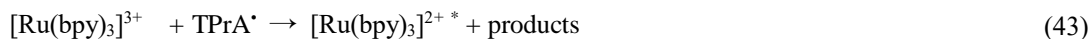
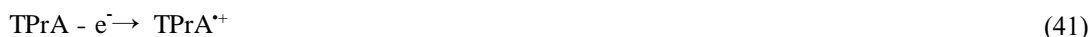
The CL of $[\text{Ru}(\text{bpy})_3]^{3+}$ with aliphatic amines was reported by Noffsinger and Danielson.⁵² Following this study, Leland and Powell reported $[\text{Ru}(\text{bpy})_3]^{2+}$ /tripropylamine (TPrA)⁵³ ECL system, which is another classical “oxidative-reduction” system. This system or related derivatives are commercially used

in ECL immunoassays and DNA analyses⁵⁴⁻⁵⁶ due to high ECL efficiency.

The ECL intensity for this system depends on the concentration of both $[\text{Ru}(\text{bpy})_3]^{2+}$ and TPrA species,⁵⁸ the solution pH and the electrode material, which commonly consists of a glassy carbon, platinum or gold electrode.⁵⁹ In general, the ECL response of this system as a function of applied potential consists of two waves. The first wave is associated to the direct oxidation of TPrA which can lead to the formation of reducing radicals (TPrA[•]) on the electrode surface, becoming smaller when the used concentration of $[\text{Ru}(\text{bpy})_3]^{2+}$ is higher, showed in Figure 4 a and c; the second wave is associated to oxidation of $[\text{Ru}(\text{bpy})_3]^{2+}$.⁵⁷ These two waves lead to the emission of light.

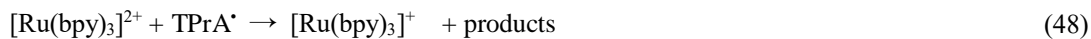
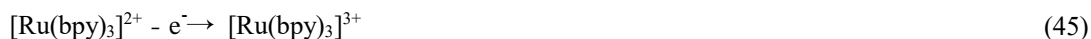
For this system, four possible reaction routes have been reported (Scheme 1, (Eqs. (40)-(44)).⁶⁰ Both $[\text{Ru}(\text{bpy})_3]^{2+}$ and TPrA are oxidized at the electrode surface to generate $[\text{Ru}(\text{bpy})_3]^{3+}$ and TPrA⁺. Afterwards, deprotonation of TPrA⁺ to produce TPrA[•] occurs, which then react with obtained $[\text{Ru}(\text{bpy})_3]^{3+}$ to produce the excited state $[\text{Ru}(\text{bpy})_3]^{2+*}$ and emit light.

Scheme 1:



In the second possible route (Scheme 2, Eqs.(45)-(50)), the first three steps are similar to the previous route, however the difference relies in the formation of $[\text{Ru}(\text{bpy})_3]^+$, generated from the reaction between $[\text{Ru}(\text{bpy})_3]^{2+}$ and TPrA[•]; then $[\text{Ru}(\text{bpy})_3]^+$ reacts directly with $[\text{Ru}(\text{bpy})_3]^{3+}$ to form the excited state $[\text{Ru}(\text{bpy})_3]^{2+*}$ and emit light.

Scheme 2:





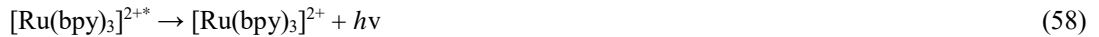
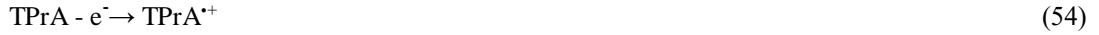
In the third route (Scheme 3, Eqs. (51)-(53)), only $[\text{Ru}(\text{bpy})_3]^{2+}$ is oxidized at the electrode surface, TPrA is oxidized by the generated $[\text{Ru}(\text{bpy})_3]^{3+}$. The overall ECL intensity of this process depends on the concentration of $[\text{Ru}(\text{bpy})_3]^{2+}$ and the ECL intensity is small when the concentration of $[\text{Ru}(\text{bpy})_3]^{2+}$ is low.

Scheme 3:



Finally, in the fourth route (Scheme 4, Eqs.(54)-(58)), the direct oxidation of TPrA occurs at the electrode and generates $\text{TPrA}^{\bullet+}$ and TPrA occurs. The subsequent reaction between $\text{TPrA}^{\bullet+}$ and $[\text{Ru}(\text{bpy})_3]^{2+}$ generates $[\text{Ru}(\text{bpy})_3]^+$, which then reacts with $\text{TPrA}^{\bullet+}$ to form the excited state $[\text{Ru}(\text{bpy})_3]^{2+*}$. The ECL route is in below,

Scheme 4:



Therefore, the excited state $[\text{Ru}(\text{bpy})_3]^{2+*}$ can be obtained via three different routes: (1) the oxidation of $[\text{Ru}(\text{bpy})_3]^+$ by $\text{TPrA}^{\bullet+}$ cation radicals; (2) the reduction of $[\text{Ru}(\text{bpy})_3]^{3+}$ by reacting with TPrA^{\bullet} free radicals; and (3) the annihilation reaction of $[\text{Ru}(\text{bpy})_3]^{3+}$ and $[\text{Ru}(\text{bpy})_3]^+$.

1.3.2.1 Reductive-oxidation ECL

The first reductive-oxidation co-reactant ECL reaction model is the $[\text{Ru}(\text{bpy})_3]^{2+}/\text{S}_2\text{O}_8^{2-}$ system, which was introduced independently by Bolletta et al. and White and Bard.⁶¹ They showed ECL production by the reaction between electrogenerated luminophores and the strong oxidizing intermediate $\text{SO}_4^{\bullet-}$,

generated from $S_2O_8^{2-}$ reduction in some organic solution and aqueous solution. In addition, $[Ru(bpy)_3]^+$ generated from reduction of $[Ru(bpy)_3]^{2+}$ is able to reduce $S_2O_8^{2-}$. No ECL is observed at potential up to -1.4 V vs. SCE in CH_3CN-H_2O solution, where $S_2O_8^{2-}$ is reduced directly at both GC and Pt electrodes. However, ECL is observed when the potential is biased more negative than the onset of $[Ru(bpy)_3]^{2+/+}$ reduction wave (-1.4 V), indicating that $[Ru(bpy)_3]^+$ is necessary to the production of the corresponding excited state species $[Ru(bpy)_3]^{2+*}$. Similar results were obtained in organic solvents, such as DMF for $[Os(bpy)_3]^{2+}$ and $[Ru(bpy)_3]^{2+}$, MeCN for $[Ru(bpy)_3]^{2+}$ and also in aqueous solutions for $[Cr(bpy)_3]^{3+}$.⁶² Actually, $S_2O_8^{2-}$ has been used as an effective quencher of $[Ru(bpy)_3]^{2+*}$ in aqueous solutions, suggesting that ECL efficiency is dependent on the concentration of $S_2O_8^{2-}$. The maximum intensity is obtained at 15-20 mM $S_2O_8^{2-}$ in solution containing $[Ru(bpy)_3]^{2+}$. Figure 5 demonstrates that more excited states are formed with the increase of $(NH_4)_2S_2O_8$ concentration until almost 18 mM. At a high $S_2O_8^{2-}$ concentration (>30 mM), the negligible ECL intensity is obtained, not only because the excited states are quenched by $S_2O_8^{2-}$, but also maybe because $S_2O_8^{2-}$ reacts with the electrogenerated $[Ru(bpy)_3]^+$ to give $[Ru(bpy)_3]^{2+}$, further decreasing the $[Ru(bpy)_3]^+$ steady-state concentration near the electrode surface.

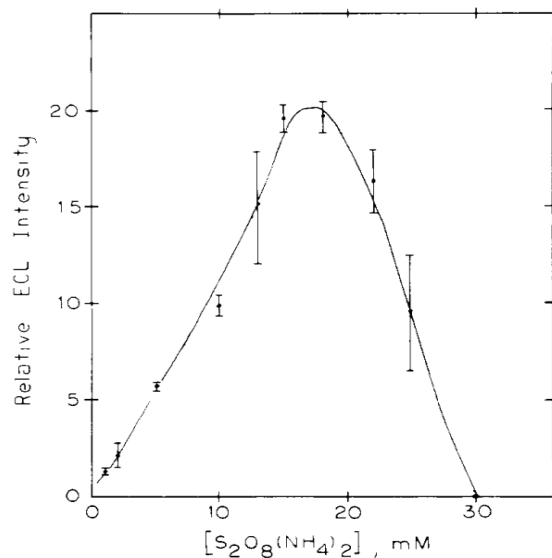
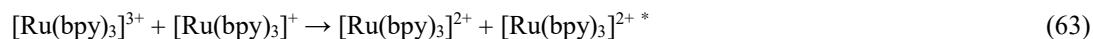
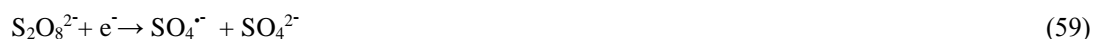


Figure 5. Relative ECL intensity as a function of $(NH_4)_2S_2O_8$ concentration in degassed MeCN- H_2O solution (1:1 by volume) containing 1mM $Ru(bpy)_3(PF_6)_2$.^[58]

The mechanism of $[Ru(bpy)_3]^{2+}/S_2O_8^{2-}$ system can be explained as follow. The $S_2O_8^{2-}$ is reduced at the electrode surface and generates $SO_4^{\cdot-}$, which reacts with $[Ru(bpy)_3]^+$, producing $[Ru(bpy)_3]^{2+*}$. Then annihilation pathway occurred. This reaction process can also be used for the $[Os(bpy)_3]^{2+}/S_2O_8^{2-}$

system,⁶² [Ru(phen)₃]²⁺/S₂O₈²⁻ system⁶³ and other derivatives systems.⁶⁴⁻⁶⁶



Benzoyl peroxide (BPO) (Figure 6) is another effective co-reactant for reductive-oxidation ECL, which often has reaction with organic systems, like rubrene,⁶⁷ 9,10-DPA,⁶⁸ fluoranthene, and anthracene. Peroxides can be used as co-reactants because they produce oxidizing agents when they are reduced. The electron density of the oxygen-oxygen (O-O) bond is the crucial factor to produce oxidizing agents.⁶⁹ Usually, the lower electron density on the O-O bond in peroxides, the stronger reactive oxidizing agents can be produced.⁷⁰ This is due to the strong effect on the electron density caused by functional groups attached to the O-O bond, thus, oxidizing agents generated from peroxides that contained electron-withdrawing groups are more reactive than those formed from peroxides with electron-donating groups.

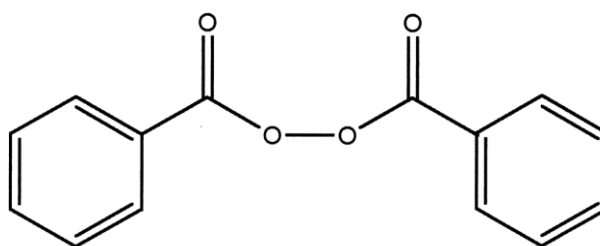
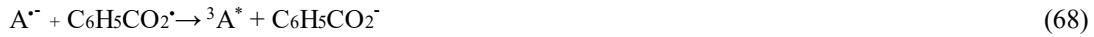
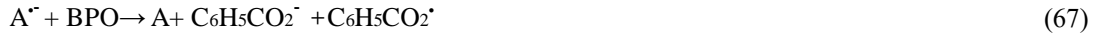


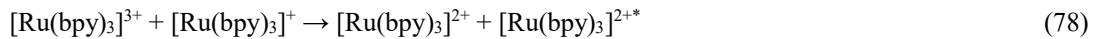
Figure 6. Molecular structure of benzoyl peroxide.⁷¹

BPO is electrochemically reduced via an overall two-electron mechanism. BPO is reduced to benzoate anion (C₆H₅CO₂⁻) and benzoate radical (C₆H₅CO₂[·]). The benzoate radical is further reduced to the benzoate anion (C₆H₅CO₂⁻). When the potential is negative enough, the benzoate radical formed is energetic deficient by reacting with aromatic hydrocarbon cation radicals to generate the excited states and emits light. "A" is marked as the luminophore.





The $\text{C}_6\text{H}_5\text{CO}_2^\cdot$ formed is energetic enough to react with $[\text{Ru}(\text{bpy})_3]^{2+}$ to form $[\text{Ru}(\text{bpy})_3]^{2+*}$, because the redox potential value for the $(\text{C}_6\text{H}_5\text{CO}_2^\cdot/\text{C}_6\text{H}_5\text{CO}_2^-)$ couple is +1.29 V vs. SCE.⁷¹ The mechanism of ECL produced with $[\text{Ru}(\text{bpy})_3]^{2+}$ is showed here.



1.4 Luminophores

ECL luminophores are entities or moieties that undergo a redox reaction to generate light by applying potential on the electrode surface with or without an ECL co-reactant. There are three main categories: 1) inorganic complexes, including different organometallic complexes; 2) organic molecules, like polycyclic aromatic hydrocarbons; and 3) nanoparticles, like silicon nanoparticles, gold nano-clusters and quadrupolar fluorescent dye nanoparticles. Nowadays, many research works are exploiting new type ECL luminophores to develop analytical applications.

1.4.1 Metal chelates

The widely used inorganic luminophores are tris(bipyridine)ruthenium(II) ion $[\text{Ru}(\text{bpy})_3]^{2+}$ and its derivatives, which show outstanding luminescent properties, due to their fully reversible one-electron

transfer electrochemical process, good stability and ECL efficiency in aqueous media, tunable solubility in various nonaqueous or aqueous media and excellent bio-capabilities with various of analytes.

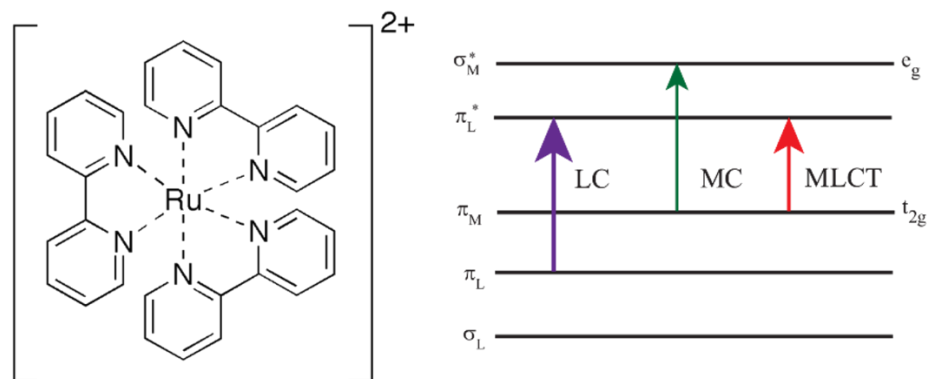


Figure 7. Structure and transitions of $[\text{Ru}(\text{bpy})_3]^{2+}$.⁷²

$[\text{Ru}(\text{bpy})_3]^{2+}$ is an octahedral complex with yellow-orange color, containing a central low spin d^6 Ru(II) ion and three bidentate bpy ligands. Its absorption wavelength is at 454 nm and the emission wavelength is at 610 nm.

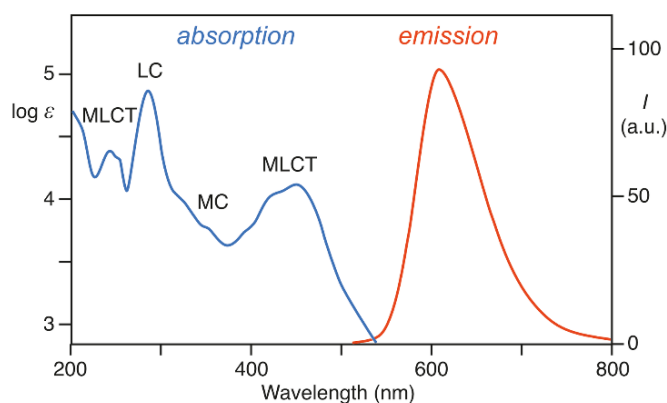


Figure 8. Absorption and emission spectra of $[\text{Ru}(\text{bpy})_3]^{2+}$.⁷²

The complex is chiral with D_3 symmetry. In its lowest lying triplet excited state, the molecule is thought to attain lower C_2 symmetry, since the excited electron is localized primarily on a single bipyridyl ligand. The excited-state configurations result from an electron residing in a bpy π^* orbital interacting with the d^5 Ru π orbital. The metal-centred (MC) excited states occurred by an electron promotion from π orbital to σ orbital of metal. The promotion of an electron from π to π^* orbital of ligand produce the ligand-centred (LC) excited states.⁷² One electron excitation from a π_M metal orbital to the π_L^* ligand orbitals

rise to the metal-to-ligand charge transfer (MLCT) excited states.

In order to improve molecular recognition ability, the majority of studies have focused in designing or modifying the ligands of ruthenium complexes. Including $[\text{Ru}(\text{bpy})_3]^{2+}$ as a standard, the other compounds are $\text{Ru}(\text{L})_x^{n+}$, which can be $[\text{Ru}(\text{terpy})_2]^{2+}$ (2,2',2''-terpyridine=terpy), $[\text{Ru}(o\text{-phen})_3]^{2+}$ (1,10-phenanthroline=*o*-phen) and $[\text{Ru}(\text{bpz})_3]^+$ (tris(2,2'-bipyrazyl)=bpz).^{66, 73}

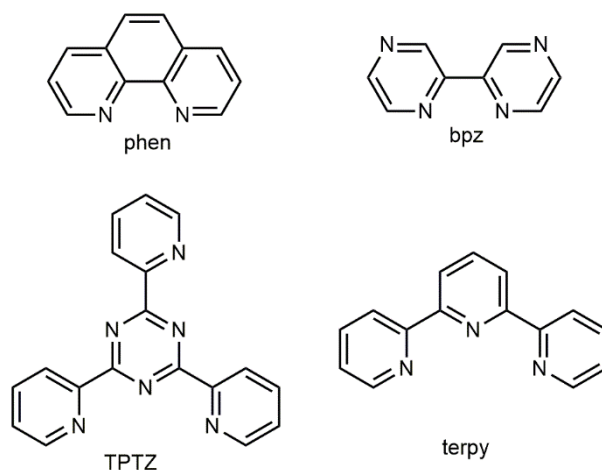


Figure 9. Structure of 1,10-phenanthroline (phen); 2,2'-bipyrazine (bpz); 2,4,6-tripyridyl-2-triazine (TPTZ); 2,2',2''-terpyridine (terpy).^{66, 73}

All compounds display one-electron oxidation and reduction peaks by using cyclic voltammetry. ECL of these compounds was obtained via annihilation route, identified as the lowest triplet MLCT state, or via co-reactant schemes for $[\text{Ru}(\text{bpz})_3]^{2+}$. Notably, ECL light intensity of $[\text{Ru}(\text{bpy})_3]^{2+}$ is the most intense. Steady-state ECL for $[\text{Ru}(\text{bpy})_3]^{2+}$ was generated at a rotating ring-disk electrode (RRDE) and yielded an ECL efficiency of 5–6%. Recently, $[\text{Ru}(\text{bpy})_3]^{2+}$ ECL have been widely used for the determination of numerous co-reactants, like oxalate, alkylamines, amino acids and etc.⁷⁴⁻⁷⁸ More importantly, when coupled with TPrA via co-reactant route, it has found broad applications in commercial ECL immunoassays and clinical analysis as a sensitive label detection at subpicomolar concentration. It is worth mentioning that the ECL efficiencies of coreactant $[\text{Ru}(\text{bpy})_3]^{2+}$ not only are dependent on photoluminescence quantum yields, but also are sensitive to minor structure changing of ruthenium complexes. For example, Ru(II) heteroleptic complexes ($[\text{Ru}(\text{BPS})_n(\text{bpy})_{3-n}]^{(2n-2)+}$) bearing mixed 2,20-bipyridine (bpy) and bathophenanthrolinedisulfonate (BPS) ligands were studied, observing that when *n* decreases from 3 to 1, the net charge changes from -4 to 0. Surprisingly, ECL intensities increased approximately 5 to 26 times with respect to decrease of *n* from 3 to 1 under a constant potential with the usage of TPrA as a coreactant.^[69] Thus, this work prove that the ECL efficiency was related to the

structure of complex.

To extend ECL applications and improve ECL efficiency, many efforts have been made to find new coreactants for $[\text{Ru}(\text{bpy})_3]^{2+}$ ECL. Glyoxal, methylglyoxal and glyoxylic acid exhibited higher ECL intensity than oxalate.^[70] This is caused by the electrogenerated hydroxyl radicals, implying that compounds electrochemically generated hydroxyl radicals can be expanded to be used as coreactant.

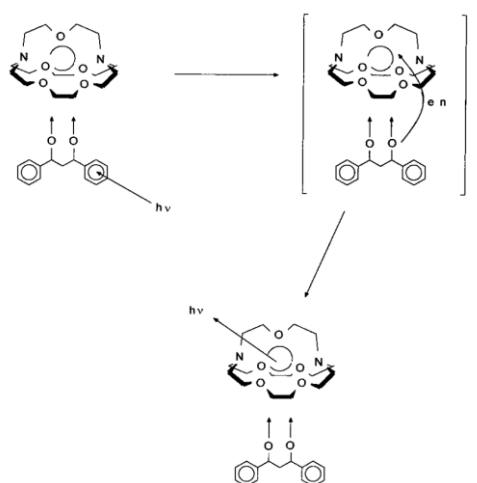


Figure 10. Photophysical processes for the β -Diketonate (L-) Ligand.⁷⁹

Even though $[\text{Ru}(\text{bpy})_3]^{2+}$ has become the most famous used ECL-active label, its broad emission bands can be a disadvantage in analytical applications. Thus, alternative labels emitting at other wavelengths and with narrower emission bands for ECL methods are thus of interest. Many trivalent lanthanide complexes have attracted attention as potential ECL labels, because they display narrow emission spectra, high photoluminescence efficiencies, large Stokes' shifts (~ 300 nm) and long excited-state lifetimes.⁸⁰⁻⁸² The first report of these compounds described the observation of intermolecular energy transfer occurred from exciplex to europium chelate directly, resulting in ECL of europium complex via exciplex-sensitized luminescence. Exciplex was formed by the radical cation of tri-*p*-tolylamine and either the benzophenone or dibenzoylmethane radical anions. Excited states are formed by an energetic electron transfer reaction where the energy donor was formed electrochemically, not optically. However, no direct ECL of the Eu(III) chelate was found in that study.⁸³ Further studies showed the direct ECL of rare earth chelate, $(\text{TBA})\text{Eu}(\text{DBM})_4$ and $(\text{TBA})\text{Eu}(\text{TTA})_4$.⁷⁹ Intermolecular energy transfer occurred from the lowest excited state of an energy donor-neutral ligands to the acceptors-anionic ligands states of the rare earth chelate.⁸⁴ Such intramolecularly transfers of energy from the ligands to the metal-centred 4f state with subsequent narrow band emissions, has been observed by spectroscopic studies. ECL was obtained

for the chelates and mixed ligand systems in the presence of $S_2O_8^{2-}$ in acetonitrile solutions and was attributed to the electron-transfer reaction between the reduced bound ligands and $SO_4^{\cdot-}$, also called “ligand-sensitization” route.⁷⁹

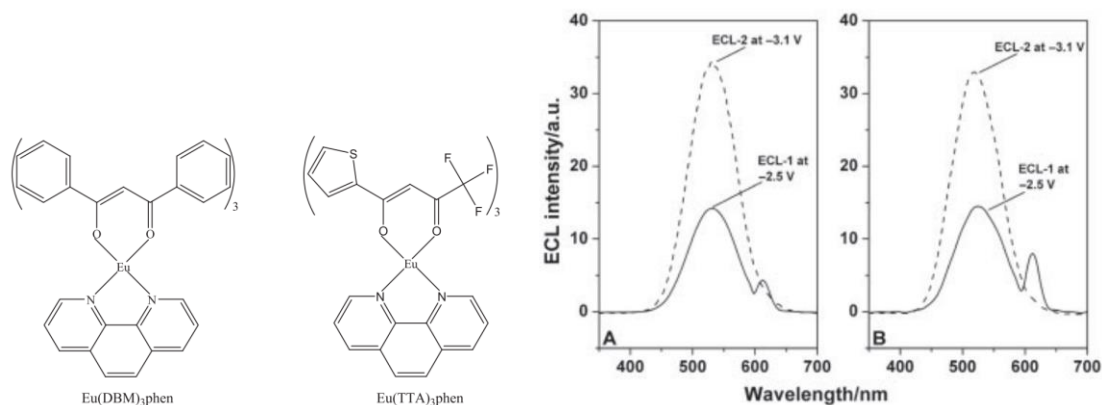


Figure 11. Structural formula of $Eu(DBM)_3phen$ and $Eu(TTA)_3phen$ and ECL spectra at different potentials of (A) $Eu(DBM)_3phen$ and (B) $Eu(TTA)_3phen$ all in 0.1 mol/L $TBABF_4$ in the presence of $(TBA)_2S_2O_8$ in acetonitrile solution, (—) ECL-1 spectra at -2.5 V; (---) ECL-2 spectra at -3.1 V.⁸⁵

After 10 years, Yu et al.⁸⁵ reported the cathodic ECL of acetonitrile–ternary Eu(III) complex systems using a gold electrode. ECL was also obtained via ligand-sensitization route. For the first step, $S_2O_8^{2-}$ was reduced to $SO_4^{\cdot-}$, which further to react with ligand radical dianions, generating nonemissive ligand-excited states, which then underwent intramolecular energy transfer to the Eu(III) f orbitals to form the excited states $Eu(III)^*$ and emit light at 610 nm with narrow peak. The ECL intensity of $Eu(TTA)_3phen$ was also much stronger than the obtained for $Eu(DBM)_3phen$, which was attributed to closer triplet-state levels of TTA to the resonance energy level of Eu(III), causing a more efficient the intramolecular energy transfer.

However, only a few researches reported ECL behavior of europium complex, thus, a further study of such systems, in order to better understand the ECL mechanism and to prove its applicability in diagnostic field is needed.

1.4.2 Organic luminophores

The earliest organic ECL luminophore involved polyaromatic hydrocarbons(PAHs), followed by the studies of PAHs, and other organic systems including luminol, polymers^{86, 87} and the amino acid tryptophan have⁸⁸ also been extensively investigated.

Luminol (5-amino-2,3-dihydro-1,4-phthalazinedione) is an inexpensive classic organic reagent

considered as an efficient ECL luminophore or label, able to generate a strong ECL signal in presence of H_2O_2 . Luminol is a yellow-colored crystalline solid powder and soluble in most polar organic solvents. It is a diprotic acid (denoted as LH_2) with pK_a values of 6.74 and 15.1. Luminol as a famous CL probe, show relatively high CL around its optimal pH (9.5), although it generates extremely low CL under physiological conditions (pH7.5).

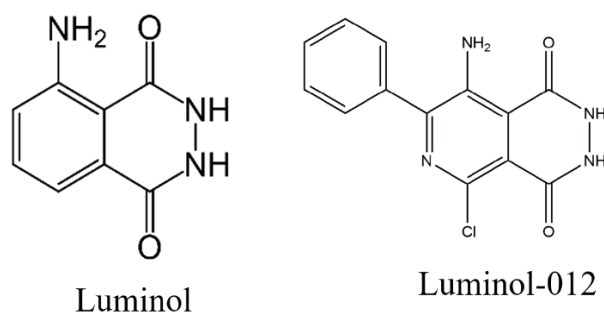


Figure 12. Structure of Luminol and Luminol-012.^{89, 90}

Luminol ECL have been widespread used for determination of H_2O_2 ,⁹¹ glucose, glucose oxidase,⁹² enzymes,⁹³ and many studies have been performed in order to enhance its ECL intensity^{94, 95} and for cell imaging.⁹⁶ Drugs, like bromhexine hydrochloride can be selectively detected in biological samples based on its quenching effect on luminol- H_2O_2 ECL system.⁹⁷ Generally, ECL of luminol is often produced in alkaline solution in the presence of hydrogen peroxide upon electro-chemical oxidation. However, in neutral pH solutions, strong luminol ECL has been obtained by modifying the electrode surface. Cui et al. studied the ECL behavior of luminol on various modified electrodes with gold nanoparticles of different size in neutral solution.⁹⁸ Two anodic luminol ECL were obtained on a gold nanoparticle self-assembled gold electrode in neutral pH conditions, although with a 16-nm-diameter gold nanoparticle modified electrode, the most intense ECL signals were observed. This allows the development of luminol ECL for the sensitive detection of biologically important compounds in physiological pH, due to excellent biocompatible properties of gold nanoparticles. Xu et al. reported the detection of H_2O_2 , glucose, and glucose oxidase activity by producing luminol ECL on stainless steel electrode.⁹⁹ This study shows the possible use of stainless steel electrodes as a highly promising material for ECL applications, such as ECL biosensing, disposable sensors, and wearable sensors. The ECL mechanism of luminol in the presence of hydrogen peroxide in alkaline medium is well studied and could be briefly described as

follow: at first, luminol is deprotonated to generate an anion LH⁻ under alkaline solution; subsequently, the LH⁻ can be electro-oxidized to form an intermediate which undergoes further electro-oxidation in the presence of H₂O₂ to produce excited state 3-aminophthalate; the excited state 3-aminophthalate finally returns to ground state and emit lights at 410 nm.

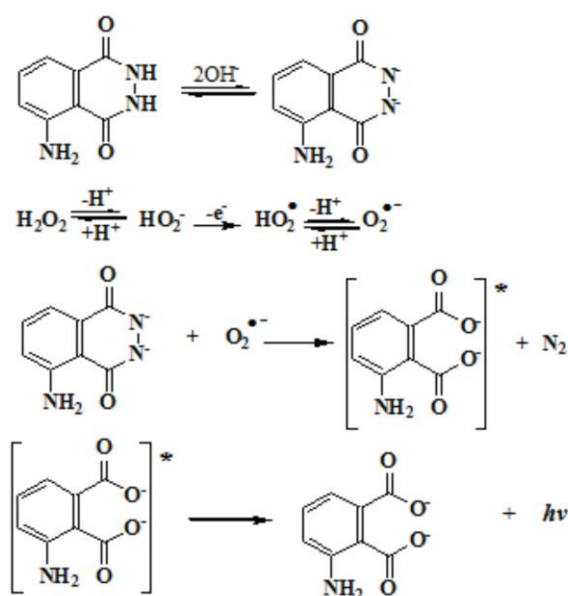


Figure 13. Reaction mechanism for the luminol–H₂O₂ ECL system.⁹⁹

L-012, a new luminol analog with higher self-luminescence, has presented higher activity than classical luminol. Thus, L-012 is rapidly emerging as a popular CL probe for the detection of reactive oxygen species (ROS).⁸⁹ Although ECL generation on L-012 is less reported, a few works involving cell imaging on modified indium tin oxide (ITO) surface. Recently, Jiang et al.¹⁰⁰ used single lithium iron phosphate (LiFePO₄, LFP) nanoparticles on the surface of indium tin oxide (ITO) electrodes for enhancing ECL generation from L-012 and hydrogen peroxide at a low voltage of 0.5V. The enhancement of ECL should be ascribed to the formation of FePO₄ from LFP particles during the charging process, which includes a mixture of Fe²⁺ and Fe³⁺ to enhance the production of oxygen intermediates from water. The decrease in the voltage minimize the electrochemical interruption of the cellular activity, which offers a special strategy to produce more realistic information of cells. Moreover, further enhancement of the ECL intensity from the nanoparticles can be performed in order to improve the temporal resolution and monitor the dynamic behavior of cellular activity.

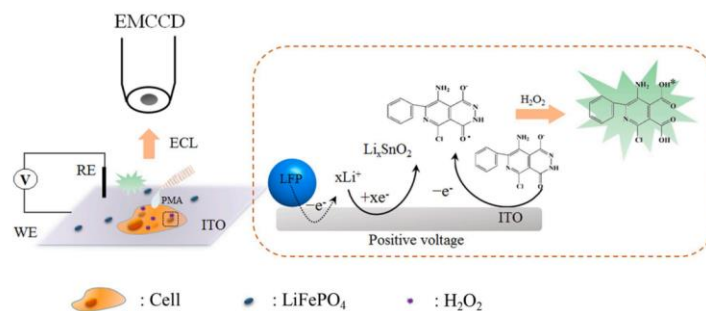


Figure 14. Schematic ECL mechanism based on lithium migration between single LFP particle and ITO surface for the local sensing of hydrogen peroxide efflux from single cells.¹⁰⁰

Nowadays, more studies about L-012 ECL are emerging, where this compound is used as biosensors for sensitive detection of biologically important compounds, cell imaging or enhancement of its ECL efficiency.

1.4.3 Nanoparticle systems

The silicon nanocrystal quantum dots was the first studied nanomaterial for ECL.¹⁰¹ Electron-transfer annihilation of electrogenerated positively and negatively charged nanocrystals radicals results in the production of excited states in solution, generating visible light. Furthermore, the coreactant pathway led to intense ECL emission when $C_2O_4^{2-}$ and $S_2O_8^{2-}$ were added to Si nanocrystals solution. Later, other kinds of semiconductor nanocrystals, called quantum dots, such as CdSe,¹⁰² CdS,¹⁰³ CdTe,¹⁰⁴ ZnS,¹⁰⁵ have been used as ECL emitters and some of those i.e. like CdS,¹⁰⁶ CdTe, have found applications in the biosensors field.

Besides quantum dots, other miscellaneous nanomaterials, like graphene and its related material,¹⁰⁷ graphite-like carbon nitride,¹⁰⁸ carbon nanodots,¹⁰⁹ have been used as promising ECL luminophores due to their characteristic-structure and properties, controllable size and shape and tunable electron-transfer. The possible ECL mechanism of graphite-like carbon nitride(C_3N_4) was reported recently.¹⁰⁸ TEA $^{\bullet}$, deprotonated by TEA $^{+}$, react to electrogenerated $C_3N_4^{+}$ to produce $C_3N_4^*$ with light emission by subsequently returning to C_3N_4 . Therefore, C_3N_4 was used as electrode for detection of Cu^{2+} and rutin. Au-functionalized C_3N_4 nanohybrids showed improved ECL intensity and stability of ECL immunosensors for detection of CEA (carcinoembryonic antigen).¹¹⁰ Silicon NPs doped with $[Ru(bpy)_3]^{2+}$ /in outer shell as red emitter and fluorescein isothiocyanate inside the shell as green coding

dye (RFSiNPs) were used as light emitting diodes.¹¹¹ By changing the molar ratio of doped dyes, the optical coding can be improved, which allows the use of this dual-dyes coped Si NPs (RFSiNPs) to determine different analytes in a single sample.

The combination of ECL and stimuli-responsive microgels functionalized with ruthenium complex derivatives have been reported recently.¹¹² ECL intensity can change reversibly by changing temperature. A reversible ECL amplification correlated with the swell-collapse transition of the microgels reach to 2 orders of magnitude was demonstrated in stimuli-responsive 100-nm microgel particles.

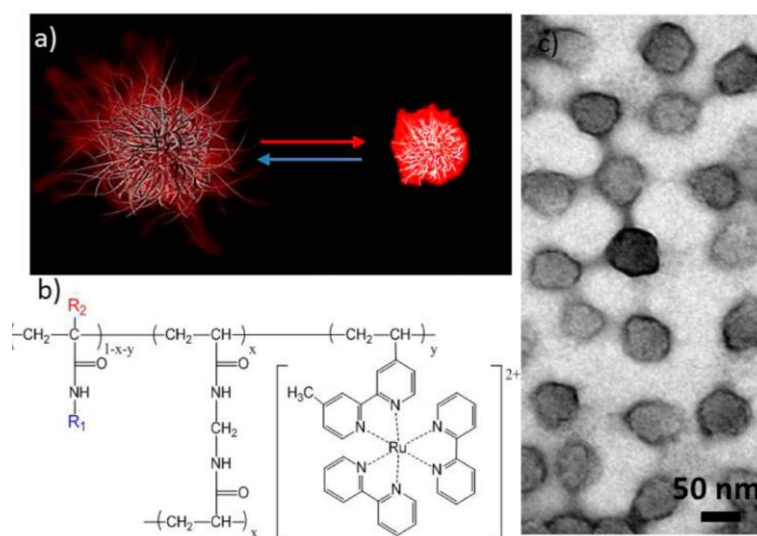


Figure 15. a) Schematic representation of the swell-collapse transition of the thermoresponsive ECL microgel; b) chemical structure of the cross-linked microgels with different chemical groups R1 and R2; c) transmission electron microscopy image of dried microgels.¹¹²

When temperatures increases, the thermo-responsive microgels collapse causes a decrease of the distance between adjacent redox sites. The decrease of this distance favors the charge diffusion in the redox polymers by electron-hopping from ruthenium site to site, which enhances the electrocatalytic oxidation of the coreactant. Both electrons and charge-compensating counterions occurs between the ruthenium sites simultaneously, thus increasing ECL intensities *via* annihilation mechanism. Such ECL enhancement related to the distance dependence offers the opportunity to develop tunable ECL resonance energy-transfer nanomaterials for multicolor emission.

The application of upconversion material was less studied in ECL field. Up-conversion, is a process in which the sequential absorption of two or more photons give rise to an emission wavelength shorter than excitation wavelength, also named as “anti-Stoke emissions”. For example, it is first time to mention that

a graphene-upconversion material exhibit a cathodic hot electron-induced ECL emission.¹¹³ The ECL intensity of the graphene-upconversion nanocomposite was increased by about 5-fold, which makes this synthesized functionalized graphene-based hybrid materials an interesting alternative for optoelectronics, microelectronics and ECL based-sensors.

1.5 ECL applications

ECL has shown great potential for various analytical applications. Recently, ECL techniques have been introduced for imaging, lasers, lighting and up-conversions devices.

ECL analytical applications have also been developed for biomedical applications, such as immunoassays,¹¹⁴ DNA detection,¹¹⁵ aptamer and nucleic acid sensors.¹¹⁶ Compared to other detection systems, this approach has many advantages including no usage of a radioactive isotope, a wide linear dynamic range, rapid measurement, disposal and storage of samples, allowing multiple labelling of the same molecules without affecting the immunoreactivity or hybridization of the probes. One of the most important applications of ECL is in the field of immunoassay. $[\text{Ru}(\text{bpy})_3]^{2+}$ can be modified and formed as active labels for proteins, nucleic acids, and other molecules.¹¹⁷ Luminol-based ECL is widely used in immunoassays for a long time.¹¹⁸ When nanoparticles, like Pd nanoparticles, ZnO nanoparticles, were introduced, the sensitivity of these immunoassays was improved.

For example, a sandwich-type immunosensor based on luminol ECL with Pd nanoparticles and glucose oxidase as synergetic catalysts were proposed (Figure 16). Pd nanoparticles can not only catalyze ECL reaction but also retain the activity of glucose oxidase because of its biocompatibility. This immunosensor was successfully used for the detection of α 1-fetoprotein with rather a low detection limit.^{119, 120}



Figure 16. Representation of ECL-based sandwich-type immunosensor and the synergetic catalysis effect of GOD and PdNPs for ultrasensitive immunoassay of AFP.¹²⁰

DNA detection is another important analytical application. Recently, DNA-gold nanoparticles bio-barcode assay has shown great promises in the detection of nucleic acid due to the unique non-enzymatic means of amplification of Au nanoparticles. Hence, the combination between ECL and DNA-Au nanoparticle bio-barcode method for DNA detection has been developed.¹²¹ In this system, an ECL nanoprobe was fabricated that relied on a DNA-gold nanoparticle modified by using $[\text{Ru}(\text{bpy})_3]^{2+}$ labeled cysteamine for boosting the ECL signal. This probe allows limit of an extremely low quantity (100 fM) and the assay exhibits excellent selectivity for single-mismatched DNA detection even in human serum. ECL imaging technology provides a facile method to study the microenvironment in the close vicinity of the electrode surface. From this technology, the image of surface electrochemical activity distribution with the location, size, and geometry of individual active regions can be obtained. With the development of the ECL techniques, more potential applications are expected to be explored.

1.6 Conclusions

ECL has been established as a powerful analytical tool for the determination of a wide range of analytes and for understanding fundamental questions in chemistry, biology, and physics. The clinical application of ECL also facilitates other new applications, like food safety, water safety, and environmental monitoring.

More studies about ECL are aimed to exploit new ECL systems, such as new organic luminophores, nanomaterial systems, to improve the ECL efficiency and combine ECL with other techniques to extend

its applications. The ECL of $[\text{Ru}(\text{bpy})_3]^{2+}/\text{TPrA}$ or luminol system is obtained generally at high potential, which limits some application to detect the analyte that oxidized easily at high potential, so exploiting suitable electrodes generating ECL at low potential or even at negative potential are needed. Electrochemiluminescence (ECL) with near-Infrared (NIR) emission has attracted attention to become a powerful analytical tool in biomedical and diagnostic fields in terms of its versatility, high stability and near zero background. Studies of the new ECL system with NIR emission that can show less photochemical damage and lower background interference are still in the progress.

References

1. Lee, W.-Y., *Microchimica Acta* 1997, 127 (1), 19-39.
2. Forster, R. J.; Bertoncello, P.; Keyes, T. E., *Annual review of analytical chemistry* 2009, 2, 359-85.
3. K. S. V. Santhanam and A. J. Bard, *Journal of the American Chemical Society* 1965.
4. Dufford, R. T.; Nightingale, D.; Gaddum, L. W., *Journal of the American Chemical Society* 1927, 49 (8), 1858-1864.
5. Maricle, D. L.; Maurer, A., *Journal of the American Chemical Society* 1967, 89 (1), 188-189.
6. Maricle, D.; Zweig, A.; Maurer, A.; Brinen, J., *Electrochimica Acta* 1968, 13 (5), 1209-1220.
7. Visco, R.; Chandross, E., *Electrochimica Acta* 1968, 13 (5), 1187-1196.
8. Nurhan E. Tokel, A. J. B., *Journal of the American Chemical Society* 1971, 94, 2862-2863.
9. Chang, M.-M.; Saji, T.; Bard, A. J., *Journal of the American Chemical Society* 1977, 99 (16), 5399-5403.
10. Leland, J. K.; Powell, M. J., *Journal of the Electrochemical Society* 1990, 137 (10), 3127.
11. Bertoncello, P.; Forster, R. J., *Biosensors & bioelectronics* 2009, 24 (11), 3191-200.
12. Dennany, L.; Forster, R. J.; Rusling, J. F., *Journal of the American Chemical Society* 2003, 125 (17), 5213-5218.
13. Zamolo, V. A.; Valenti, G.; Venturelli, E.; Chaloin, O.; Marcaccio, M.; Boscolo, S.; Castagnola, V.; Sosa, S.; Berti, F.; Fontanive, G., *ACS nano* 2012, 6 (9), 7989-7997.
14. Bertoncello, P.; Forster, R. J., *Biosensors and Bioelectronics* 2009, 24 (11), 3191-3200.
15. Bebb, H. B.; Williams, E. W., Chapter 4 Photoluminescence I: Theory. 1972, 8, 181-320.
16. Vo-Dinh, T., *digital Encyclopedia of Applied Physics* **2003**. Doi:10.1002/3527600434.eap063
17. Herring, P. J., *Nature* 1977, 267 (5614), 788-793.
18. Maloy, J.; Bard, A. J., *Journal of the American Chemical Society* 1971, 93 (23), 5968-5981.
19. Bos, A. J. J., *Radiation Measurements* 2006, 41, S45-S56.
20. Zink, J. I., *Accounts of Chemical Research* 1978, 11 (8), 289-295.
21. Sehgal, C.; Steer, R. P.; Sutherland, R. G.; Verrall, R. E., *The Journal of Physical Chemistry* 1977, 81 (26), 2618-2620.
22. Hamers, D.; van Voorst Vader, L.; Borst, J. W.; Goedhart, J., *Protoplasma* 2014, 251 (2), 333-47.
23. Hallaj, T.; Amjadi, M.; Manzoori, J. L.; Shokri, R., *Microchimica Acta* 2014, 182 (3-4), 789-796.
24. Toyo'oka, T., *Talanta* 2003, 60 (2-3), 467-475.
25. Khan, P.; Idrees, D.; Moxley, M. A.; Corbett, J. A.; Ahmad, F.; von Figura, G.; Sly, W. S.; Waheed, A.; Hassan, M. I., *Applied biochemistry and biotechnology* 2014, 173 (2), 333-55.

-
26. Chen, X.; Zhang, J.; Li, Y.; Han, S., *Luminescence : the journal of biological and chemical luminescence* 2018, 33 (5), 962-967.
 27. Klopff, L. L.; Nieman, T. A., *Analytical Chemistry* 1983, 55 (7), 1080-1083.
 28. Lan, Z.-H., Oklahoma State University: 1996.
 29. Merenyi, G.; Lind, J.; Erikson, T. E., *Journal of the American Chemical Society* 1986, 108 (24), 7716-26.
 30. Lind, J.; Merenyi, G.; Eriksen, T. E., *Journal of the American Chemical Society* 1983, 105 (26), 7655-7661.
 31. Piper, W. W.; Williams, F. E., *Physical Review* 1955, 98 (6), 1809-1813.
 32. Jiangbo Ouyang, F.-R. F. F., Allen J. Bard, *Journal of the Electrochemical Society* 1989, 136, 1033-1039.
 33. Pope, M., Kallmann, H. & Magnante, P., *Journal of Chemical Physics* 2004, 38, 2042-2043.
 34. Chang, J.; Hercules, D.; Roe, D., *Electrochimica Acta* 1968, 13 (5), 1197-1207.
 35. Parker, C. A.; Short, G. D., *The Journal of Physical Chemistry* 1968, 72 (8), 3071-3071.
 36. Werner, T. C.; Chang, J.; Hercules, D. M., *Journal of the American Chemical Society* 1970, 92 (4), 763-768.
 37. Werner, T. C.; Chang, J.; Hercules, D. M., *Journal of the American Chemical Society* 1970, 92 (19), 5560-5565.
 38. Hayashi, S.; Etoh, H.; Saito, S., *Japanese journal of applied physics* 1986, 25 (9A), L773.
 39. Hercules, F. E. B. D. M., *The Journal of Physical Chemistry* 1979, 83, 2203-2209.
 40. Faulkner, L. R.; Tachikawa, H.; Bard, A. J., *Journal of the American Chemical Society* 1972, 94 (3), 691-699.
 41. Ernest L. Ritchie, P. P., R. Mark Wightman, *Journal of the American Chemical Society* 1997, 119, 11920-11925.
 42. J. Chang, D. M. H. D. K. R., *Electrochimica Acta* 1968, 13, 1197-1207.
 43. J. Bard, K. G. B. A., *Journal of Electroanalytical Chemistry and Interfacial Electrochemistry* 1975, 65, 945-962.
 44. Bard, W. L. W. A. J., *The Journal of Physical Chemistry* 1979, 83, 1350-1357.
 45. Sharma, D.; Lee, J.; Shin, H., *Biosensors & bioelectronics* 2018, 107, 10-16.
 46. Kong, S. H.; Lee, J. I.; Kim, S.; Kang, M. S., *ACS Photonics* 2017, 5 (2), 267-277.
 47. Meyer, M. S. T. J., *Chemistry of Materials* 1999, 11, 1186-1189.
 48. Karolyn M. Maness, R. H. T., Thomas J. Meyer, Royce W. Murray, R. Mark Wightman, *Journal of the American Chemical Society* 1996, 118, 11609-11616.
 49. Pannell, K. H.; Yee, W.; Lewandos, G. S.; Hambrick, D. C., *Journal of the American Chemical Society* 1977, 99 (5), 1457-1461.
 50. Israel Rubinstein, A. J. B., *Journal of the American Chemical Society* 1981, 103, 512-516.
 51. J. Butler, A. H., *Radiation Physics and Chemistry* 1979, 15, 603-612.
 52. Noffsinger, J. B.; Danielson, N. D., *Analytical chemistry* 2002, 59 (6), 865-868.
 53. Deaver, D. R., *Nature* 1995, 377, 758-760.
 54. Wei Z., Bard. A. J., *Analytical chemistry* 2007, 79, 459-463.
 55. Cao, J. T.; Wang, Y. L.; Zhang, J. J.; Dong, Y. X.; Liu, F. R.; Ren, S. W.; Liu, Y. M., *Analytical chemistry* 2018, 90 (17), 10334-10339.
 56. Sun, H.; Wang, H.; Bai, W.; Bao, L.; Lin, J.; Li, Y., *Talanta* 2019, 191, 350-356.
 57. Yanbing Zu, A. J. B., *Analytical chemistry* 2000, 72, 3223-3232.

-
58. Valenti, G.; Rampazzo, E.; Kesarkar, S.; Genovese, D.; Fiorani, A.; Zanut, A.; Palomba, F.; Marcaccio, M.; Paolucci, F.; Prodi, L., *Coordination Chemistry Reviews* 2018, 367, 65-81.
 59. Erin M. Gross Paolo Pastore, R. M. W., *Journal of Physical Chemistry B* 2001, 105, 8732-8738.
 60. Wujian Miao, J.-P. C., Allen J. Bard, *Journal of the American Chemical Society* 2002, 124, 14478-14485.
 61. White, H. S.; Bard, A. J., *Journal of the American Chemical Society* 1982, 104 (25), 6891-6895.
 62. Bolletta, F., *Inorganica chimica Acta*, 1982, 62, 207-213.
 63. Guobao Xu, S. D., *Analytica Chimica Acta* 2000, 412, 235-240.
 64. Yamashita, K.; Yamazaki-Nishida, S.; Harima, Y.; Segawa, A., *Analytical chemistry* 2002, 63 (9), 872-876.
 65. Mark M. Richter, A. J. B., *Analytical Chemistry* 1998, 70, 310-318.
 66. Tokel-Takvoryan, N. E.; Hemingway, R. E.; Bard, A. J., *Journal of the American Chemical Society* 1973, 95 (20), 6582-6589.
 67. Akins, D. L. B., R.L., *Chemical Physics Letters* 1974, 29, 428-435.
 68. Santa Cruz, T. D.; Akins, D. L.; Birke, R. L., *Journal of the American Chemical Society* 1976, 98 (7), 1677-1682.
 69. Ertem, M. Z.; Concepcion, J. J., *Oxygen Atom Transfer as an Alternative Pathway for Oxygen–Oxygen Bond Formation. Inorganic Chemistry* 2020, 59 (9), 5966-5974.
 70. Seidler, E. M.; Kimball, A. B., *Journal of the American Academy of Dermatology* 2010, 63 (1), 52-62.
 71. Antonello, S.; Musumeci, M.; D. M. Wayner, D.; Maran, F., *Journal of the American Chemical Society* 1997, 119, 9541-9549.
 72. Reviews, C. C., *Chemical Science* 1988, 84, 85-277.
 73. Andersson, A.-M.; Isovitsch, R.; Miranda, D.; Wadhwa, S.; Schmehl, R. H., *Chemical communications* 2000, (6), 505-506.
 74. Wei, H.; Wang, E., *Luminescence* 2011, 26 (2), 77-85.
 75. Lu, X.; Wang, H.; Du, J.; Huang, B.; Liu, D.; Liu, X.; Guo, H.; Xue, Z., *Analyst* 2012, 137 (6), 1416-1420.
 76. Hai-Juan, L.; Shuang, H.; Lian-Zhe, H.; Guo-Bao, X., *Chinese Journal of Analytical Chemistry* 2009, 37 (11), 1557-1565.
 77. Ege, D.; Becker, W. G.; Bard, A. J., *Analytical chemistry* 1984, 56 (13), 2413-2417.
 78. Won-Yong, L.; Nieman, T. A., *Journal of Chromatography A* 1994, 659 (1), 111-118.
 79. Richter, M. M.; Bard, A. J., *Analytical chemistry* 1996, 68 (15), 2641-2650.
 80. Armelao, L.; Quici, S.; Barigelletti, F.; Accorsi, G.; Bottaro, G.; Cavazzini, M.; Tondello, E., *Coordination Chemistry Reviews* 2010, 254 (5-6), 487-505.
 81. Fang, L.; Chen, S.; Fang, T.; Fang, J.; Lu, C.; Xu, Z., *Composites Science and Technology* 2017, 138, 106-116.
 82. Shahalizad, A.; D'Aléo, A.; Andraud, C.; Sazzad, M. H.; Kim, D.-H.; Tsuchiya, Y.; Ribierre, J.-C.; Nunzi, J.-M.; Adachi, C., *Organic Electronics* 2017, 44, 50-58.
 83. Hemingway, R. E.; Park, S.-M.; Bard, A. J., *Journal of the American Chemical Society* 1975, 97 (1), 200-201.
 84. Bian, L., *The Journal of Physical Chemistry A* 2003, 107 (51), 11517-11524.
 85. Yu, H. X.; Cui, H.; Guan, J. B., *Luminescence: The journal of biological and chemical luminescence* 2006, 21 (2), 81-89.

-
86. Fan, F.-R.; Mau, A.; Bard, A.-J., *Chemical physics letters* 1985, 116 (5), 400-404.
 87. Richter, M. M.; Fan, F.-R. F.; Klavetter, F.; Heeger, A. J.; Bard, A. J., *Chemical Physics Letters* 1994, 226 (1-2), 115-120.
 88. Zhang, C.; Zhou, G.; Zhang, Z.; Aizawa, M., *Analytica chimica acta* 1999, 394 (2-3), 165-170.
 89. Zielonka, J.; Lambeth, J. D.; Kalyanaraman, B., *Free Radical Biology and Medicine* 2013, 65, 1310-1314.
 90. Ramkiran, A.; Varun G. M.; Puranjan. M., Nagarajan P., *Chemistry of Advanced Materials* 2018, 3(1), 16-22.
 91. Tian, K.; Li, D.; Tang, T.; Nie, F.; Zhou, Y.; Du, J.; Zheng, J., *Talanta* 2018, 185, 446-452.
 92. Cheng, Y.; Yuan, R.; Chai, Y.; Niu, H.; Cao, Y.; Liu, H.; Bai, L.; Yuan, Y., *Analytica chimica acta* 2012, 745, 137-142.
 93. Marquette, C. A.; Ravaud, S.; Blum, L. J., *Analytical Letters* 2000, 33, 1779-1796.
 94. Su, Y.; Wang, J.; Chen, G., *Analytica chimica acta* 2005, 551 (1-2), 79-84.
 95. Dai, H.; Lin, Y.; Xu, G.; Gong, L.; Yang, C.; Ma, X.; Chen, G., *Electrochimica acta* 2012, 78, 508-514.
 96. Zhou, J.; Ma, G.; Chen, Y.; Fang, D.; Jiang, D.; Chen, H.-y., *Analytical chemistry* 2015, 87 (16), 8138-8143.
 97. Kong, D.; Huang, S.; Cheng, J.; Zhuang, Q.; Liu, Y.; Lu, C. H., *Luminescence* 2018, 33 (4), 698-703.
 98. Dong, Y.-P.; Cui, H.; Xu, Y., *Langmuir* 2007, 23 (2), 523-529.
 99. Kitte, S. A.; Gao, W.; Zholudov, Y. T.; Qi, L.; Nsabimana, A.; Liu, Z.; Xu, G., *Analytical chemistry* 2017, 89 (18), 9864-9869.
 100. Zhang, J.; Jin, R.; Chen, Y.; Fang, D.; Jiang, D., *Sensors and Actuators B: Chemical* 2021, 329, 129208.
 101. Ding, Z.; Quinn, B. M.; Haram, S. K.; Pell, L. E.; Korgel, B. A.; Bard, A. J., *Science* 2002, 296 (5571), 1293-1297.
 102. Myung, N.; Ding, Z.; Bard, A. J., *Nano Letters* 2002, 2 (11), 1315-1319.
 103. Ding, S.-N.; Xu, J.-J.; Chen, H.-Y., *Chemical communications* 2006, (34), 3631-3633.
 104. Bae, Y.; Myung, N.; Bard, A. J., *Nano Letters* 2004, 4 (6), 1153-1161.
 105. Shen, L.; Cui, X.; Qi, H.; Zhang, C., *The Journal of Physical Chemistry C* 2007, 111 (23), 8172-8175.
 106. Jie, G.; Liu, B.; Pan, H.; Zhu, J.-J.; Chen, H.-Y., *Analytical Chemistry* 2007, 79 (15), 5574-5581.
 107. Wang, Y.; Lu, J.; Tang, L.; Chang, H.; Li, J., *Analytical chemistry* 2009, 81 (23), 9710-9715.
 108. Cheng, C.; Huang, Y.; Wang, J.; Zheng, B.; Yuan, H.; Xiao, D., *Analytical chemistry* 2013, 85 (5), 2601-2605.
 109. Lim, C. S.; Hola, K.; Ambrosi, A.; Zboril, R.; Pumera, M., *Electrochemistry Communications* 2015, 52, 75-79.
 110. Chen, L.; Zeng, X.; Si, P.; Chen, Y.; Chi, Y.; Kim, D.-H.; Chen, G., *Analytical chemistry* 2014, 86 (9), 4188-4195.
 111. Luan, L.; Lin, Z.-j.; Wu, G.; Huang, X.-l.; Cai, Z.-m.; Chen, X., *Chemical Communications* 2011, 47 (13), 3963-3965.
 112. Pinaud, F.; Russo, L.; Pinet, S.; Gosse, I.; Ravaine, V. r.; Sojic, N., *Journal of the American Chemical Society* 2013, 135 (15), 5517-5520.
 113. Yin, M.; Wu, L.; Li, Z.; Ren, J.; Qu, X., *Nanoscale* 2012, 4 (2), 400-404.

-
114. Miao, W.; Bard, A. J., *Analytical chemistry* 2004, 76 (23), 7109-7113.
115. Chen, Y.; Xu, J.; Su, J.; Xiang, Y.; Yuan, R.; Chai, Y., *Analytical Chemistry* 2012, 84 (18), 7750-5.
116. Chen, Y.; Jiang, B.; Xiang, Y.; Chai, Y.; Yuan, R., *Chemical Communication* 2011, 47 (27), 7758-60.
117. Zhuo, Y.; Liao, N.; Chai, Y. Q.; Gui, G. F.; Zhao, M.; Han, J.; Xiang, Y.; Yuan, R., *Analytical Chemistry* 2014, 86 (2), 1053-60.
118. Xu, S.; Liu, Y.; Wang, T.; Li, J., *Analytical chemistry* 2011, 83 (10), 3817-3823.
119. Niu, H.; Yuan, R.; Chai, Y.; Mao, L.; Liu, H.; Cao, Y., *Biosensors and Bioelectronics* 2013, 39 (1), 296-299.
120. Niu, H.; Yuan, R.; Chai, Y.; Mao, L.; Yuan, Y.; Cao, Y.; Zhuo, Y., *Chemical Communications* 2011, 47 (29), 8397-8399.
121. Duan, R.; Zhou, X.; Xing, D., *Analytical chemistry* 2010, 82 (8), 3099-3103.



Chapter 2.

Photoinduced electrochemiluminescence at depleted semiconductor electrodes in water

2.1 Introduction

Basics in Semiconductors

An intrinsic semiconductor (SC), is a chemically pure (i.e., undoped) SC without dopant species. Intrinsic SCs present and possess poor conductivity. In an intrinsic SC, the density of charge carriers is only determined by thermal excitation following the mass law. The equation of Mass-Action Law: $np = n_i^2$. The product of the free electron concentration n and the free hole concentration p is equal to a constant square of intrinsic carrier concentration n_i . If somehow n is increased (e.g. by doping), p must decrease to keep np constant. In monocrystalline silicon (the archetypal SC), silicon atoms form a cubic diamond structure with the four peripheral electrons of the Si atom providing bonds with neighboring atoms. According to molecular bonding theory, the formation of bonding and antibonding levels is determined by the combination of atomic orbitals of several atoms. Closely located energy levels are usually referred to as energy bands, which comprise the valence band (VB, E_{VB} being the energy of the valence band edge, similar to the highest occupied molecular orbital, HOMO) and the conduction band (CB, E_{CB} being the energy of the conduction band edge, similar to the lowest unoccupied molecular orbital, LUMO). The energy gap between the two bands is called the band gap (E_g), it corresponds to the minimum energy required to excite electrons from their bound state to a free state where they can participate in conduction. In an intrinsic Si, the Fermi level (E_F) is in the middle of E_g . The Fermi level for intrinsic semiconductor is given as, $E_F = (E_{CB} + E_{VB})/2$. E_F is an important parameter because it is the electrochemical potential of the SC. SC doping is very useful to modulate the electrical, optical, and structural properties of SC. It consists of the intentional introduction of impurities into an intrinsic SC. After this process, the doped SC is referred to as an extrinsic SC, and can belong to two main groups, the group of n-type SCs (i.e., SCs doped with donor atoms) or the group of p-type SCs (i.e., SCs doped with acceptor atoms).

n-type Si has been doped with an element from group V as an impurity, such as phosphorus (P), arsenic (As), or antimony (Sb). In an n-type Si SC, the impurity has five valence electrons which is more than the valence electron of Si, one valence electron from the impurity becomes free to move and can participate in the conductivity through the conduction band. The electrons are the major carriers of the n-type SC, shown in Figure 2.1b. For an n-type SC, the probability of finding an electron in the conduction band is larger than the probability of finding a hole in the valence band, therefore, as a consequence of n-doping, E_F is shifted toward higher energy (closer to E_C).

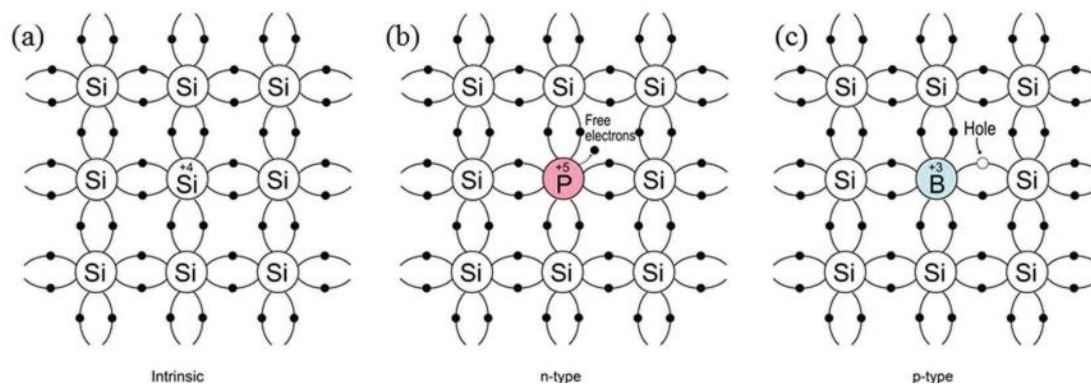


Figure 2.1 Schematic bond representation for (a) intrinsic silicon; (b) n-type silicon doped with phosphorus and (c) p-type silicon doped with boron.^{1,2}

p-type Si has been doped with an element from group III as an impurity (like boron (B), aluminium (Al), gallium (Ga), indium (In), etc.), shown in Figure 2.1c. These elements have three valence electrons, so the impurity added creates a vacancy of electron (i.e., an hole) in the valence band. The hole is the majority carrier of p-type SC and in a p-type SC, E_F is located closer to E_{VB} .

Description of the Semiconductor/Liquid Interface

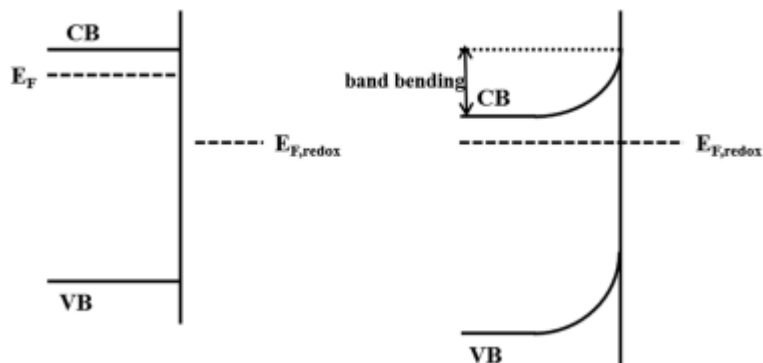


Figure 2.2 Equilibration of the Fermi levels results in the formation of a space charge region in the n-type semiconductor.

When a SC is immersed in a liquid containing a redox couple, charges will transfer between the two phases until the electronic equilibrium is established. At equilibrium, the Fermi levels of both phases are the same. Since the electrochemical potential of electrons is equivalent to the Fermi energy, it allows us to define a *redox Fermi energy* $E_{F,redox}$, which depends on the Nernst potential of redox couple in the solution, thus, the standard potential U° of the ox/red (O/R) couple and on the concentrations of its constituents (C_O and C_R). The number of electrons transferred in the redox reaction is n . Here is the

Nernst equation showing the equilibrium redox potential on the standard hydrogen scale(SHE).

$$U_{\text{redox}} = U^{\circ} + \frac{RT}{nF} \ln \frac{C_0}{C_R} \quad (2.1)$$

Taking the vacuum level as the zero energy, SHE appears to lie at -4.5 eV with respect to the vacuum level. $E_{F,\text{redox}}$ is given by

$$E_{F,\text{redox}} = -4.5 \text{ eV} - e_0 U_{\text{redox}} \quad (2.2)$$

As a result of this equilibration process, a built-in electric field is formed in the SC, which can help for charge separation and for directing photogenerated minority charge carriers (holes for n-type SC, electrons for p-type SC) into the solution.³ The band bending is determined by the difference between the original Fermi level of the SC and the Fermi level of the redox couple, shown on the left-hand side of Figure 2.2. The region formed by the transfer of charge is called the space charge layer or the depletion layer.

If the external potential is biased from equilibrium to more negative values, the band bending decreases, and electrons transfer occurs from the conduction band to the electrolyte, thus it involves the reduction of oxidized species and a flow of current. If the external potential is biased to more positive values, the Schottky barrier avoids the transfer of electrons from the electrolyte to the conduction band, leading to only a very small current flow related to the oxidation of reduced species by thermal excitation of electrons into the conduction band. In this condition, the junction behaves as a Schottky diode, which blocks current flow in one direction, as shown in the middle figure of Figure 2.4.

Three main regimes (Figure 2.3) are possible which can be described as “flat band regime”, “depletion regime” and “accumulation regime”.

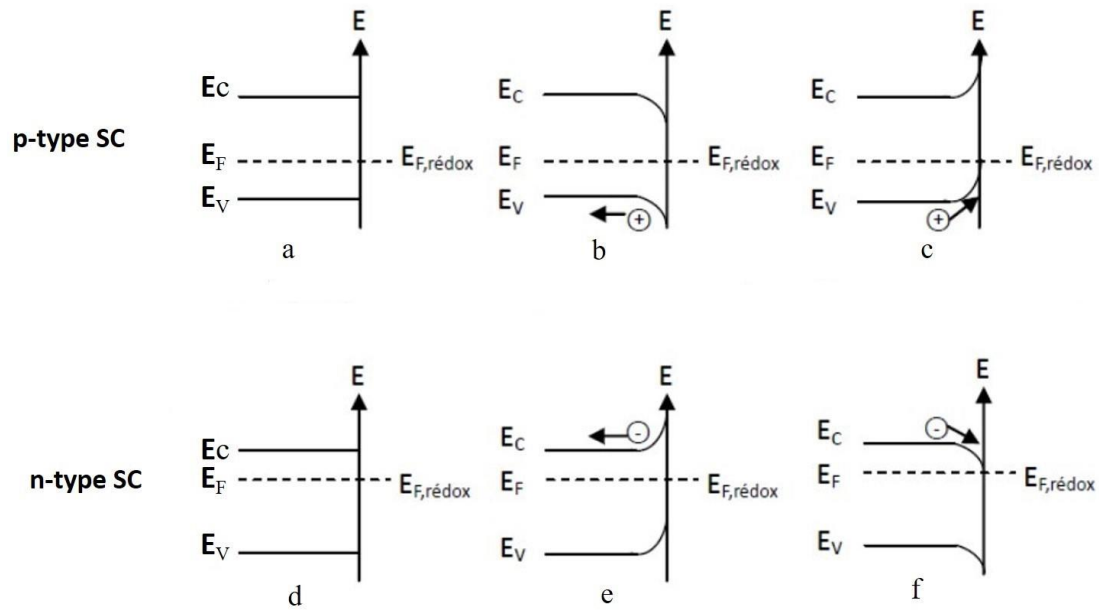


Figure 2.3 The three possible equilibria in the dark

Flat Band

A flat band regime is formed when the Fermi Level of SC (E_F) and the Fermi level of redox couples ($E_{F, \text{redox}}$) in the electrolyte are identical.

Depletion

In an n-type SC, if $E_{F, \text{Redox}} < E_F$, electrons move to the solution until equilibrium is reached. Since the Fermi levels in both phases must be the same, the energy bands in SC are bent upward at the equilibrium. The majority charge carriers (e^-) are depleted at the interface resulting in the formation of a depletion layer. Conversely, in a p-type SC, if $E_{F, \text{Redox}} > E_F$, the energy bands are bent downward and the band bending is also produced and the majority charge carriers, the holes (h^+), are depleted at the interface.

In this case, the majority carriers (the e^- for an n-type SC and the h^+ for a p-type SC) cannot flow from the SC to the electrolyte.

Accumulation

For an n-type SC, when $E_{F, \text{Redox}} > E_F$, the bands are curved downward and majority charge carriers (e^-) are enriched at the interface. Conversely, for a p-type SC, when $E_{F, \text{Redox}} < E_F$, the bands are curved upward and majority charge carriers (h^+) are enriched at the interface. In this case, the majority carriers can flow from the SC to the electrolyte.

Therefore, only the flat band situation (very unlikely to occur at equilibrium) and the accumulation situation allow the reaction to occur to the interface in the dark. In this last situation (Figure 2.3c and f),

in an n-type SC, the majority carriers e^- can therefore react with the species of the electrolyte to trigger a reduction reaction. Conversely, in a p-type SC, the h^+ can react with the species of the electrolyte to perform an oxidation reaction.

The Semiconductor–Electrolyte Junction Under Illumination

When the energy of illuminated photons is greater than E_g of SC, electrons are excited to the unoccupied states in the conduction band, leaving holes in the valence band. Electron-hole pairs are created within the SC. This light energy source, therefore, modifies the concentration of charge carriers at the SC/electrolyte interface. Here, we use an n-type SC in depletion under illumination as an example. In this condition, holes created by illumination in the valence band of n-type SC can oxidize the reduced redox species in the electrolyte, leading to an oxidation reaction: $R + h^+ = O$. Since the concentration of holes in the dark is much smaller than the concentration of electrons in n-type SC, the Schottky barrier prevents the oxidation process in the dark. Conversely, in the situation of a depleted p-type SC, photogenerated electrons in the conduction band under illumination can migrate to the surface to react with oxidized redox species from the electrolyte, leading to a reduction reaction.

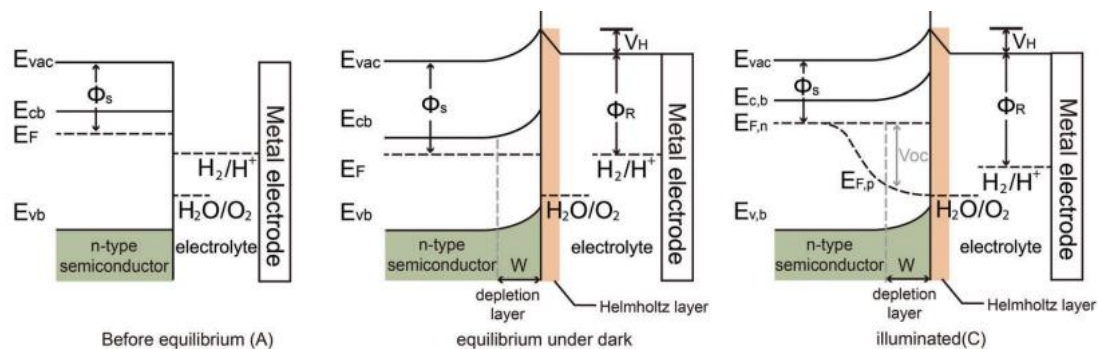


Figure 2.4 Band energetics of an n-type semiconductor/electrolyte contact showing the relationships between the electrolyte redox couple (H_2O/O_2 and H_2/H^+), the Helmholtz layer potential drop (V_H), and the semiconductor work function (Φ_s), the electrolyte work function (Φ_R), the electron quasi-Fermi level ($E_{F,n}$) and hole quasi-Fermi level ($E_{F,p}$) in three cases: (A) before equilibration between the two phases; (B) after equilibration under dark conditions; and (C) in quasi-static equilibrium under steady-state illumination. The voltage (V_{oc}) generated by the junction under illumination is given by the difference between the potential corresponding to $E_{F,n}$ and the electrochemical potential of the redox couple of interest (H_2O/O_2 for an n-type semiconductor and H_2/H^+ for a p-type).²

In depleted SCs, minority carriers are driven to the interface under illumination. Thus, illumination has a considerable effect on an interface in a depletion situation, however, due to the band bending direction, it will not have a consequence on the reactivity of an interface in the accumulation regime.

Under illumination (non-equilibrium conditions), the quasi-Fermi level is a descriptor of the

electrochemical potential of one carrier. In n-type SCs under illumination, $E_{F,n}$ is the electron quasi-Fermi level and $E_{F,p}$ is the hole quasi-Fermi level. The voltage generated by the built-in electric field within semiconductors is referred to as the open-circuit voltage (V_{oc}) or photovoltage, which is equal to the difference between $E_{F,n}$ and $E_{F,p}$ under no net current flow. V_{oc} is a key parameter for describing semiconductor photoanodes and photocathodes.

If we consider the complete electrochemical cell, in the case of an n-type SC photoanode, the photogenerated holes driven by the energy difference between the valence band edge and the redox level of the species in the solution move to the solution, the photoinduced electrons are collected and transferred through the external circuit to the counter electrode or move to the cathode to perform a reduction and ensure the electroneutrality of the system. The opposite phenomenon occurs on a p-type SC photocathode. This phenomenon, therefore, results in the flow of a photocurrent, corresponding to an electrochemical reaction induced by photogenerated charge carriers at the depleted SC/electrolyte interface, then the photoelectrochemical cell is illuminated.

Photo-induced Electrochemiluminescence (PECL)

Photo-induced electrochemiluminescence (PECL) is a new concept in which ECL is generated on depleted semiconductor electrodes under illumination. The electrochemical and photoexcitation energies are coupled to produce sufficient energy for emitting light. PECL combines ECL and photoelectrochemistry of SCs. This concept relies on employing photogenerated minority carriers within a depleted semiconductor which can decrease the potential required to trigger an electrochemical reaction,^{4,5} involving the conversion of an input light signal (photons absorbed by the SC, λ_{exc}) to an output light signal (photons emitted by ECL process, λ_{emi}).

ECL on p-type silicon electrodes by a photosensitized reduction process in acetonitrile solution was firstly reported in 1975.⁶ It described the illuminated electrode to perform photosensitized electron transfer processes at lower electrode potentials (i.e., less positive for oxidations and less negative for reductions) than metal electrode. For PECL, the active portion of the electrode is that of the exciting light beam instead of the emission occurring over the entire metal electrode surface. ECL from photosensitized oxidations and reductions on p and n-type GaAs and InP electrodes of aromatic species in aprotic solvents were further investigated by Luttmer and Bard.⁷ The initial study was done in the dark, where no current flows, until the SC is illuminated with light having an energy higher than the bandgap of the electrode,

giving emission at potentials less positive than those required for emission on a metal electrode. Thus, the SC/liquid interface behaves like a Schottky junction and shows diode-like behavior under dark conditions. Therefore, it can be concluded that when the ECL reaction is carried out on an SC electrode, three new features can emerge. One feature is that no current flows under dark, another feature is that the electrochemical oxidations occurred on irradiated n-type SC at less positive potential, the last feature is ECL generated on irradiated n-type SC at less positive potential. The same feature occurs on p-type SC under dark, as electrochemical reductions occurred on irradiated p-type SC at a less negative potential than on an inert electrode. Specifically, the “negative overpotential” effect on n-type SC is the basis for light energy conversion utilizing electrochemical systems (caused by the V_{oc} , as seen in the previous section).

In this chapter, I will now report the PECL on n-Si/SiO_x/Ni photoanode in an aqueous solution with the model system [Ru(bpy)₃]²⁺/TPPrA⁸ and PECL on BiVO₄ photoanode with L-012 in NaOH.⁹ PECL of n-Si/SiO_x/Ni photoanode is an upconversion process, where 810 nm light absorption induces ECL emission in the visible (635 nm). Intense PECL emission can be obtained at a potential as low as 0.45 V vs SCE. Bright PECL emission is also observed on BiVO₄ at an even lower potential -0.4 V vs Ag/AgCl, amplifying the overall luminescence. This work constitutes the first example of PECL where $\lambda_{exc} < \lambda_{emi}$ and this PECL concept can be extended to other SCs and could find potential applications for light-addressable and imaging devices. This project is a collaboration with the group of Gabriel Loget from Institut des Sciences Chimiques de Rennes, University of Rennes.

2.2 PECL by Upconversion at Silicon Electrodes in Water

Silicon, the second most abundant element in the Earth’s crust, is attracting particular attention as a photoelectrode material because of its abundance, low toxicity, and tunable electronic properties.¹⁰ Silicon SC has a narrow band gap ($E_g \sim 1.1$ eV), which is relatively well matched to the solar spectrum. It becomes a promising material for photoelectrodes because a large number of photons can be absorbed and converted compared to other wider band gap SCs. Furthermore, highly controllable structures of Si can be produced with mature technological infrastructure. Thus, after the report from Candea et al. on photoelectrolysis of water,¹¹ Si has become one of the most studied materials in the early evolution of the photoelectrochemistry field using SC as the electrode. Besides, Si is also employed as a substrate to manufacture a broad diversity of microfluidic systems,¹² including diagnosis microchips,^{13, 14} which

makes it a relevant candidate as an ECL electrode. However, this material is generally highly unstable when used as a photoanode in water.¹⁵ To solve this problem, a Ni layer was designed to be a protection layer.¹⁶ The choice of Ni was driven by reports in the field of photoelectrochemical water electrolysis. Indeed, it was shown by Kenney et al.¹⁶ that nm-thick Ni layers can considerably stabilize Si electrodes for electrochemical reactions occurring in conditions particularly harsh for Si. Then, it has been shown in different reports that with Ni protection, Si photoanodes exhibited dynamic photoelectrochemical response with a low onset potential, high photocurrent density, and durability.^{17 18, 19} In these systems, it is thought that the low onset potential is caused by the increased junction photovoltage, induced by the oxidation of Ni.^{20, 21} In our study, direct current (DC) magnetron sputtering was used to obtain deposited Si/SiO_x/Ni(#nm) electrode with different thickness of Ni layer (# denotes the thickness of the Ni layer). The SiO_x tunnel layer had in all case, a thickness comprised between 1.5 to 2 nm, as determined previously by ellipsometry and transmission electron microscopy (TEM).^{19, 22}

2.2.1 Principle of P-ECL on a Silicon Anode

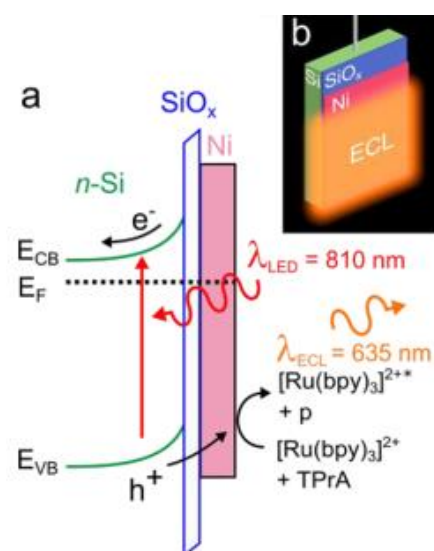


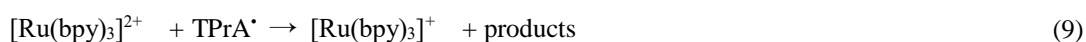
Figure 2.5 (a) Scheme showing an n-Si/SiO_x/Ni MIS photoanode during PECL (the side product of the TPrA radicals formed during the ECL process is denoted by p). (b) Scheme showing the Si/SiO_x/Ni electrodes employed in this work with ECL emission (λ_{ECL}).

Figure 2.5a shows the overall PECL scheme that involves the coupling of the input light energy having a wavelength of 810 nm and the electrical energy to produce an output emission with higher energy (wavelength of 635 nm). The combination of Si photoelectrochemistry and [Ru(bpy)₃]²⁺/TPrA ECL

creates a PECL system producing light from photogenerated h^+ . The light was obtained from n -Si/SiO_x/Ni electrode surface, due to the appearance of the excited state $[\text{Ru}(\text{bpy})_3]^{2+*}$, produced by the reaction between $[\text{Ru}(\text{bpy})_3]^{2+}$ and TPrA. This system emits light at 635 nm (Figure 2.5b), a wavelength that is shorter than its input light at 810 nm. This is reminiscent of up-conversion and allows triggering $[\text{Ru}(\text{bpy})_3]^{2+}$ /TPrA ECL at a low potential of 0.45 V vs SCE. The proposed mechanism of the reaction that occurred at the interface can be explained as follow.



Or



2.2.2 Characterization of the Si-based anodes

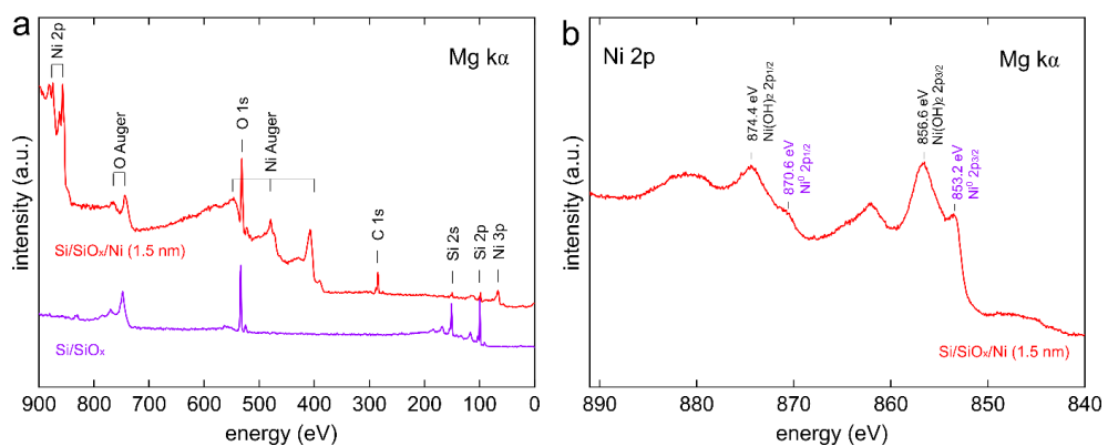


Figure 2.6 a) XPS survey spectra recorded for n -Si/SiO_x (purple curve) and n -Si/SiO_x/Ni (1.5 nm). b)

XPS spectrum showing the Ni 2p region for *n*-Si/SiO_x/Ni (1.5 nm).

From the X-ray photoelectron spectroscopy (XPS) spectra, the large decrease in the intensity of the Si 2p and 2s peaks after deposition shows that the Ni layer densely covered Si/SiO_x. Figure 2.6 b shows that the deposited Ni has characteristic features of a Ni⁰ metal film covered by a native oxide/hydroxide native layer.²³ In this figure, the peak positions attributed to Ni⁰ are displayed in purple and the peak positions attributed to Ni(OH)₂ are displayed in black; note that the NiO 2p_{3/2} component (~854 eV) is located between these two peaks. Thus, Ni was covered by a native NiO/Ni(OH)₂ layer in all cases, as confirmed XPS.

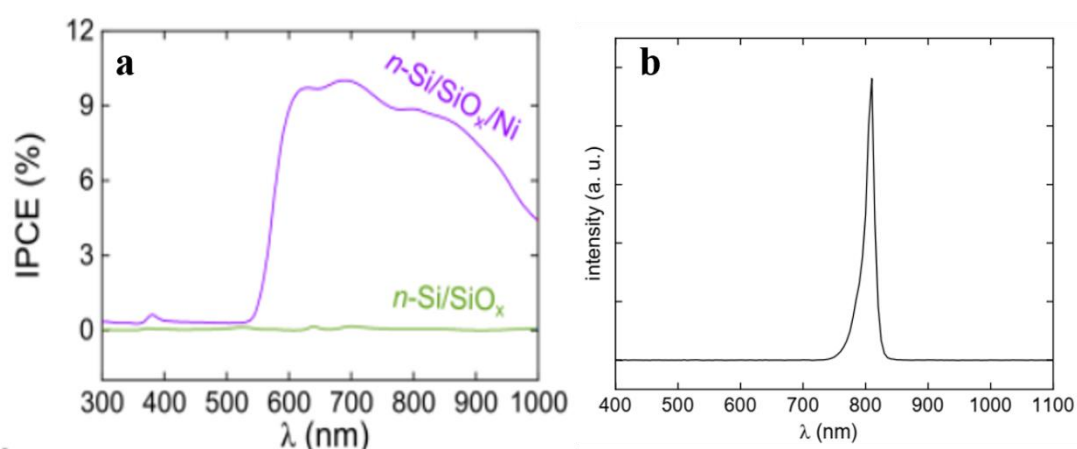


Figure 2.7 a) IPCE spectra recorded on *n*-Si/SiO_x (green curve) and *n*-Si/SiO_x/Ni (1.5 nm) (purple curve) at 0.7 V vs SCE. The measurement was performed in PBS (pH 7.3) with 5 mM [Ru(bpy)₃]²⁺ and 100 mM TPrA. b) Spectrum of the LED employed for P-ECL experiments.

The incident photon-to-current efficiency (IPCE) spectrum was recorded on *n*-Si/SiO_x/Ni. An effective photoconversion appears at wavelength >550 nm, with the maximum conversion efficiency of ~10% around 700 nm. The cutoff below 550 nm is explained by the absorption of [Ru(bpy)₃]²⁺ dissolved in the electrolyte, as confirmed by the absorption spectrum of the electrolyte (black curve in Figure 2.10). The IPCE spectrum recorded on *n*-Si/SiO_x under the same conditions (Figure 2.7a, green curve) presents no photoconversion, which is indicative of Si passivation in the timeframe of the IPCE measurement. This experiment confirms the importance of the Ni thin film for promoting stable charge transfer at the solid-liquid interface. To record real-time ECL on illuminated *n*-Si/SiO_x/Ni surfaces, an incident wavelength of 810 nm was employed (the light-emitting diode (LED) spectrum is shown in Figure 2.7b), which corresponds to a reasonable 9% IPCE (Figure 2.7a) and is far enough from the ECL emission peak ($\lambda_{\text{ECL}} = 635$ nm, Figure 2.10).

2.2.3 Electrochemistry and PECL of Si/SiO_x/Ni

Electrochemistry and ECL of p⁺-Si/SiO_x/Ni

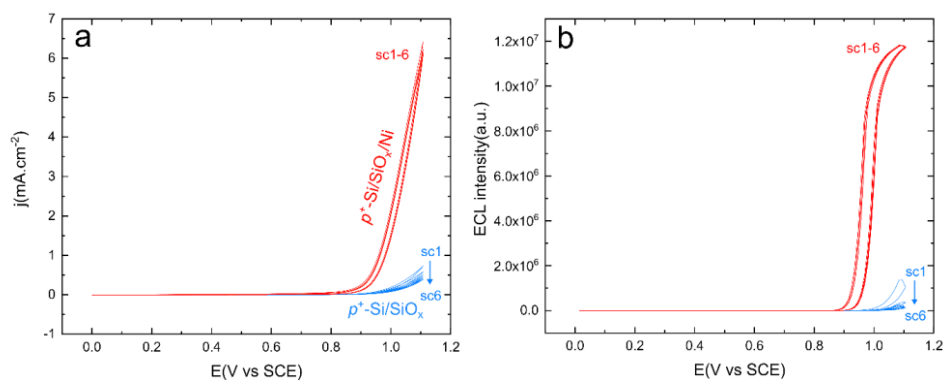


Figure 2.8 a) CVs (6 consecutive scans) recorded in the dark on p⁺-Si/SiO_x/Ni (5 nm) (red curves) and p⁺-Si/SiO_x (blue curves). b) Corresponding ECL intensity vs E curves. These measurements were performed in PBS (pH 7.3) with 5 mM [Ru(bpy)₃]²⁺ and 100 mM TPrA at 20 mV s⁻¹.

To evaluate the electrochemical performance and the stability of our metal-insulator-SC (MIS) junctions, the first experiments were performed on non-photoactive model electrodes that were prepared with degenerated p⁺-Si surfaces modified with a 5 nm-thick Ni thin film to yield non-photoactive p⁺-Si/SiO_x/Ni (5 nm) and non-photoactive p⁺-Si/SiO_x. Dark electrochemical analyses of these electrodes in the ECL electrolyte (pH 7.3) revealed that ECL could occur on such surfaces at high potentials, as shown by cyclic voltammetry (CV) (Figure 2.8). Current and corresponding ECL signals are still stable on p⁺-Si/SiO_x/Ni (5 nm) electrode after 6 consecutive scans, but on p⁺-Si/SiO_x, current and corresponding ECL signals has passivation. This measurement shows clearly that the non-photoactivity of p⁺-Si/SiO_x(Ni) and the effect of Ni layer for stabilizing silicon electrode surface.

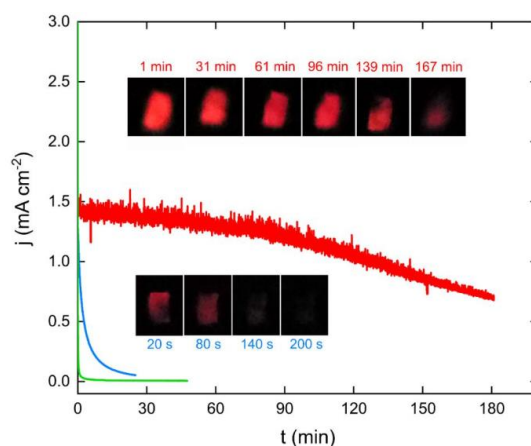


Figure 2.9 CAs recorded at 1 V in the dark on p⁺-Si/SiO_x/Ni(5 nm) (red curve), at 1.2 V on p⁺-Si/SiO_x (blue curve), and at freshly-hydrogenated Si(Si-H) (green curve). Inset: Optical photographs showing the ECL emission observed on p⁺-Si/SiO_x/Ni(5 nm) (top) and p⁺-Si/SiO_x (bottom). These measurements were performed in PBS (pH 7.3) with 5 mM [Ru(bpy)₃]²⁺ and 100 mM TPrA.

Chronoamperometry (CA) was also recorded on p⁺-Si/SiO_x/Ni (5 nm) and p⁺-Si/SiO_x in the dark. In this case, current densities (*j*) in the range of 1 mA cm⁻² were recorded at 1 V vs SCE, associated with ECL that could be observed by the naked eye on p⁺-Si/SiO_x/Ni (5 nm) and recorded with a digital camera for more than 2 h (Figure 2.9). This is in strong contrast to the behavior observed on Ni-free hydrogenated Si (Si-H) and Si/SiO_x electrodes, which exhibited a quick decay of *j* and the ECL, which disappeared after a few minutes (Figures 2.8 and 2.9). Thus, these experiments demonstrate the importance of the Ni layer for stabilizing the anode and show that stable ECL can occur at Si/SiO_x/Ni MIS electrodes, allowing the study of photoactive n-Si/SiO_x/Ni electrodes, which is described in the following.

Electrochemistry and PECL of n-Si/SiO_x/Ni

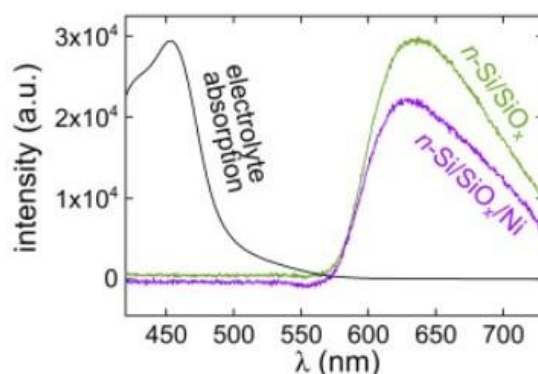
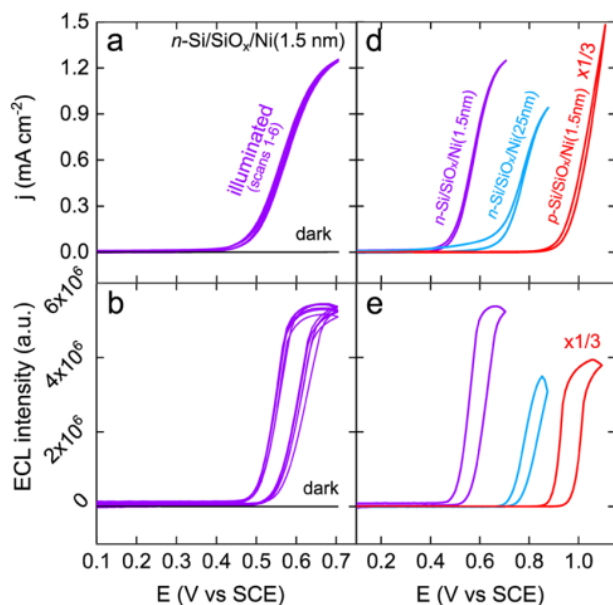


Figure 2.10 Normalized absorption spectrum of the electrolyte (black curve) and PECL emission spectra recorded on n-Si/SiO_x (green curve) and n-Si/SiO_x/Ni (1.5 nm) (purple curve) at 0.6 V vs SCE under illumination at $\lambda_{LED} = 810$ nm.

I will now discuss the behavior of photoactive Si anodes, that were made by employing a moderately doped n-type Si (n-Si) surface, these electrodes were studied in the same media as before: PBS (pH 7.3) with 5 mM [Ru(bpy)₃]²⁺ and 100 mM TPrA. When a potential of 0.6 V vs. SCE was applied with an LED illumination of 810 nm on n-Si/SiO_x and n-Si/SiO_x/Ni (1.5 nm), an ECL emission peak can be detected at 635 nm (green and purple curves of Figure 2.10), which is identical to the spectra recorded on classic glassy carbon electrode. This result indicates that the same metal-to-ligand charge transfer excited state, [Ru(bpy)₃]^{2+*}, was reached on the different electrode surfaces. This figure also features the electrolyte

absorption which shows a peak at almost 465 nm.

To study the photoelectrochemistry and PECL on n-Si/SiO_x/Ni (1.5 nm), the CV and the corresponding ECL intensity, respectively, were recorded on n-Si/SiO_x/Ni (1.5 nm). It is interesting to note the absence of current and ECL signals in the dark (black curve), showing the rectifying behavior of the solid/liquid junction in that potential range. In contrast, when the electrode was illuminated, a photocurrent density in the range of 1 mA cm⁻² coupled with ECL signals appeared at potentials above 0.45 V (purple curves in Figure 2.11 a,b) with no decay during six consecutive cycles. The stability of n-Si/SiO_x/Ni (1.5 nm) was further confirmed by chronopotentiometry (CP) under illumination, where a constant current density of 1 mA cm⁻² was applied for 15 min, during which only negligible potential and ECL variations were recorded (Figure 2.11c, purple plots). Here, n-Si/SiO_x is used as a comparison. The curve of n-Si/SiO_x shows that its potential increases largely in a short time, which means that photocorrosion occurs on n-Si/SiO_x with poor stability. The fast deactivation during CP measurement on n-Si/SiO_x further confirms the importance of Ni layer. A comparison of the photocurrent and ECL intensity versus E curves obtained on illuminated photoactive n-Si/SiO_x/Ni (1.5 nm) with the ones recorded on non-photoactive p⁺-Si/SiO_x/Ni (1.5 nm) is shown in Figure 2.11d and e. The figures reveal that the onset potential for ECL emission at non-photoactive p⁺-Si/SiO_x/Ni (1.5 nm) is much larger than that recorded at n-Si/SiO_x/Ni (1.5 nm).



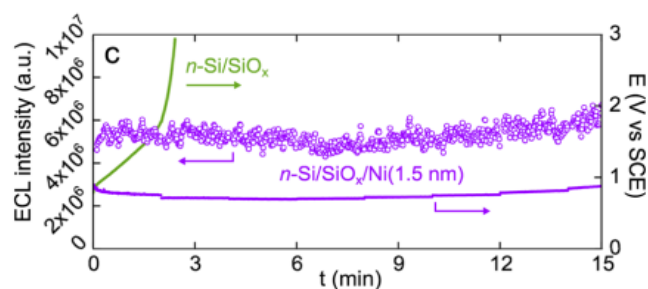


Figure 2.11 (a) CVs recorded on n-Si/SiO_x/Ni (1.5 nm) under LED illumination at 810 nm (six consecutive scans, purple curves) and in the dark (black curve). (b) Corresponding ECL intensity vs E curves. (c) CP curves (lines) recorded at 1 mA cm⁻² on n-Si/SiO_x/Ni (1.5nm) (purple curve) and n-Si/SiO_x (green curve) under illumination at 810 nm. The ECL intensity evolution on n-Si/SiO_x/Ni (1.5 nm) is shown by purple circles. (d) CVs recorded in the dark on p⁺-Si/SiO_x/Ni (1.5 nm) (red curve) and under illumination on n-Si/SiO_x/Ni (1.5nm) (purple curve) and n-Si/SiO_x/Ni (25 nm) (blue curve). (e) Corresponding ECL intensity vs E curves. These measurements were performed in PBS (pH 7.3) with 5 mM [Ru(bpy)₃]²⁺ and 100 mM TPrA at 20 mV s⁻¹. The red curves in (d) and (e) have been divided by 3 for clarity.

The effect of the Ni layer by employing an n-Si/SiO_x/Ni (25 nm) electrode was further investigated. This electrode was also active for PECL but the thicker Ni film is associated with a considerable decrease in photovoltage ($V_{oc} = 150$ mV), in good agreement with recent reports showing that ultrathin metal films on n-Si-based Schottky junction photoelectrodes considerably increase the junction barrier height.^{16, 19,}

24

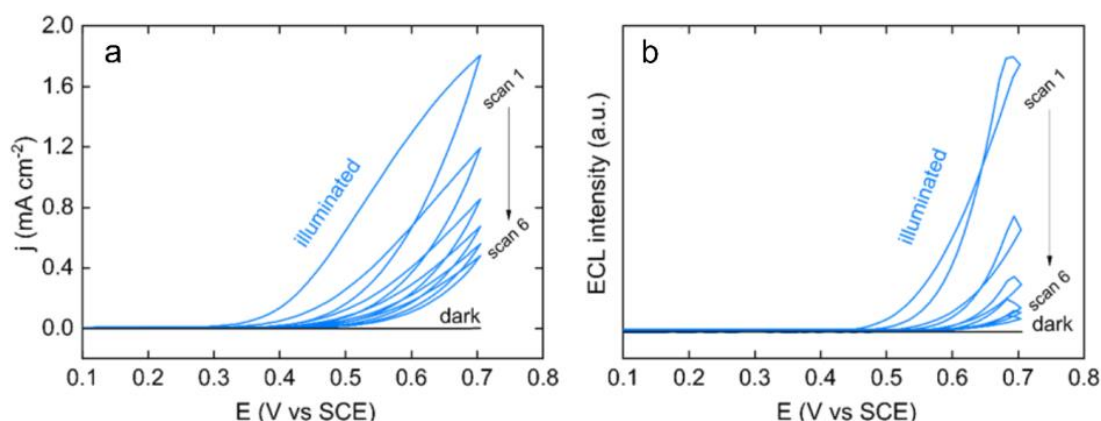


Figure 2.12 a) CVs recorded at 20 mV s⁻¹ on n-Si/SiO_x under illumination (6 consecutive scans, blue curves) and in the dark (black curve). b) Corresponding ECL intensity vs E curves.

CVs and corresponding ECL spectra were also performed on n-Si/SiO_x under illumination with consecutive 6 scans. In contrast to the previously discussed case where a Ni thin film is used, n-Si/SiO_x exhibited fast deactivation during CV cycling, shown by the decay of the corresponding ECL signal

(Figure 2.12). This is in good agreement with the sharp increase of potential on n-Si/SiO_x shown in CP measurements (Figure 2.11c, green curve). These results all confirm that Ni layer provides a degree of protection. The effect of the illumination power on the PECL was finally investigated, as shown in Figure 2.13. Under dark, there is no photocurrent and corresponding ECL signal (black curve in (a) and (b)). In these experiments, CVs and corresponding ECL intensity profiles were recorded at different values of the illumination power (by controlling the current provided by the power generator connected to the LED). Photocurrent and ECL intensity was recorded under LED illumination with 5 powers, 2 mW cm⁻², 5.9 mW cm⁻², 9.7 mW cm⁻², 13.5 mW cm⁻², 17.3 mW cm⁻². The photocurrent and ECL signal is smallest when 2 mW cm⁻² power is used on the LED. When the illumination power increase, photocurrent, and the corresponding ECL also increase, and at 17.3 mW cm⁻², the largest photocurrent and strongest ECL light was obtained.

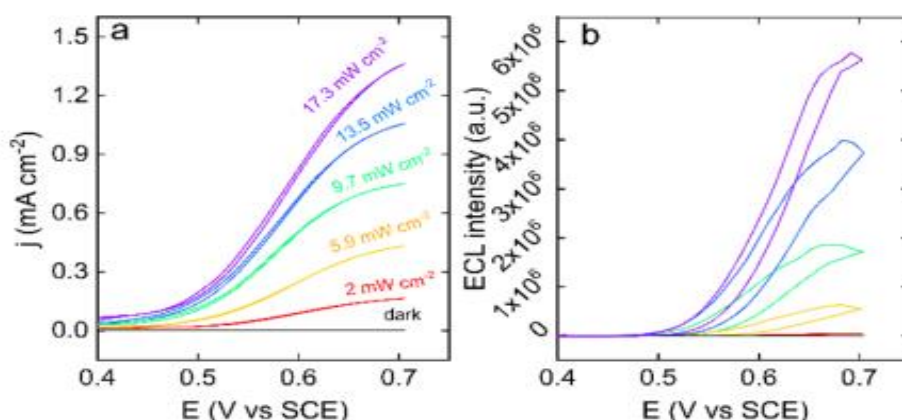


Figure 2.13 (a) CVs recorded on n-Si/SiO_x/Ni (1.5 nm) at different LED power densities. (b) Corresponding ECL intensity vs E curves. These measurements were performed in PBS solution (pH 7.3) containing 5 mM [Ru(bpy)₃]²⁺ and 100 mM TPrA with 810 nm incident light at a scan rate of 20 mV s⁻¹.

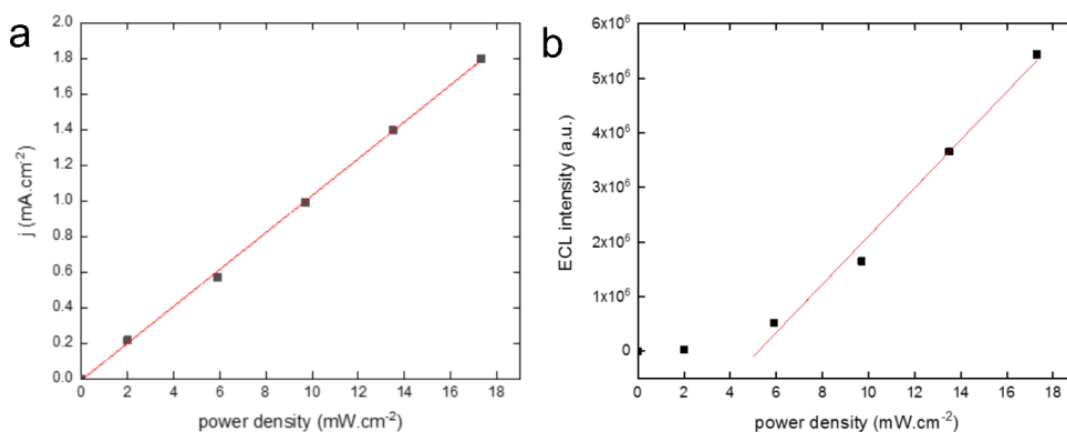


Figure 2.14 Curves show a) the evolution of the photocurrent density and b) the ECL intensity as a function of the illumination power density.

The results from Figure 2.14 further show the relationship between photocurrent, ECL signal, and the illumination power. It has a linear relationship between photocurrent and illumination power. Figures 2.13 and 2.14 all confirm that photocurrent and ECL are dependent on the illumination power.

2.3 Luminescence Amplification at BiVO₄ Photoanodes by PECL

Among n-SCs, BiVO₄ has been extensively studied and has emerged as a promising photoanode because of its favorable electronic and optical properties, its stability in neutral electrolytes,²⁵ its nontoxicity.²⁶ It has a bandgap of 2.4–2.5 eV and can absorb a significant portion of UV and visible light. BiVO₄ with the monoclinic scheelite phase shows the most photoactive activity, compared to tetragonal zircon-type and tetragonal scheelite structures.²⁷ Monoclinic scheelite BiVO₄ has a strong yellow color and potentials corresponding to its E_{CB} of ~ 0 V vs. the reversible hydrogen electrode (RHE) and to its E_{VB} of 2.4 V vs. RHE, providing sufficient overpotential for holes to photooxidize water.²⁸ The effective masses of electrons and holes in BiVO₄ are predicted to be much lighter than those of other semiconductors (e.g. TiO₂, In₂O₃). In my work, the BiVO₄ layer deposited on fluoride-doped SnO₂ (FTO) substrates was used as electrode. The deposition method consists in electroplating Bi⁰ onto FTO and converting it into BiVO₄ by an annealing procedure (see experimental section 1.2.2).

2.3.1 Principle of PECL on BiVO₄

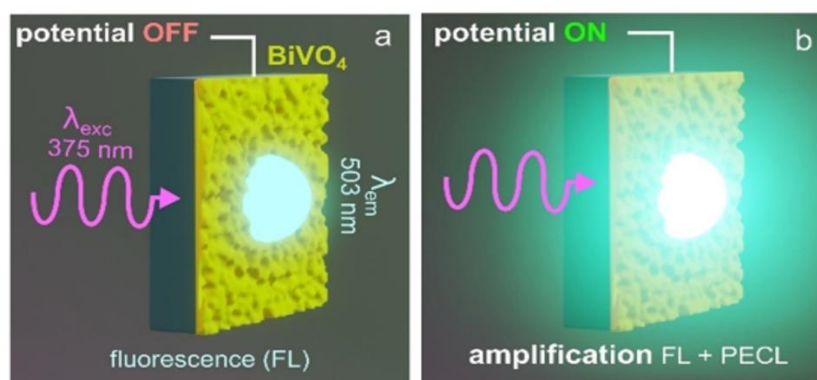


Figure 2.15 a,b) Schemes illustrating the luminescence amplification principle. In (a) Fluorescence of Luminol-012 (FL) is generated at a BiVO₄/liquid interface when a backside 375 nm illumination is applied. In (b) the luminescence is amplified by imposing a potential to the surface which triggers PECL.

Here, I will show that anodic PECL of this system can be induced at a low potential to amplify the overall

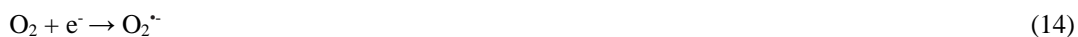
luminescence (i.e. Fluorescence of Luminol-012(FL)+PECL) in a precise manner. In the present configuration, FL of electrolyte is generated under incident light without applied potential and PECL enhances the luminescence signal when a potential is applied. The concept presented here is based on the use of λ_{exc} , which can photoexcite both the SC and the luminophore. As shown in Figure 2.15 a, when no electrochemical potential is applied to the surface (i.e. in open circuit condition), only FL is emitted at the liquid/solid interface, provided that the incident light is transmitted through the BiVO₄ surface. However, as depicted in Figure 2.15 b, when a potential is applied, PECL can be generated on the photoanode, which amplifies the intensity of the light emission. Before this work, PECL examples have been reported for designing electrochemically assisted up-conversion systems at Si electrode in water with the co-reactant system [Ru(bpy)₃]²⁺/TPrA⁸ and other SC photoelectrodes using organic luminophores dissolved in dried organic electrolytes were studied.^{6,7} In the previous section of my thesis, PECL allowed light production at a potential of 0.45 V vs. SCE, all potentials of these electrodes in this study were much lower than the typical potential (>1 V vs. same reference electrode) required on the conventional electrode with [Ru(bpy)₃]²⁺/TPrA system. In this work, the potential for PECL on BiVO₄ photoanode using a luminol analogue (L-012: 8-amino-5-chloro-2,3-dihydro-7-phenyl-pyrido[3,4-d]pyri-dazine-1,4-dione)^{29, 30} is much lower, at -0.4 V vs. Ag/AgCl. A fundamental difference between this system and the former PECL study is that, in the first one, FL was avoided by using an incident wavelength, λ_{exc} , higher than the absorption band ($\lambda_{exc} > \lambda_{abs}$) of the ECL emitter. The PECL and fluorescence of L-012 emit at 503 nm with the incident light at 375 nm.

Hydrogen peroxide (H₂O₂) is often used as an additive to increase anodic luminol ECL, because anodic luminol ECL is generally weak due to the difficult oxidation of water to generate reactive oxygen species.³¹ In the present study, L-012 was selected because it has been proved that it can produce stronger luminescence than luminol.³² Surprisingly, the L-012 ECL is still intense without the addition of H₂O₂. The reaction mechanism for the luminol–H₂O₂ ECL system was already explained in the first chapter, but the reaction mechanism without H₂O₂ is not clear yet. In a previous study, the illumination of a glassy carbon electrode with a wavelength greater than 500 nm increased the ECL of luminol.³³ It has been proposed that hot carriers (electrons and holes) are responsible for the photocurrent generation on carbon-fiber or graphite electrode.^{34,35} According to the authors, hot holes can be induced at the electrode surface by light irradiation and the hot holes can oxidize hydroxide anions (OH⁻) to hydroxyl radicals (OH[•]), which is capable of promoting the oxidation of luminol, generating larger current and stronger ECL. Here

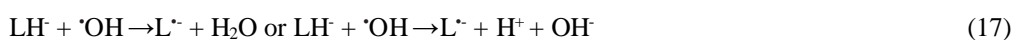
we speculate the possible L-012 ECL mechanism is that photogenerated holes oxidize OH⁻ to [•]OH, which is a sufficiently strong one-electron oxidant,³⁶ then promote the oxidation of L-012. Generally, L-012 exhibits a strong CL in alkaline solution.³⁷ Diazaquinone is termed as L.



The photogenerated electron flow to the external circuit, move to the counter electrode, and inject into an aqueous solution. Due to the presence of oxygen in the solution, the oxygen reduction occurred at the counter electrode, inducing the generation of superoxide radical O₂^{•-} and H₂O₂.³⁸



So with [•]OH, the CL pathway can be started by one-electron oxidation followed by rapid deprotonation of the formed LH[•] radical.^{39, 40}



L[•] radicals can either disproportionate to yield LH[•] and diazaquinone (L) or be oxidized a second time by a one-electron oxidant to yield L,



And in the presence of O₂^{•-} or H₂O₂ generated before, an endoperoxide species, LO₂²⁻ or LO₂H₂, is produced, from the reaction of L[•] with O₂^{•-} or the reaction between L with H₂O₂.



After this, LO₂²⁻ or LO₂H₂ eliminates molecular nitrogen or LO₂H,⁴¹ generating excited 3-aminophthalate dianion (AP²⁻*), which return to 3-aminophthalate dianion with light emission.



In this present system, (i) reaction sequence 12 and 16 rapidly supplies the hydroxyl radical $\cdot\text{OH}$ necessary for the first common step for all CL routes (17 and 18) and for reaction 20 to produce diazaquinone L, (ii) reaction 14 supplies a superoxide radical $\text{O}_2^{\cdot-}$ for reaction 15, and (iii) reaction 15 supplies hydrogen peroxide H_2O_2 for reaction 16. On this basis, L-012 ECL is formed by CL pathways and $\cdot\text{OH}$ would be required to trigger two pathways.

2.3.2 Characterization of BiVO_4 electrode

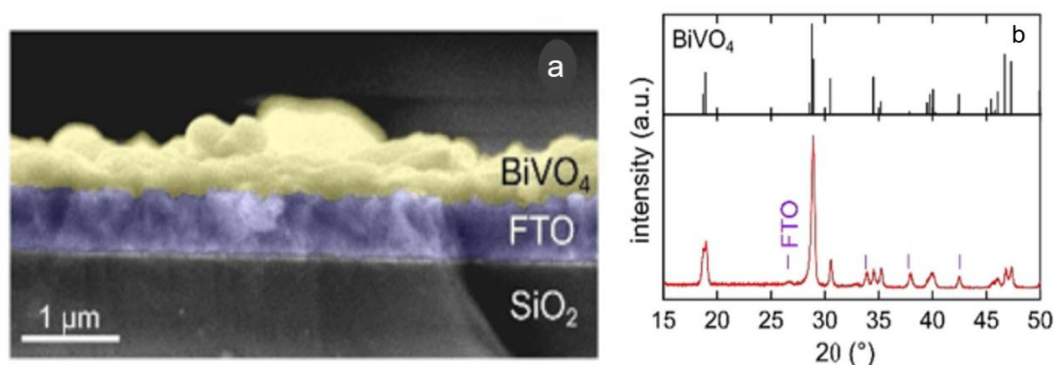


Figure 2.16 a) Colored SEM cross-section showing the FTO/ BiVO_4 surface used as a photoanode in this work (scale bar: $1\ \mu\text{m}$). b) XRD pattern of an FTO/ BiVO_4 surface (red curve). The top black lines indicate the predicted peak position for BiVO_4 (ICSD #100604) and the peaks corresponding to FTO (ICSD #39178) are indicated by purple lines.

Scanning electron microscopy (SEM), presented in Figure 2.16 a, showed that the BiVO_4 was deposited on the FTO surface and the thickness of the BiVO_4 layer was about $0.6\ \mu\text{m}$. The crystallinity of the layer was investigated by X-ray diffraction (XRD) measurements, which unveiled the pattern expected for monoclinic BiVO_4 (red and black curves of Figure 2.16b). It has been proved that the monoclinic BiVO_4 shows the most efficient photoactivity compared to the other two phases.⁴²

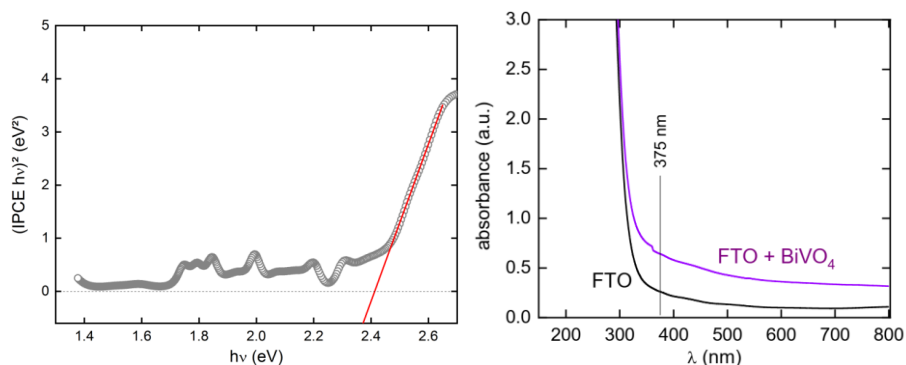


Figure 2.17 a) Tauc plot obtained by photocurrent spectroscopy using the BiVO₄ photoanode in the ECL electrolyte. b) UV-vis absorbance spectra of FTO (black curve) and FTO/BiVO₄ photoanodes (purple curve).

Photocurrent spectroscopy revealed that the BiVO₄ layer has an indirect bandgap⁴³ of 2.4 eV (see Figure 2.17a), in good agreement with the expected theoretical value.⁴⁴ UV-vis measurements showed the partial transparency of the SiO₂/FTO/BiVO₄ surface in the 350–400 nm range (see Figure 2.17b), as required to transmit λ_{exc} to the solution phase (red spectrum in Figure 2.18), this is the reason why we chose 375 nm as the incident light.

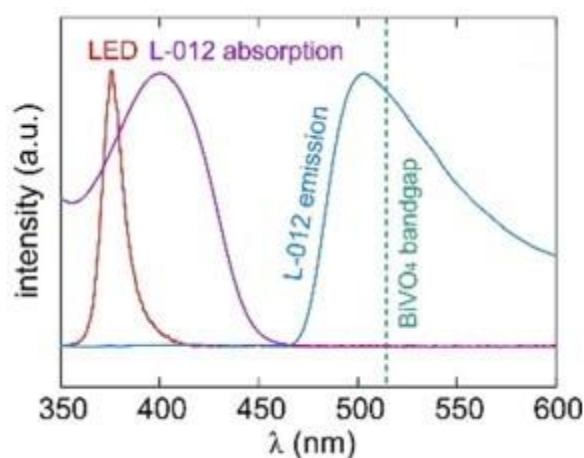


Figure 2.18 Normalized spectra showing the emission of the LED used in this work (red), L-012 absorption (purple), and the emission of L-012 (blue).

The LED light emits at 375 nm. The absorption and emission spectrum of L-012 were recorded in 0.1 M NaOH with an L-012 concentration of 10 mM. Figure 2.18 shows that L-012 absorbs at almost 410 nm and fluoresces with a maximum intensity at λ_{em} = 503 nm (blue spectrum). The experimentally determined bandgap of BiVO₄ is represented by the green dotted line.

2.3.3 Electrochemistry and PECL on BiVO₄

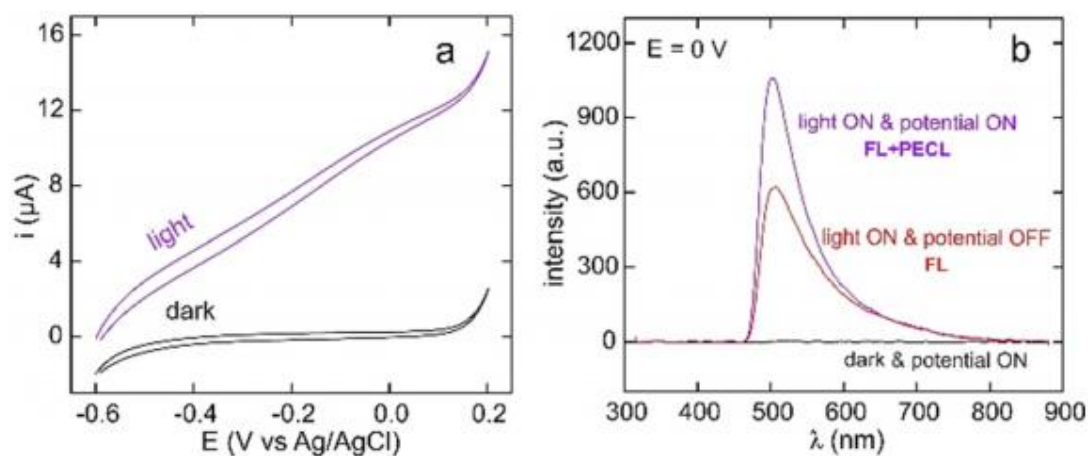


Figure 2.19 a) CVs recorded at BiVO₄ at 20 mVs⁻¹ in the dark (black) and under illumination (purple). b) Luminescence spectra recorded at 0 V in the dark (black curve), at open circuit under LED illumination (red curve, FL), and at 0 V under LED illumination (purple curve, FL+PECL). The measurements were recorded with P_{LED}=15.3 mW (λ_{exc} =375 nm) in 0.1M NaOH with an L-012 concentration of 10 mM.

Figure 2.19 a shows CVs recorded in the dark and under illumination (black and purple curves, respectively). While negligible currents were measured in the dark, an anodic photocurrent appeared under LED illumination, suggesting the consumption of the photogenerated holes in an oxidation process. This CV is very similar to those previously reported for BiVO₄ photoanodes²⁷ and demonstrates the photoactivity of our BiVO₄ surface under these conditions. The influence of the applied potential on luminescence is clearly shown in Figure 2.19 b. In the dark, no ECL appeared. Conversely, under illumination, intense ECL peaks appeared on the surface. The emission at the open circuit (red curve) is caused by the L-012 FL and exhibits a maximum at λ_{em} =503 nm. Remarkably, applying a potential E = 0 V to the BiVO₄ surface considerably amplifies the luminescence, resulting in an increase of the luminescence intensity (i.e. λ_{em}) by more than 70% (purple spectrum).

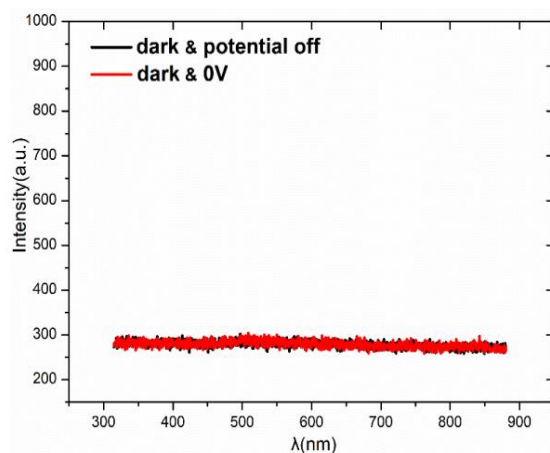


Figure 2.20 Spectra recorded at 0 V in the dark (red curve) and an open circuit in the dark (black curve).

Spectra were also performed in dark with potential on and off. Figure 2.20 proves that without LED illumination, no emission was measured regardless of whether a potential was applied (black curve) or not. To know the effect of LED power (P_{LED}) connected with a power generator, CVs and FL spectra were recorded at $BiVO_4$ by controlling the power source of LED (1.3 mW, 7.1 mW, and 15.3 mW). Figure 2.21a shows that photocurrent increases with the increase of P_{LED} . Thus, the effect of P_{LED} is remarkable because it allows control of the h^+ density and, thus, the photocurrent. Meanwhile, P_{LED} also has the same effect on the FL of L-012. Figure 2.21b shows FL intensity increase when the applied power increase.

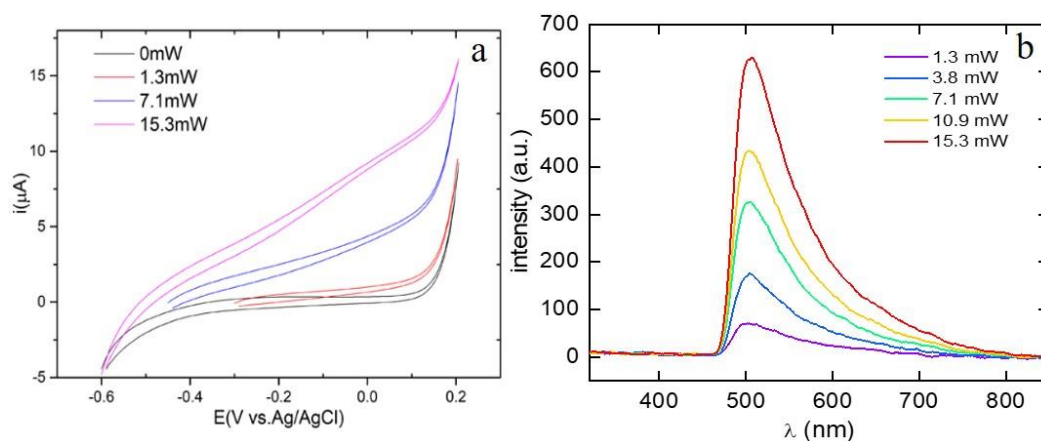


Figure 2.21 a) CVs recorded at $BiVO_4$ at 20 mV s^{-1} in the dark (black) and under illumination with an incident power of 1.3 (red), 7.1 (blue), and 15.3 mW (purple). b) FL spectra recorded in open-circuit conditions at different LED illumination powers (PLED).

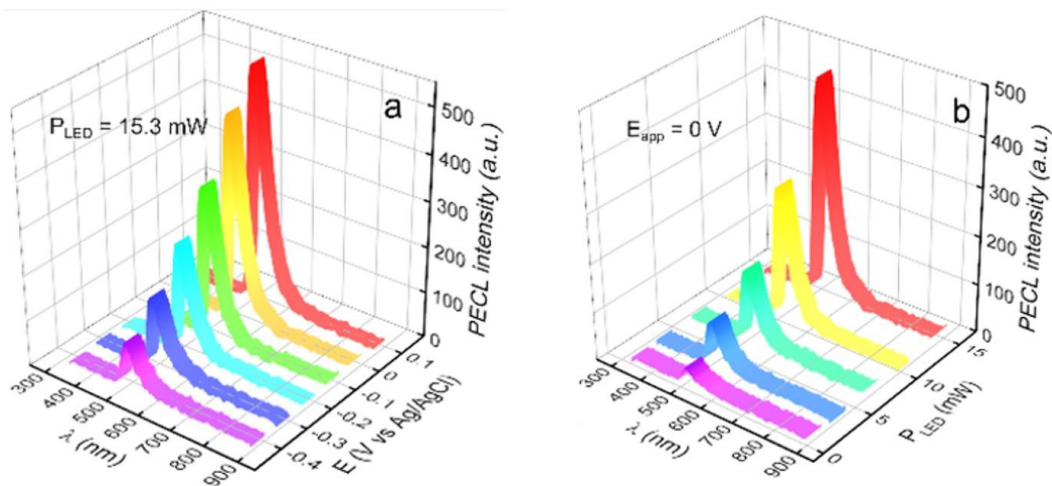


Figure 2.22 a) PECL spectra recorded with a constant LED illumination at different potentials E vs. Ag/AgCl. b) PECL spectra recorded at a constant potential (0 V) at different LED illumination power (P_{LED}).

To precisely focus on PECL, in the following, the FL spectrum (recorded before each measurement) was subtracted from the overall luminescence (FL + PECL). Figure 2.22 a shows the effect of E on PECL intensity in the -0.4 to 0.1 V range and reveals that PECL increases with potential increases. Precisely, its intensity increased by 5.5 times in this potential range. It is also striking to observe that PECL could be measured at a potential as low as -0.4 V (Figure 2.22 a, purple spectrum), which is, to the best of our knowledge, the lowest potential ever reported for ECL generation of a luminol derivative. In Figure 2.22 b, the effect of P_{LED} is clearly shown. P_{LED} is varied from 1.3 to 15.3 mW and the potential is kept constant ($E = 0$ V), PECL has a consistent response with the increase of P_{LED} . Thus, it proves clearly that P_{LED} has a strong influence on PECL and led to an increase in its intensity by more than 13 times.

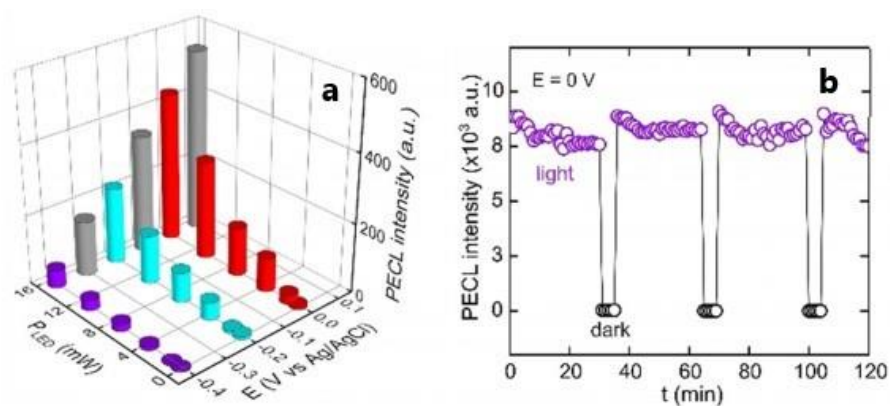


Figure 2.23 a) Graph showing the intensity of the PECL peak as a function of the applied potential and the illumination power. b) Graph showing the PECL intensity as a function of the time at 0 V under intermittent light illumination. PECL spectra were obtained by subtracting the FL spectra recorded under open-circuit potentials from

the luminescence spectra (FL+PECL). The measurements presented in panels (b) were recorded with $P_{LED}=15.3$ mW. All measurements were performed at $\lambda_{exc}=375$ nm in 0.1M NaOH with an L-012 concentration of 10 mM.

A series of results, obtained by varying E and P_{LED} , are gathered in Figure 2.23 a, which plots the PECL maximum intensity as a function of these parameters, and clearly illustrates how they influence PECL. While PECL is not generated at low P_{LED} , it becomes very high for high E and P_{LED} values. Quantitatively, the highest amplification was obtained for + 0.1 V and 15.3 mW. The electrochemical and spectroscopic data allows one to relate the luminescence amplification to the photoanodic activity of $BiVO_4$. At this stage, we rationally assume that PECL is triggered by the direct oxidation of the luminophores and the hydroxide anions by photogenerated h^+ .^{27, 33, 45} Nevertheless, it is also plausible that concomitant photoelectrochemical processes, such as a local pH decrease caused by OH^- consumption⁴⁶ or H_2O_2 generation,⁴⁷ could also play a role in the PECL, which would be investigated in future. The stability of this electrode was tested by measuring the PECL intensity as a function of time under intermittent illumination. 15.3 mW was used as PLED when the light is on. As shown in Figure 2.23 b, PECL responds instantaneously to illumination and is rather stable at 0 V over 2 hours.

2.4 Conclusion

In conclusion, we reported for the first time PECL of the aqueous model system $[Ru(bpy)_3]^{2+}/TPrA$, which was demonstrated at MIS n-Si/SiO_x/Ni photoanodes. The upconversion process ($\lambda_{exc} > \lambda_{emi}$), which combines photoactivation at the SC and electrochemistry, gives a remarkably stable and intense ECL emission in water at a low potential of 0.45 V vs SCE. Another PECL mechanism involving L-012 at $BiVO_4$ photoanodes using a light source at 375 nm, that is suitable for exciting the luminophore fluorescence as well as the SC photoelectrode, was studied. This system is the first example of PECL on an oxide photoelectrode. When an appropriate potential is applied to the photoanode, bright emission is obtained with a significant PECL contribution, which increases with the potential, to the overall light intensity. It has been shown that, because of the low oxidation potential of L-012, the high photovoltage, and the chemical stability of $BiVO_4$, PECL can be induced on the $BiVO_4$ surface at a lower potential than 0.4 V for several hours. This concept can be employed to precisely tailor L-012 emission and this report constitutes the first example of PECL where $\lambda_{exc} < \lambda_{emi}$. These findings show that the recent developments

in photoelectrode protection can be beneficial for applications outside energy, opening exciting opportunities in various fields such as ECL. Indeed, the concept of PECL can be applied to other types of reactions (including cathodic ones) on a variety of absorbing n- and p-type SCs, and thus, a wide range of PECL systems with different absorption/emission characteristics should be readily accessible. Besides being beneficial in terms of electrochemical potential gain, this concept may find application in biosensing, light-addressable systems, or for the design of new detection strategies and infrared imaging devices.

Experimental section

1. Photoinduced electrochemiluminescence at depleted semiconductor electrodes in water

1.1 Photoinduced electrochemiluminescence by Upconversion at Silicon Electrodes in Water

1.1.1 Material

Acetone (MOS electronic grade, Erbatron from Carlo Erba) and anhydrous ethanol (RSE electronic grade, Erbatron from Carlo Erba) were used without further purification. The ultrapure water had a resistivity of 18.2 M Ω cm (Purelab Classic UV). Sulfuric acid (96%, VLSI grade Selectipur) and hydrogen peroxide (30%, VLSI, Sigma-Aldrich) were purchased from BASF and Sigma Aldrich, respectively. Tris(bipyridine)ruthenium(II) chloride (Ru(bpy)₃Cl₂), tri-n-triethylamine (TPrA) were purchased from Sigma Aldrich. Phosphate buffer solution (PBS, 100 mM, pH 7.3) was prepared from sodium phosphate dibasic heptahydrate and sodium phosphate monobasic monohydrate that were purchased from Sigma Aldrich.

1.1.2 Electrode preparation

All vials and tweezers used for cleaning of silicon were previously decontaminated in 3/1 v/v concentrated H₂SO₄/30% H₂O₂ at 105 °C for 30 min, followed by copious rinsing with ultrapure water. The Ni thin films were deposited on the clean Si/SiO_x surfaces by sputtering with a Leica EM ACE600 coating system (Ni target purity: 99.8%, Leica). The Ar pressure for sputtering was 2 × 10⁻² mbar and the current 100 mA (pre-sputtering time of 1 min), the thickness of the film was determined in situ by a

quartz crystal microbalance. After deposition, the system was degassed with N₂. The coated surfaces were further processed to fabricate electrodes. The Ohmic contact was done on the backside of Si wafer by scratching the surface with a diamond glass cutter; then a droplet of InGa eutectic and a metal wire were applied on the scratched part. A thin layer of silver paste was painted to cover the InGa eutectic contact as well as a part of the metal wire. After drying of the paste, epoxy resin (Loctite 9460, Henkel) was deposited to shield the backside and frontside of the surface except an active area comprised between 0.1 and 0.2 cm², the exact geometrical value was precisely measured using the Image J software prior to the (photo)electrochemical experiments. The electrodes were baked in the oven at 90 °C for 1.5 h to cure the epoxy resin.

1.1.3 Electrochemical and photoelectrochemical experiments

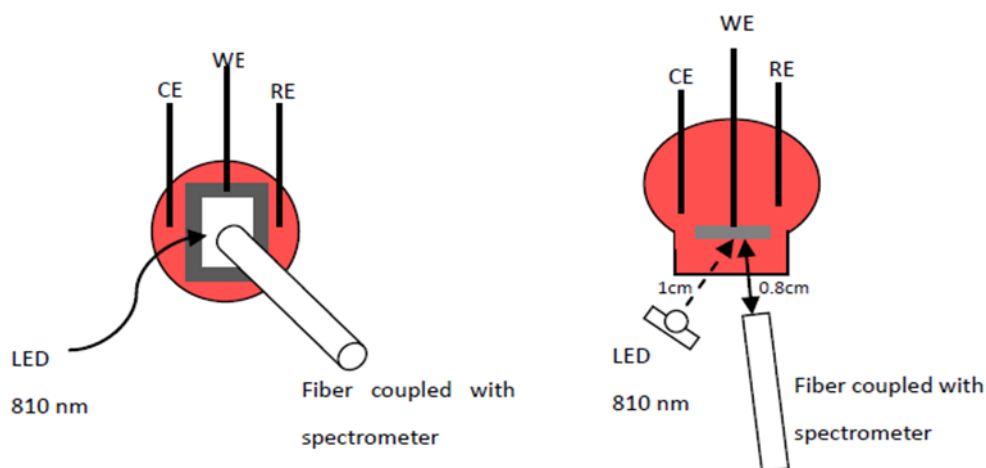


Figure 2.24 Set-up employed for P-ECL experiments, in front view(left) and in top view(right).

The P-ECL experiments were performed in a homemade cell comprising a quartz window in front of which was localized the photoelectrode. The LED and the optical fiber coupled to a spectrometer were placed in front of the quartz window (Figure 2.24) to illuminate the surface and simultaneously acquire ECL emission spectra every 500 ms, respectively. This setup allowed separation of the incident excitation LED light ($\lambda_{LED} = 810$ nm) from the ECL signal (i.e., λ_{ECL}) and enabled recording of the ECL intensity, which was integrated from 550 to 650 nm on the ECL spectra, as a function of the potential during CV cycles. The position of Si electrode, LED and fiber placed like a rectangle, to make sure the electrode can be irradiated by LED light can be observed and ECL light can be captured by optical fiber, which showed in the front view. The distance between LED and the Si electrode is 1cm, 0.8cm is the distance

between the Si electrode and optical fiber which is coupled with the spectrometer.

Cyclic voltammetry (CV), chronoamperometry (CA) and chronopotentiometry (CP) measurements were performed in a three-neck cell comprising a quartz window. The reference electrode was a KCl saturated calomel electrode (SCE) and the counter electrode was a graphite rod. The cell was filled with the electrolyte that comprised 5 mM $[\text{Ru}(\text{bpy})_3]^{2+}$, 100 mM TPrA in the buffer solution. The working electrode was placed in front of the quartz window. The light was provided by a LED (ILH-IX01-81SLSC201-WIR200, Radiospares) that was placed facing the quartz window with an angle of 45° and a distance from the electrode of ~ 1 cm. The power of the LED was controlled by the current applied with a power generator. Unless specified the applied current was 25 mA, which corresponds to a power density of 17.3 mW cm^{-2} , as measured with a PM200 Thorlabs powermeter fitted with a S130VC Thorlabs detector. Electrochemical measurements were performed with a SP150 (Biologic) or a μ -Autolab Type III (Autolab). The CVs reported in this work were recorded at 20 mV s^{-1} . ECL spectra were recorded using a spectrograph Spectra pro 2300i (Princeton Instrument) connected to a collecting optical fiber, under potential scanning with an exposure time of 0.5 s. The optical fiber was placed as well in front of the quartz window with a distance from the electrode of ~ 0.8 cm (see the scheme in Figure 2.2). ECL intensity was calculated by the integration of the ECL spectra from 550 nm to 650 nm and background spectra where the LED was ON and the cell was left at the OCP were recorded before each experiment and subtracted to the spectra. Photovoltages were estimated by subtracting the potential corresponding to an arbitrary set value of ECL intensity of 1×10^5 on $\text{p}^+\text{-Si/SiO}_x/\text{Ni}$ (in the dark) and $\text{n-Si/SiO}_x/\text{Ni}$ (under illumination). IPCE measurements were performed with a CIMPS-QE IPCE 3 workstation (Zahner) comprising a TLS03 tunable light source controlled by a PP211 potentiostat in the same cell as the one used for the classical electrochemical experiments and the applied potential was 0.7 V. The light modulation frequency was 1 Hz, the settling time was 10 s and the number of counts 25. The Thales software provided the spectra in photocurrent efficiency (A W^{-1}) or IPCE (%). In order to check the validity of the P-ECL measurements, the IPCE spectra obtained in A W^{-1} (Figure 2.7) allowed calculating that a theoretical current density of 0.95 mA cm^{-2} should be obtained at 810 nm with a power density of 17.3 mW cm^{-2} , which is (considering experimental errors related with the experimental setup) relatively close to the value of 1.2 mA cm^{-2} obtained at 0.7 V in Figure 2.11a, thus, confirming the validity of our measurements.

1.2 Luminescence Amplification at BiVO₄ Photoanodes by Photoinduced Electrochemiluminescence

1.2.1 Material

Acetone (technical grade, VWR) and ethanol (96%, Carlo Erba) were used without further purification. The ultrapure water had a resistivity of 18.2 MΩ cm (Purelab Classic UV). 8-amino-5-chloro-2,3-dihydro-7-phenyl-pyrido[3,4-d]pyridazine-1,4-dione (L-012) was purchased from FUJIFILM Wako Chemicals Europe GmbH. Fluorine doped tin oxide (FTO) plates, sodium hydroxide solution (100 mM), sodium hydroxide (>98%) and dimethyl sulfoxide (DMSO) (extra pure grade) were purchased from Sigma Aldrich. Bismuth (III) nitrate pentahydrate Bi(NO₃)₃·5H₂O (98%), and vanadyl acetylacetonate (99%) were purchased from Acros Organics.

1.2.2 Electrode preparation

FTO slides (1×2 cm²) were cleaned by a detergent (110551, Ecolab), rinsed copiously with ultrapure water and sonicated for 10 min successively in acetone, ethanol and ultrapure water.

They were finally rinsed and dried under an Ar flow. The method we used to coat these FTO surfaces with BiVO₄ was adapted from reference. We first electroplated metal Bi that was then converted in BiVO₄, as described in the following. The Bi plating electrolyte was prepared by dissolving 0.77 g of Bi(NO₃)₃·5H₂O in 80 ml of ethylene glycol. Before electrodeposition, a piece of copper tape was disposed at one extremity of a cleaned FTO slide (to be used as an electrical contact) that was then partially covered with hydrophobic tape (3M) to define a ~0.5 cm² active area. The electrochemical cell was an open beaker filled with the plating electrolyte, the working electrode was the FTO slide, the reference electrode was a KCl-saturated calomel electrode (SCE) and the counter electrode was a large Pt plate. Bi electroplating was carried out by chronoamperometry imposing 7 cycles composed of two steps (-1.85 V for 30 s followed by 0 V for 5 s) using a Biologic SP-150 potentiostat. After electrodeposition, the electrode was rinsed with ultrapure water and dried with Ar. After that, the copper and the hydrophobic tape were removed from the surface and 40 μL of a 0.15 M solution of vanadyl acetylacetonate in DMSO was cast over the surface to fully cover the Bi surface. The DMSO was evaporated by heating the surface for 20 min on a hot plate at 100°C and the surface was then annealed at 500 °C for 2 h in the air (2 °C min⁻¹) in a tube furnace (Carbolite EHA 12300). After annealing, the surface was immersed in a 1 M NaOH aqueous solution for 30 min under stirring to remove V₂O₅ from the layer. The surface was finally copiously rinsed with ultrapure water and dried under Ar.

1.2.3 Material characterization

XRD analysis was performed on a Rigaku SmartLab instrument (3 kW, Kalpha1,2 Cu) using grazing-incidence X-ray diffraction (GIXRD) with incident angle $\omega = 0.3^\circ$, incident slit of 0.2 mm, angular range 15-65°, speed 2°/min. Scanning electron microscopy (SEM) was performed using a JSM 7100F (JEOL). SEM picture analysis was performed using the ImageJ software. The colourized SEM pictures were prepared using the Inkscape freeware, the non-colourized SEM picture is presented in Figure 2.16.

1.2.4. Electrochemical, photoelectrochemical and optical characterization

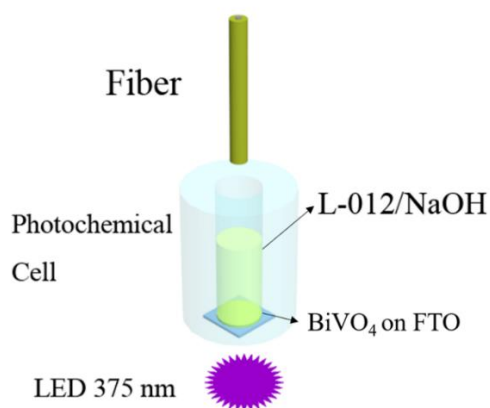


Figure 2.25 The set-up employed for P-ECL experiments.

The BiVO₄/FTO material was then employed as the anode in the photoelectrochemical cell which contained an electrolyte composed of 10 mM L-012 in 1M NaOH. This cell comprised an LED ($\lambda_{\text{exc}} = 375 \text{ nm}$), placed below the FTO side of the photoanode to illuminate it. An optical fiber was positioned above the BiVO₄ in the electrolyte solution and coupled to a spectrometer. This photoelectrochemical setup allowed to record emission spectra as a function of the incident illumination intensity (P_{LED}) and E. The FL of L-012 was measured under illumination when there is no applied potential, and when the potential was applied, PECL was therefore recorded and it amplifies the luminescence signal.

Cyclic voltammetry (CV) and chronoamperometry (CA) measurements were performed with a μ -Autolab Type III (Metrohm). The scan rate of CVs was 20 mV s⁻¹. Except for the electrodeposition experiments (introduced before), the reference was an Ag/AgCl (3 M NaCl) electrode and the counter electrode was a carbon rod. The working electrode was the FTO/BiVO₄ surface, which was sealed with

an O-ring (photoelectrochemically active surface area of $\sim 0.3 \text{ cm}^2$) at the bottom of a homemade open-top photoelectrochemical cell and a piece of copper tape was employed as an electrical contact. 5 mL of the ECL electrolyte, comprised of 10 mM L-012 dissolved in the 0.1 M NaOH solution, was injected into the cell and the two other electrodes were placed on the sides in order to prevent shadowing of the front surface. A 375 nm light-emitting diode (LED, 733-4745, Radiospares) filtered with a low bandpass filter was placed below the photoanode (Figure 2.25) to illuminate its backside of our (through the FTO). The LED was connected to a power generator that allowed to control the emission power intensity. A calibration curve (light power as a function of applied current) was recorded using a photodiode power sensor (S130VC, Thorlabs) connected with a power meter (PM200, Thorlabs) and allowed to measure the illumination power of the LED. Unless specified the applied current was 150 mA, which corresponds to a power of 15.3 mW.

ECL spectra were acquired by an optical fibre coupled to a spectrograph Spectra pro 2300i (Princeton Instrument) at different potentials with an exposure time of 0.1 s. The optical fibre was placed above the electrolyte/air interface at a distance of $\sim 4 \text{ cm}$ from the electrode. PECL+FL spectra were recorded from 200 nm to 900 nm under different power and at different potentials and FL spectra were recorded with LED ON but without applying a potential to the electrode (open circuit conditions). In Figure 2.19, the spectrum obtained in the dark in open circuit condition (presented in the red curve of Figure 2.19) was used as a background and subtracted to the spectra. The PECL intensity, presented in Figures 2.23 and 2.24 was obtained by subtracting the FL signal (recorded before the measurement at the open circuit) from the PECL+FL signal (recorded upon the application of a potential). UV/Vis absorption spectra were recorded by using a V-570 (Jasco) spectrophotometer. Photo-emission spectra were recorded with a Cary Eclipse (Varian) fluorescence spectrophotometer. The photocurrent spectroscopy experiments, that were performed to obtain the Tauc plot of Figure 2.17a, were acquired with a CIMPS-QE IPCE 3 workstation (Zahner) comprising a TLS03 tunable light source controlled by a PP211 potentiostat with a backside illumination in the ECL electrolyte.

References

1. Liu, X.; Jiang, H.; Lei, J.; Ju, H., *Analytical Chemistry* 2007, 79 (21), 8055-8060.
2. Jiang, C.; Moniz, S. J. A.; Wang, A.; Zhang, T.; Tang, J., *Chemistry Society Review* 2017, 46 (15), 4645-4660.
3. Lewis, N. S. *Inorganic chemistry* 2005, 44 (20), 6900-6911.

-
4. Seraphin, B. O., *Solar Energy Conversion: Solid-state Physics Aspects* 1979.
 5. Tan, M. X.; Laibinis, P. E.; Nguyen, S. T.; Kesselman, J. M.; Stanton, C. E., *Progress in inorganic chemistry* 1994, 41, 21-144.
 6. Laser, D.; Bard, A. J., *Chemical Physics Letters* 1975, 34 (3), 605-610.
 7. Luttmmer, J.; Bard, A. J., *Journal of the Electrochemical Society* 1979, 126 (3), 414.
 8. Zhao, Y.; Yu, J.; Xu, G.; Sojic, N.; Loget, G., *Journal of American Chemistry Society* 2019, 141 (33), 13013-13016.
 9. Yu, J.; Saada, H.; Abdallah, R.; Loget, G.; Sojic, N., *Angewandte Chemie International Edition English* 2020, 59 (35), 15157-15160.
 10. Sun, K.; Shen, S.; Liang, Y.; Burrows, P. E.; Mao, S. S.; Wang, D., *Chemical reviews* 2014, 114 (17), 8662-8719.
 11. Canda, R. M.; Kastner, M.; Goodman, R.; Hickok, N., *Journal of Applied Physics* 1976, 47 (6), 2724-2726.
 12. Ren, K.; Zhou, J.; Wu, H., *Accounts of chemical research* 2013, 46 (11), 2396-2406.
 13. Powell, L.; Wiederkehr, R. S.; Damascus, P.; Fauvart, M.; Buja, F.; Stakenborg, T.; Ray, S. C.; Fiorini, P.; Osburn, W. O., *Analyst* 2018, 143 (11), 2596-2603.
 14. Vogel, Y. B.; Gooding, J. J.; Ciampi, S., *Chemical Society Reviews* 2019, 48 (14), 3723-3739.
 15. Zhang, X. G., *Springer Science & Business Media*: 2007.
 16. Kenney, M. J.; Gong, M.; Li, Y.; Wu, J. Z.; Feng, J.; Lanza, M.; Dai, H., *Science* 2013, 342 (6160), 836-840.
 17. Loget, G.; Fabre, B.; Fryars, S.; Meriadec, C.; Ababou-Girard, S., *ACS Energy Letters* 2017, 2 (3), 569-573.
 18. Laskowski, F. A. L.; Nellist, M. R.; Venkatkarthick, R.; Boettcher, S. W., *Energy & Environmental Science* 2017, 10 (2), 570-579.
 19. Loget, G.; Mériadec, C.; Dorcet, V.; Fabre, B.; Vacher, A.; Fryars, S.; Ababou-Girard, S., *Nature communications* 2019, 10 (1), 1-11.
 20. Trotochaud, L.; Young, S. L.; Ranney, J. K.; Boettcher, S. W., *Journal of the American Chemical Society* 2014, 136 (18), 6744-6753.
 21. Burke, M. S.; Enman, L. J.; Batchellor, A. S.; Zou, S.; Boettcher, S. W., *Chemistry of Materials* 2015, 27 (22), 7549-7558.
 22. Aroonratsameruang, P.; Pattanasattayavong, P.; Dorcet, V.; Mériadec, C.; *The Journal of Physical Chemistry C* 2020, 124 (47), 25907-25916.
 23. Lambers, E. S.; Dykstal, C.; Seo, J. M.; Rowe, J. E.; Holloway, P. H., *Oxidation of metals* 1996, 45 (3), 301-321.
 24. Laskowski, F. A.; Nellist, M. R.; Venkatkarthick, R.; Boettcher, S. W., *Energy & Environmental Science* 2017, 10 (2), 570-579.
 25. Kim, T. W.; Choi, K.-S., *Science* 2014, 343 (6174), 990-994.
 26. Abdi, F. F.; Han, L.; Smets, A. H.; Zeman, M.; Dam, B.; Van De Krol, R., *Nature communications* 2013, 4 (1), 1-7.
 27. Kim, J. H.; Lee, J. S., *Advanced Materials* 2019, 31 (20), e1806938.
 28. Park, Y.; McDonald, K. J.; Choi, K. S., *Chemistry Society Review* 2013, 42 (6), 2321-37.
 29. Zhang, J.; Jin, R.; Jiang, D.; Chen, H.-Y., *Journal of the American Chemical Society* 2019, 141 (26), 10294-10299.
 30. Zhang, W.; Hao, L.; Huang, J.; Xia, L.; Cui, M.; Zhang, X.; Gu, Y.; Wang, P., *Talanta*

2019, 201, 455-459.

31. Liu, X.; Qi, W.; Gao, W.; Liu, Z.; Zhang, W.; Gao, Y.; Xu, G., *Chemical Communication (Camb)* 2014, 50 (93), 14662-5.
32. Kielland, A.; Blom, T.; Nandakumar, K. S.; Holmdahl, R.; Blomhoff, R.; Carlsen, H., *Free Radical Biology and Medicine* 2009, 47 (6), 760-766.
33. Cao, Z.; Su, B., *Electrochemistry Communications* 2019, 98, 47-52.
34. Modestov, A.; Gun, J.; Lev, O., *Surface science* 1998, 417 (2-3), 311-322.
35. Modestov, A. D.; Gun, J.; Lev, O., *Journal of Electroanalytical Chemistry* 1999, 476 (2), 118-131.
36. Koppenol, W., *Bioelectrochemistry and Bioenergetics* 1987, 18 (1-3), 3-11.
37. Ahmed, S.; Kishikawa, N.; Ohyama, K.; Maki, T.; Kurosaki, H.; Nakashima, K.; Kuroda, N., *Journal of Chromatography A* 2009, 1216 (18), 3977-3984.
38. Kulmala, S.; Ala-Kleme, T.; Kulmala, A.; Papkovsky, D.; Loikas, K., *Analytical Chemistry* 1998, 70 (6), 1112-1118.
39. Lind, J.; Merenyi, G.; Eriksen, T., *Journal of the American Chemical Society* 1983, 105 (26), 7655-7661.
40. Merenyi, G.; Lind, J.; Erikson, T. E., *Journal of the American Chemical Society* 1986, 108 (24), 7716-7726.
41. Merenyi, G.; Lind, J.; Shen, X.; Eriksen, T., *Journal of Physical Chemistry* 1990, 94 (2), 748-752.
42. Yu, J.; Kudo, A., *Advanced Functional Materials* 2006, 16 (16), 2163-2169.
43. Cooper, J. K.; Gul, S.; Toma, F. M.; Chen, L.; Liu, Y.-S.; Guo, J.; Ager, J. W.; Yano, J.; Sharp, I. D., *The Journal of Physical Chemistry C* 2015, 119 (6), 2969-2974.
44. Tokunaga, S.; Kato, H.; Kudo, A., *Chemistry of Materials* 2001, 13 (12), 4624-4628.
45. Lamm, B.; Zhou, L.; Rao, P.; Stefik, M., *ChemSusChem* 2018.



Chapter 3.

Electrochemiluminescent enantioselective detection with chiral-imprinted mesoporous metal surfaces

3.1 Introduction

Chirality is one of the properties of the object which cannot be indistinguishable or superimposed from

its mirror image, and the two mirror-image forms are generally named enantiomers.¹ Chirality can be defined at different length scales, ranging from the molecular to the supramolecular and macroscopic scale,² such as pharmaceuticals, biological molecules and agrochemicals. The chiral molecules (two enantiomers) have identical physical and chemical properties, like the same melting point, the same solubility, except for optical rotation. Since many biological molecules are enantiomers, they often play a mark difference on biological activities. In many cases, only one isomer in a chiral compound show the desired activity, while the other isomer may exhibit no therapeutic value and potentially cause unsuspected adverse effects. For instance, in drugs, often one of a drug's enantiomers is responsible for the desired physiological effects,³ while the other one is less active, inactive or sometimes even with the adverse effects. In the case of the human being, the stereoselectivity of receptors prefers for single D-sugar molecules to be used for energy production.⁴ Moreover, many important metabolic pathways of our bodies favour mostly L-amino acids as reactants, while the D-enantiomer is still not completely understood for its functions.⁵ Thus, the present technology for discrimination between enantiomers is of a consequential challenge to further being explicated in the more facile utilization together with higher sensitivity, especially in chemical, food, medical and pharmaceutical industries.⁶

Chiral discrimination approaches have been proposed relied on a large number of fundamental aspects. Previous reports have demonstrated the utilization of various analytically spectroscopic, e.g., UV-Vis spectrometry,⁷ fluorescence,⁸ H^1 nuclear magnetic resonance (H^1 -NMR)⁹ and circular dichroism (CD),¹⁰ polarimetric,¹¹ chromatographic^{12, 13} and electrochemical techniques¹⁴ for investigating the enantiomeric recognition of chiral molecules. However, these methods often suffer from some limitations related to the high cost for advanced instrumentation, the difficulty of sample purification or derivation, and time-consuming analytical processes.

Thus, there is still a strong need for the development of new and straightforward approaches allowing the discrimination of enantiomers. In this context, electrochemical concepts offer several advantages. One of them, which is of particular interest in terms of an easy readout and low cost, is ECL. ECL is a light-emitting phenomenon, which can be decomposed into three sequential main steps: i) the electrochemical trigger with the generation of reactive intermediates involving a luminophore and a sacrificial co-reactant; ii) their homogeneous reaction leading to the formation of the excited state of the luminophore; and iii) its relaxation to the ground state accompanied by photon emission. ECL provides several outstanding advantages, including no requirement of an excitation light source, high sensitivity

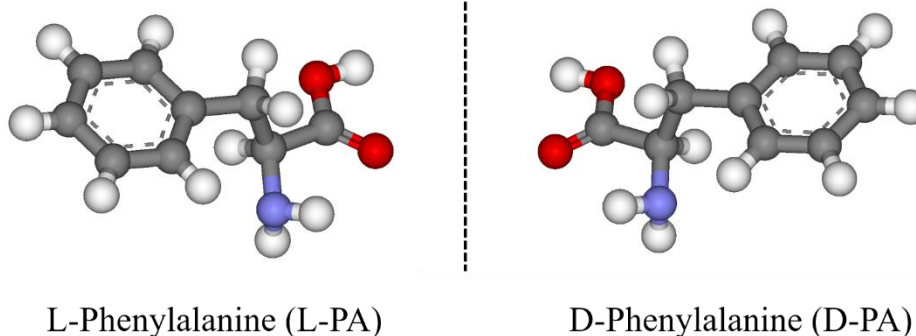
at physiological pH, simple instrumentation and detectable light emission, a controllable fine-tuning electrochemical reaction by an imposed potential and an ultrasensitive detection of the emitted light due to the nearly zero-background signal,¹⁵ allowing it can be achieved in a relatively low concentration ranging from 10^{-11} to 10^{-15} M,^{16,17} down to imaging at the single molecule level.¹⁸ In addition, ECL is considered as a rapid, cost-effective, and easy to operate technique. Qualitative and quantitative analysis of specific compounds can be carried out based on the luminescence produced by the electrochemical reaction occurring at the electrode surface. Up to now this approach has been also widely associated with other techniques for a large number of practical clinical and biological applications, such as bioassays for immunosensing,¹⁹ and imaging of (bio)chemical reactions.²⁰

ECL is a technique which is usually insensitive to chiral information, because its intrinsic readout signals such as the current, the wavelength or the intensity of the emitted light are identical for two enantiomers. Therefore, in general it is impossible to distinguish them. Recently, the circular polarization of the ECL emission providing valuable information on the excited state of the luminophore was reported. The two individual enantiomers of different luminophores (bispyrene organic macrocycle and the model $[\text{Ru}(\text{bpy})_3]^{2+}$) were detected selectively by circularly polarized-electrochemiluminescence (CP-ECL).¹⁹ Other groups reported stereoselective ECL sensors based on various ingredients.^{21, 22} For example, a molecular grafting approach was followed to anchor hemoglobin (Hb) on gold (Au) nanoparticles, which were then further immobilized on carbon nitride nanosheets (g- C_3N_4) for a final deposition on glassy carbon electrodes (Hb/Au-g- C_3N_4 /GCE) in order to discriminate penicillamine enantiomers.²³ In another study, cysteine (Cys) functionalized nitrogen-doped copper oxide/cobalt oxide (CuO/CoO) nanofibers (Cys@N-CuO/CoO NFs) have been proposed to distinguish the enantiomers of 3,4-dihydroxyphenylalanine (DOPA).²⁴ A chiral determination of cinchonine was detected with molecularly imprinted polymer membrane on the surfaces of magnetic microspheres by using an electrochemiluminescent sensor. Cinchonine was detected based on enhancement of the ECL intensity caused by the reaction of tertiary amino structures of cinchonine molecules with $[\text{Ru}(\text{bpy})_3]^{2+}$. This developed sensor improve specific recognition ability, providing a new method for testing and analyzing chiral substances on the basis of the special structure of 6-mercapto-beta-cyclodextrin.²⁵ In all these cases, a chiral molecular selector had to be integrated into the more or less complex architectures. Herein, we use a strategy that is completely different from CP-ECL or other electrochemiluminescent sensors, relying first of all on the fact that certain chiral molecules can play the role of ECL co-reactants, and

second, that the enantio-discrimination recognition occurs on metal surfaces, which are encoded with structural chiral information.

Apart from the technical point of view, a well-designed material should be also taken into consideration. Several alternative materials have been adopted into chiral discrimination and enantioselective analysis, for example, enantioselective membranes,²¹ molecularly imprinted polymers (MIPs)²² and modified cyclodextrins.²³ To meet the requirements for practical applications in terms of high productivity, low-cost manufacturing, friendly environmental issues, stereoisomeric capability, their stability is still the major negative aspect. Theoretically, a degree of chiral discrimination directly depends on chiral surface properties; in particular, a significant improved chiral recognition has been successful on mesoporous surfaces. Recently, novel chiral porous materials, namely chiral encoded mesoporous metals, have been successfully fabricated and combine the beneficial advantages of the mesoporosity, providing a high active surface area and improved mass transportation²⁴ with an enantioselective adsorption on metal surfaces.^{25, 26} To extend the scope of using this strategy to a wide range of metals, several noble and non-noble materials, such as monometallic platinum (Pt)^{27, 28} and nickel(Ni)²⁹ alloyed platinum-iridium (Pt-Ir) or the same alloys supported on nickel foam³⁰, have been investigated. These nanostructured surfaces could be successfully used as electrodes for the three major schemes of chiral technologies including a catalyst for asymmetric catalysis,³¹ a stationary phase for chiral separation³² a sensor for the chiral actuator,³³ and enantioselective analysis.³⁴ Chiral encoded mesoporous Pt could act as the stationary phase elaborated with the electro-assisted approach for the separation of enantiomers such as tryptophan and naproxen.^{35, 36} Furthermore, the chiral Pt electrode could be fabricated together with polypyrrole and this hybrid film revealed an efficient enantioselective actuation ability via wireless bipolar electrochemistry.³⁷ Monometallic Pt usually suffers from passivation after the reuse for many cycles, alloying metals like Pt-Ir could conquer the major difficulty. As illustrated in the latest reports,²⁵ when an alloy material with chiral properties, the chiral-encoded mesoporous Pt/Ir has been introduced instead of monometallic metals such as Pt, the remarkably improved enantioselective discrimination capability has been observed even after several recognition cycles using a simple electrochemical analysis such as differential pulse voltammetry (DPV). Interestingly, the designed materials also are resistant to harsh conditions, and therefore the high chiral discrimination capability is observed still even at high oxidative potentials. This notable stability also allows the usage of the Pt-Ir as a catalyst for the production of selective chiral molecules via both electrocatalysis²⁵ and chemical heterogeneous catalysis,³⁸ and the

catalyst revealed outstanding stability observed by highly enantiomeric excess values even after many catalytic cycles.



Scheme 1. Optimized structures of L-phenylalanine(left) and D- phenylalanine(right)

This structural stability makes an imprinted Pt-Ir alloy also a material of choice for a coupling with ECL, as high positive potentials have to be applied usually to the electrode for these experiments. By implementing together with the ECL approach, the chiral imprinted alloy should in this case generate an enantioselective ECL signal when one of the ingredients, either acted as the luminophore or the co-reactant with chiral features. In this contribution, a new dimension for enantioselective recognition of ECL is demonstrated on chiral-imprinted mesoporous Pt-Ir alloy. The chiral-imprinted mesoporous Pt-Ir alloy electrode was applied as a working electrode where the electrooxidation of chiral co-reactant molecules occurs and leads to ECL emission of the model $\text{Ru}(\text{bpy})_3^{2+}$ luminophore. In other words, to achieve enantioselective ECL detection, we target the initial electrochemical triggering step in this approach and not the final optical product, light and its polarization, as in previous works.^{39, 40} An amino acid, like phenylalanine (PA)(Scheme1), either D- or L- stereoisomeric enantiomers, was selected for this study to act as dual functional compound, a chiral target molecule as well as co-reactant for the ECL system.⁴¹ When the chiral Pt-Ir encoded with D-PA was used as a working electrode, remarkably different enantioselectivity between D- and L-PA was observed by ECL. As illustrated in Scheme 2, when Pt-Ir encoded with D-PA is used as a working electrode, an ECL signal with a significantly higher amplitude is expected for D-PA as an analyte compared to L-PA, due to a preferential oxidation at the specific chiral recognition sites. This concept opens up perspectives for a more general use of molecular-imprinted metals in combination with an ECL readout in advanced chiral technologies. This job is a collaboration with the group of Alexander Kuhn from University of Bordeaux, and Chularat Wattanakit

from Vidyasirimedhi Institute of Science and Technology.

3.2 Results and Discussion

Characterization of PA imprinted mesoporous Pt-Ir alloy

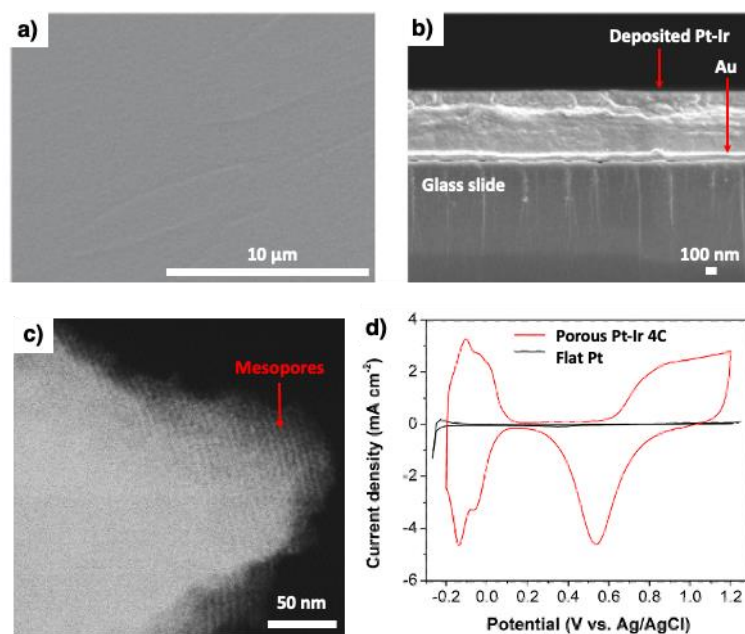


Figure 3.1 Characterization of chiral-imprinted mesoporous Pt-Ir electrode demonstrated SEM images with a) Top-view shown in scale bars of 10 μm , b) Cross-sectional view shown in scale bars of 100 nm. c) TEM image taken by STEM mode of the thin-layers porous Pt-Ir sample shown in scale bars of 50 nm; d) Cyclic voltammograms of porous Pt-Ir (red) and commercially flat Pt (black) scanning in 0.5 M H_2SO_4 solution at a scan rate of 100 mV s^{-1} . The Pt-Ir alloy is obtained by electrodeposition with a deposited charge density of 4 C cm^{-2} .

In this chapter, the co-electrodeposition of chloroplatinic acid hydrate ($\text{H}_2\text{PtCl}_6 \cdot x\text{H}_2\text{O}$) and dihydrogen hexachloroiridate (IV) hydrate ($\text{H}_2\text{IrCl}_6 \cdot x\text{H}_2\text{O}$), in the simultaneous presence of the columnar-shaped non-ionic surfactants, polyethylene glycol hexadecyl ether, and the chiral templates as either L- or D-phenylalanine (PA) with molar ratio of $\text{PA}/(\text{PtCl}_6^{2-} + \text{IrCl}_6^{2-}) = 1/12$, was used to elaborate the chiral encoded mesoporous Pt-Ir electrodes, analog to previous literature reports.²⁵ The deposited Pt-Ir alloy obtained by a deposition charge density of 4 C cm^{-2} provides outstanding properties such as a perfectly smooth outermost surface (Figure 3.1a) and a uniform thickness of the deposited Pt-Ir film approximately 500 nm (Figure 3.1b).²⁵ The scanning transmission electron microscopy (STEM) image (Figure 3.1c) reveals a highly ordered pore arrangement with an average diameter in a range of the mesopore approximately 5 nm, similar to what has been obtained previously.²⁴

To further verify the high porosity of the prepared porous Pt-Ir electrode, an enhanced active surface area can be emphasized by a significantly larger cyclic voltammetric (CV) curve with respect to that of the commercial flat Pt, analyzed in 0.5 M H₂SO₄ solution. Typically, the electrochemically active surface area is estimated in the region of hydrogen adsorption/desorption in a potential window between 0.0 to -0.25 V vs Ag/AgCl,⁴² and these measurements confirm that the significantly improved roughness factors in the case of the porous Pt-Ir approximately up to 100 order of magnitude compared to the commercial flat Pt (Figure 3.1d), indicating that the mesoporous structure has been successfully generated at the chiral porous Pt-Ir electrodes surface.

Electrochemical and ECL characterization of PA/[Ru(bpy)₃]²⁺ system on non-imprinted surfaces

As already mentioned, phenylalanine (PA), an amino acid, was selected as the dual-functional substrate to demonstrate chiroptical ECL-based detection, applied with an imprinting chiral template formed by Pt-Ir alloy surface. PA is also the sacrificial co-reactant and reacts with the model luminophore [Ru(bpy)₃]²⁺. Both compounds were dissolved in phosphate buffer solution (PBS, pH 7.3).

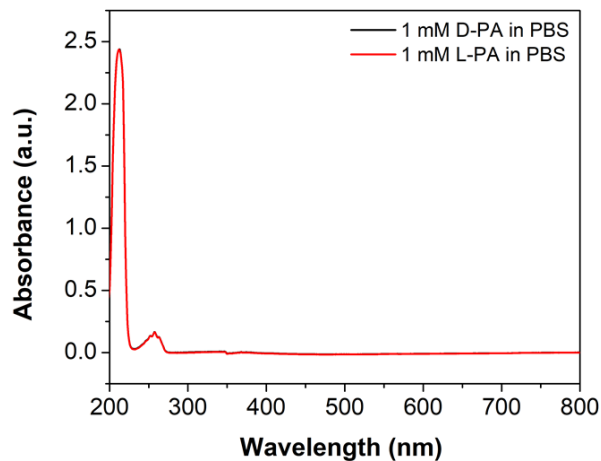


Figure 3.2 Physical properties of the PA enantiomer (UV-VIS spectra).

As expected, both PA enantiomers, either L-PA or D-PA, reveal identical optical properties as can be seen in the superimposed UV-Vis spectra of both enantiomers (Figure 3.2). This spectrum further confirms that the enantioselectivity on PA imprinted Pt-Ir alloy electrode is originated from the enantioselective

property of the electrode.

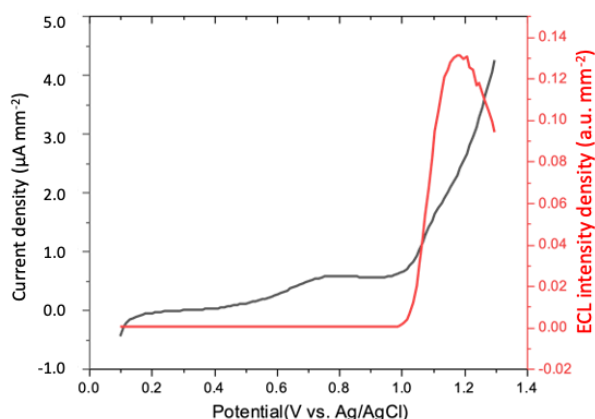


Figure 3.3 electrochemical and the ECL behaviors of the analyte solution on classical Pt electrode. The experiment was done in 10 mM PA dissolved in 1mM $[\text{Ru}(\text{bpy})_3]^{2+}$ solution.

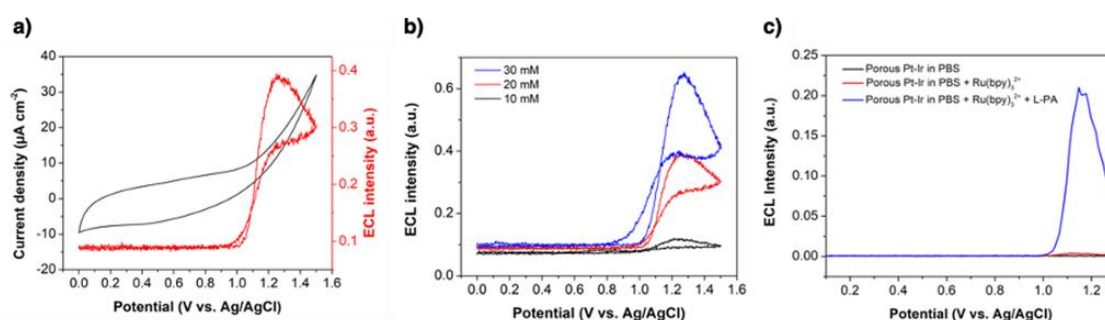


Figure 3.4. Control experiments demonstrating the behavior of non-imprinted mesoporous Pt-Ir alloys in different solutions and using different techniques: a) Cyclic voltammetry displays an important capacitive current combined with the ECL signal (CV-ECL); b) Effect of PA concentration on ECL intensity using CV-ECL; c) ECL intensity as a function of the composition of the solution recorded by DPV-ECL. Luminophore and co-reactant have to be present simultaneously to generate a significant ECL signal.

To verify the electrochemical behaviours of both PA and $[\text{Ru}(\text{bpy})_3]^{2+}$ in PBS solution, a classical Pt electrodes was used as a working electrode. As illustrated by Figure 3.3, the differential pulse voltammetry (DPV) curve clearly reveals the oxidation characteristics of PA and $[\text{Ru}(\text{bpy})_3]^{2+}$ at approximately 0.75 and 1.1 V vs Ag/AgCl/KCl 3M (all the potentials of this study are reported vs this reference electrode),^{43, 44} respectively. The ECL signal starts to be generated at 1 V, where the oxidation of the $[\text{Ru}(\text{bpy})_3]^{2+}$ complex occurs. It reaches to the maximum intensity at 1.15 V.⁴⁵ As expected, a classical Pt disk electrode does not provide any enantioselectivity either (signal ratio of 1.0 ± 0.3 ($n=5$)).

When using non-imprinted mesoporous Pt-Ir alloys as working electrodes (Figure 3.4a), a very pronounced capacitive current is observed due to their high active surface areas (Figure 3.1d). The ECL signal appears nevertheless at the same oxidation potential as for the classical Pt surface and its amplitude depends on the PA concentration (Figure 3.4b). In order to avoid the large capacitive currents, DPV was therefore chosen for further studying the chiral discrimination. The DPV-ECL detection was consecutively conducted by using non-imprinted mesoporous Pt-Ir electrodes in the PBS solution containing $[\text{Ru}(\text{bpy})_3]^{2+}$ (i.e. no PA) and $[\text{Ru}(\text{bpy})_3]^{2+}$ with PA dissolved. The corresponding ECL signals have been obtained (Figure 3.4c). In the solution containing only the supporting electrolyte (PBS), there is, as expected, no ECL signals. Nevertheless, a negligible ECL signal was found in the $[\text{Ru}(\text{bpy})_3]^{2+}$ solution. However, when adding the PA co-reactant to the $[\text{Ru}(\text{bpy})_3]^{2+}$ solution, strong ECL intensity is observed. These observations on non-imprinted mesoporous Pt-Ir alloy surfaces shows the importance of PA as a co-reactant and that ECL emission is generated at the oxidation potential of $[\text{Ru}(\text{bpy})_3]^{2+}$. It further indicates that the mechanism follows an oxidative-reduction route, like in the case of the well-known tri-n-propylamine (TPrA) combined with $[\text{Ru}(\text{bpy})_3]^{2+}$.⁴⁵

Chiral discrimination by ECL on imprinted Pt-Ir alloys

Although a simple electrochemical technique such as DPV can be used as a standalone technique for studying chiral recognition,²⁵ it may suffer from low sensitivity of chiral discrimination. Thus, its combination with enantioselective ECL emission on the chiral Pt-Ir alloys electrode, which can lead to a very significant signal improvement. Interestingly, the fresh L-PA imprinted mesoporous Pt-Ir reveals pronounced chiral recognition property with a five times higher ECL signal for L-PA compared to D-PA (Figure 3.5a). Similarly, D-PA gave a much stronger ECL signal recognition on the fresh D-PA imprinted mesoporous Pt-Ir electrodes with respect to L-PA solution (Figure 3.5b). Even though freshly prepared Pt-Ir electrodes can discriminate between PA enantiomers, the sensitivity of this ECL analysis is still limited as the surface can be gradually passivated by the adsorption of molecules. In order to enhance the ECL signal, a potential-induced surface regeneration concept was introduced. The metal surface was activated and cleaned by using chronoamperometry, applying a constant negative potential of -0.1 V for 30 s to remove any physisorbed species on the mesoporous metal surface before ECL analysis.⁴⁶

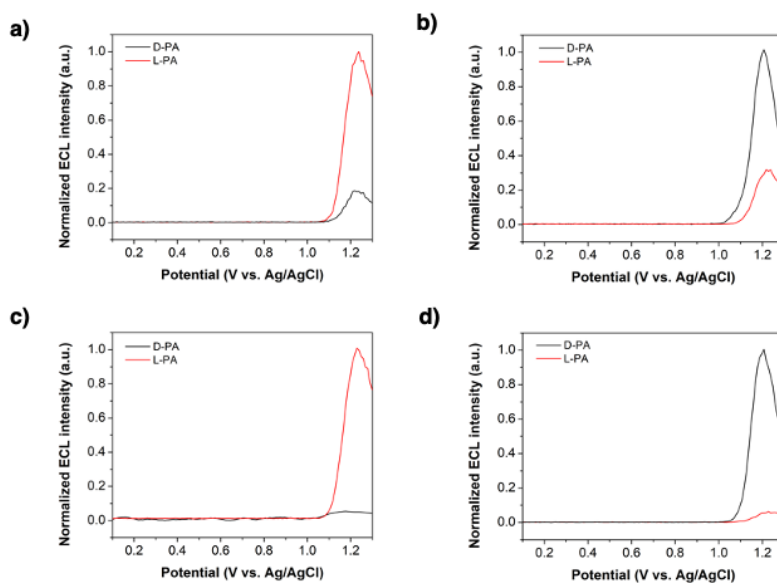
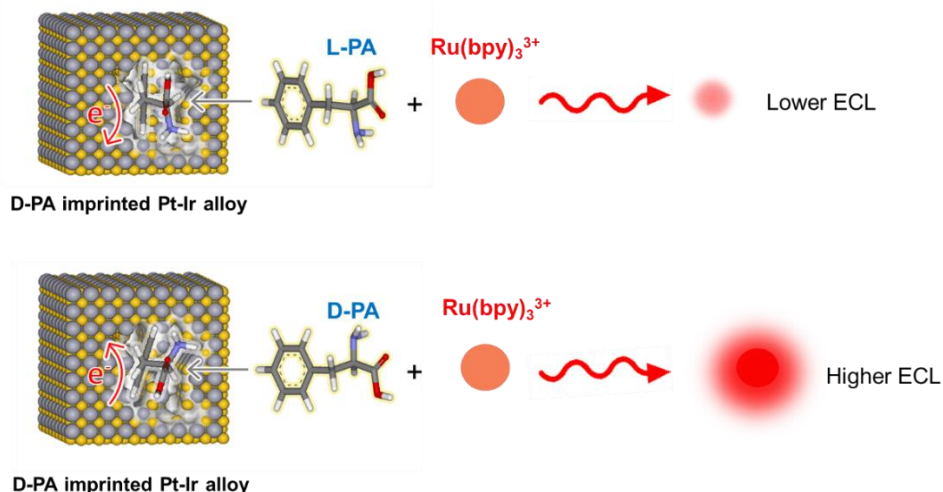


Figure 3.5 Chiral discrimination by ECL on fresh (upper row) and activated (lower row) Pt-Ir alloy electrodes, demonstrating the ECL signals for discrimination between PA enantiomers of a), c) L-PA, and b), d) D-PA imprinted Pt-Ir electrodes. The experiments were conducted in both 10 mM L-PA and D-PA/1 mM $[\text{Ru}(\text{bpy})_3]^{2+}$ dissolved in 0.1 M PBS solutions using the DPV-ECL technique.

Interestingly, as shown in Figure 3.5c and d, the discrimination ability between L-PA and D-PA is dramatically improved in this case. The enantioselectivity values for L-PA and D-PA recognition, expressed by the ratio of the respective ECL signals, reaches values of over 20. These values are approximately five times (4.9 ± 1.6) higher than those of the non-activated PA imprinted Pt-Ir electrodes. This enhanced enantioselectivity could be ascribed to the fact that the cleaning step equally affects the enantioselective internal surface of mesopores and the unselective outer surface of the Pt-Ir layer. As the mesopores represent a higher fraction of the total available surface area, this leads to a relative increase of the signal of the imprinted species, which preferentially reacts inside the pores. This results in a higher probability for the bimolecular reaction between oxidized $[\text{Ru}(\text{bpy})_3]^{2+}$ and PA species to occur in a stereoselective way, and consequently generates a significantly larger ECL signal for the imprinted enantiomer (Scheme 2).⁴⁷

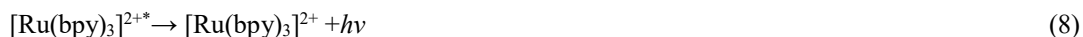
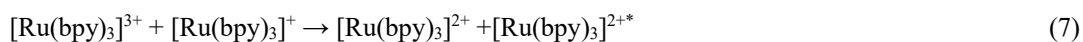


Scheme 2. Illustration of the reaction between $[\text{Ru}(\text{bpy})_3]^{3+}$ and PA radical generated through the oxidation in cavies on D-PA imprinted mesoporous Pt-Ir alloys electrode surface.

In this case, the ECL pathway would be proposed similar to the Miao *et al.* report in the $[\text{Ru}(\text{bpy})_3]^{2+}$ /TPrA system as mentioned in the introduction part.⁴⁵ The ECL generation and discrimination process is displayed in Scheme 2. Briefly, the reaction routes mainly relate to the three parts include: (i) and (ii) the direct oxidation of PA (1) and $[\text{Ru}(\text{bpy})_3]^{2+}$ (3) at the Pt-Ir electrode surfaces, respectively, and (iii) the generated $[\text{Ru}(\text{bpy})_3]^{2+}$ react to the PA^{\bullet} radical species at the excited state (4) to promote the light emission (5). The simplified equations to demonstrate the major routes are shown below,



Notably, in case of an excess of co-reactant like PA compared to $[\text{Ru}(\text{bpy})_3]^{2+}$, $[\text{Ru}(\text{bpy})_3]^{2+\bullet}$ species could be also created upon alternative routes. As shown in (6), $[\text{Ru}(\text{bpy})_3]^{2+}$ oxidize PA^{\bullet} radical species, resulting in a possibly annihilation pathway between the $[\text{Ru}(\text{bpy})_3]^{3+}$ and $[\text{Ru}(\text{bpy})_3]^{2+}$ to produce the excited $[\text{Ru}(\text{bpy})_3]^{2+\bullet}$ reactive species (7), with the light emission.



Reusability testing of the chiral-encoded Pt-Ir alloys for discrimination of enantiomers using ECL approach

As these ECL experiments require quite high positive potentials, which might lead to an oxidation of the metal surface and thus to a gradual loss of chiral information, the stability and reusability of the chiral imprinted Pt-Ir alloy during several cycles for the ECL enantioselective discrimination were investigated.

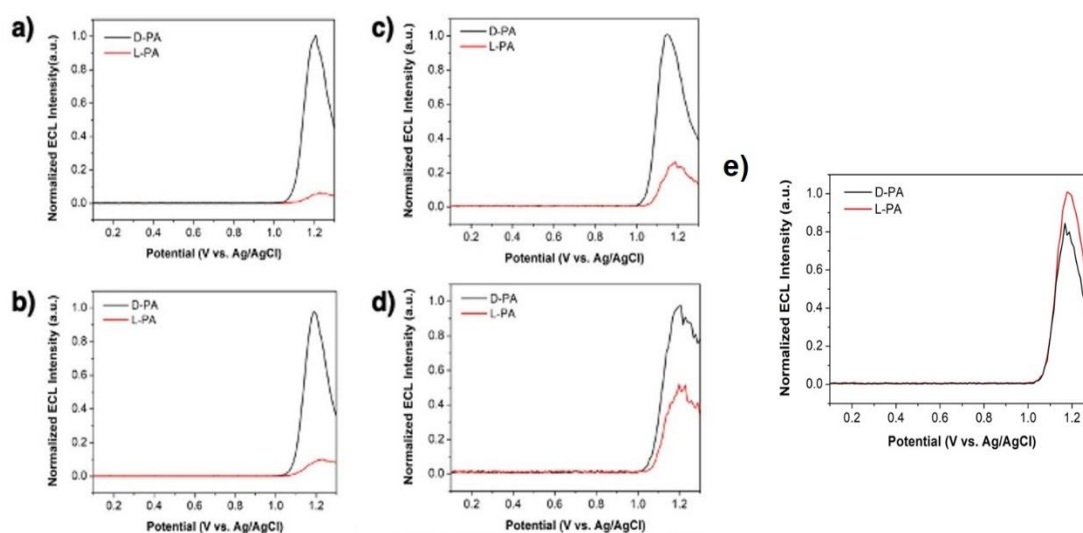


Figure 3.6 Reusability testing of the D-PA imprinted mesoporous Pt-Ir for the discrimination of PA enantiomers by ECL analyzed in L- or D-PA and $[\text{Ru}(\text{bpy})_3]^{2+}$ dissolved in PBS system. a), b), c), d) and e) represent ECL intensities for the experimental runs in the first to fifth cycles, respectively. The experiment was done in 10mM PA dissolved in 1mM $[\text{Ru}(\text{bpy})_3]^{2+}$ solution. After each analysis, the Pt-Ir electrode was rinsed and cleaned in MilliQ water for 6 h. Surface regeneration by chronoamperometry at -0.1 V for 30 s was applied before each analysis. The same Pt-Ir electrode was used in all cases.

Figure 3.6a shows the ECL responses of a D-PA imprinted Pt-Ir surface in presence of D- and L-PA during the first anodic scan of fresh electrodes. It shows a good enantioselectivity. Figure 3.6b-e displays the ECL signals recorded during the next 4 anodic scans with the same electrode. The ECL intensity measured in the solution containing L-PA tends to increase in comparison to D-PA (Figure 3.6a-e). It shows that the D-PA imprinted Pt-Ir can be reused up to five detection cycles, despite a decrease in

enantioselectivity values summarized in Figure 3.7. This ratio ranges from around 18.0 (1st cycle) to 10.0 (2nd cycle), 3.8 (3rd cycle), 2.0 (4th cycle) and 0.8 (5th cycle), respectively.

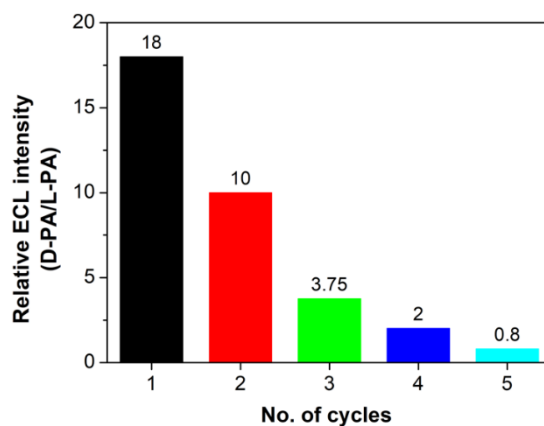


Figure 3.7 Histogram displays the relationship between the calculated enantioselectivity of D-PA versus L-PA concerning the number of cycles of the DPV-ECL analysis using the reused D-PA imprinted mesoporous Pt-Ir electrode.

The sensible decrease of the enantioselectivity relates to formation of metal oxide while applying highly anodic potentials up to 1.3 V. Despite the fact that surface regeneration by chronoamperometry at the very beginning of the negative potential would generate the cleaned active metal surfaces, for which before every single analysis it was applied, the generated metal oxide partially hinders the direct oxidation of PA on Pt-Ir alloy surfaces after many catalytic cycles, resulting in significantly the diminished ECL intensities.⁴⁸ It should be noted that in the previous report,²⁵ the chiral imprinted Pt-Ir alloys demonstrated very promising discrimination ability of enantiomers even after several excursions to highly positive potentials. However, in the previous case, the experiment was carried out in an acidic halide solution (hydrochloric acid, pH at 1.3) in which the halide species may prevent the growth of metal oxide surfaces, eventually allowing a more efficient electro-oxidation of the reactants.^{49,50} In strong contrast to this, the ECL analysis in this present study was conducted in the neutral PBS solution (pH 7.3), and therefore, the surface passivation leads to a gradual decrease in enantiomeric discrimination efficiency.

3.3 Conclusion

In summary, the results demonstrated for the first time that the chiral imprinted mesoporous Pt-Ir alloy can be used as a working interface to achieve enantio-discrimination by ECL. The selected amino acid, phenylalanine, was efficiently employed as a co-reactant to generate the stereoselective emission of ECL signals, depending on the chirality of the recognition sites imprinted in the metal structure. Most importantly, the results exhibit that whether fresh or activated Pt-Ir electrodes, the material can be effectively applied for chiral detection by ECL technique. A pronounced selectivity, transduced by a 20 times more intense light emission for the target enantiomer, was observed. This first example illustrates the power of using an ECL-based readout, combined with its usual advantages such as a low background signal. As the ECL activity is based on the presence of the amino group in the target molecule, it is easy to imagine that the strategy can be extended to other molecules with amino functions, and most importantly to other members of the family of amino acids. Therefore, the findings of these first proof-of-principle experiments open up interesting perspectives for the development of other molecular encoded metal structures able to be used for such an optical detection strategy.

Experimental section

2.1 Chemicals

(L)-phenylalanine (L-PA) was purchased from Tokyo Chemical Industry (TCI), while (D)-phenylalanine (D-PA), Hydrogen hexachloroplatinate(IV) hexahydrate ($\text{H}_2\text{PtCl}_6 \cdot 6\text{H}_2\text{O}$), dihydrogen hexachloroiridate(IV) hydrate ($\text{H}_2\text{IrCl}_6 \cdot x\text{H}_2\text{O}$), polyethylene glycol hexadecyl ether (Brij® C10), sodium phosphate dibasic heptahydrate ($\text{Na}_2\text{HPO}_4 \cdot 7\text{H}_2\text{O}$), sodium phosphate monobasic monohydrate ($\text{NaH}_2\text{PO}_4 \cdot \text{H}_2\text{O}$) and Tris(2,2'-bipyridyl) dichlororuthenium(II) hexahydrate ($\text{Ru}(\text{bpy})_3\text{Cl}_2 \cdot 6\text{H}_2\text{O}$) were received from Sigma-Aldrich. Phosphate buffer solution (PBS,) for 1 M at solution pH of 7.33 was prepared from $\text{Na}_2\text{HPO}_4 \cdot 7\text{H}_2\text{O}$ and $\text{NaH}_2\text{PO}_4 \cdot \text{H}_2\text{O}$ dissolved in MilliQ water. Sulfuric acid (H_2SO_4) was obtained from Alfa. MilliQ water (18.2 M Ω cm) was applied for all experiments. All chemicals were immediately used without further purification.

2.2 Synthesis of phenylalanine (PA)-encoded mesoporous Pt-Ir alloy electrodes

The synthesis of such electrodes was carried out upon electrochemically depositing approach by a three-electrode system performed on a potentiostat (Metrohm μ Autolab Type III) using Ag/AgCl (sat. KCl),

Pt mesh (geometrical area as 1 cm²), and prepared Pt-Ir alloy electrodes (geometrical area as 0.25 cm²) as a reference, counter and working electrodes, respectively. All corresponding results were analyzed using the Nova (version 1.11) program originally provided with the instrument. Initially, a gold-coated glass slide was cleaned by sonicating in 2-propanol for 15 min, and then rinsing with MilliQ water several times before drying under nitrogen (N₂) gas flow. The chiral-imprinted mesoporous Pt-Ir electrodes were prepared following the previously reported procedure with some modifications²⁵ with different chiral templates. In the typical procedure, the alloying electrodes have been obtained by co-electrodeposition of the prepared gel containing 28 wt% of the Pt and Ir salts (H₂PtCl₆·6H₂O and H₂IrCl₆·6H₂O, for 85 at% Pt and 15 at% Ir, respectively) in the presence of non-ionic surfactants (Brij® C10, 28 wt%) formed in hexagonal phase dissolved in MilliQ water (36 wt%), and the chiral templates as either L-PA or D-PA by a molar ratio of 1/12 (PtCl₆²⁻ + IrCl₆²⁻). All synthesized electrodes were conducted on a cleaned gold-coated glass slide as a support with applied potential at -0.05 V vs Ag/AgCl, and the controlled thickness by a charge density of 4 C cm². Finally, all templates including chiral molecules and surfactants were completely removed by rinsing for several times and immersing overnight with MilliQ water.

2.3 Characterization of chiral-encoded mesoporous Pt-Ir alloy electrodes

Scanning Electron Microscopy (SEM) was used to explore the surface morphology of the Pt-Ir electrodes operated on a Hitachi TM-1000 tabletop microscope; furthermore, the cross-sectional imaging of such electrodes were analyzed by SEM performed on a JEOL, JSM-7610F. The mesoporous structure of the Pt-Ir alloys was confirmed by the Transmission Electron Microscopy (TEM) performed on a JEOL JEM-ARM200F microscope at 200 kV. To prepare a Pt-Ir layers for TEM measurement, the deposited Pt-Ir layers were removed out from the substrate by gently mechanical scraping. The samples were dispersed in ethanol, and the resultant was finally dropped on the copper (Cu)-TEM grids for analysis. To verify the electrochemically active surface areas (ECSA), the electrochemical characterization as cyclic voltammetry (CV) was applied by scanning the mesoporous Pt-Ir electrodes in 0.5 M H₂SO₄ at a scan rate of 100 mV s⁻¹. The ECSA of the prepared electrodes was calculated from the hydrogen adsorption/desorption regions of the obtained CV curves following the literature.

2.4 Electrochemistry and electrochemiluminescence (ECL) analysis

The chiral discrimination were performed by the differential pulsed voltammetry (DPV) (step potential

10 mV, modulation amplitude 50 mV, modulation time 50 ms, interval time 500 ms), with 10 mM PA and 1mM Ru(bpy)₃²⁺ in 1 M PBS solution as supporting electrolyte (pH 7.33) in a potential window ranging from -0.1 to 1.3 V. The DPV was scanned on either a classical Pt electrode (3 mm of dimension) or a prepared chiral-imprinted Pt-Ir electrode as working electrodes, platinum mesh (geometrical area for 1 cm²) as counter electrode and an Ag/AgCl/KCl (sat. KCl) as the reference electrode performed on a μ Autolab type III potentiostat. Prior to analysis, the classical Pt electrode was polished with a 0.25 μ m diamond paste (Struers) and rinsed with ethanol and MilliQ water several times. Regeneration of the electrode surfaces was obtained by applying with chronoamperometry at -0.1 V for 30 s in the 0.1 M PBS solution.

ECL spectra were collected in a homemade cell with a Hamamatsu R5070A photomultiplier tube (PMT detector) which was placed at about 2 millimetres from the working electrode. The PMT detector was held at -750 V with a Hamamatsu C9525 high-voltage power supply. The obtained signal was amplified by a Keithley 6485 Picoammeter, and the resultant was consequently acquired via the second input channel of the μ Autolab type III potentiostat. All ECL spectra were recorded immediately after the working electrode was placed into the solution. All experiments were done in a dark room.

Enantioselectivity (R_L or R_D) between L- and D-phenylalanine (PA) was calculated following these relationships:

$$R_L = \frac{I_L - I_D}{I_L + I_D} \quad (1)$$

$$R_D = \frac{I_D - I_L}{I_D + I_L} \quad (2)$$

Where I_L and I_D are the maximum ECL intensities that were analyzed in L-PA and D-PA solutions, respectively.

References

1. Janssens, S.; Borgoo, A.; Alsenoy, C. V.; Geerlings, P., *The Journal of Physical Chemistry A* 2008, 112 (42), 10560-10569.
2. Morrow, S. M.; Bissette, A. J.; Fletcher, S. P., *Nature nanotechnology* 2017, 12 (5), 410-419.
3. Ariens, E., *European journal of clinical pharmacology* 1984, 26 (6), 663-668.
4. Mason, S. F., *Chirality* 1989, 1 (3), 183-191.
5. Sugahara, H.; Meinert, C.; Nahon, L.; Jones, N. C.; Hoffmann, S. V.; Hamase, K.; Takano, Y.; Meierhenrich, U. J., *Biochimica et Biophysica Acta (BBA)-Proteins and Proteomics* 2018, 1866 (7), 743-758.
6. Maier, N. M.; Franco, P.; Lindner, W., *Journal of Chromatography A* 2001, 906 (1-2), 3-33.

-
7. Zor, E.; Bekar, N., *Biosensors and Bioelectronics* 2017, 91, 211-216.
 8. Su, W. C.; Zhang, W. G.; Zhang, S.; Fan, J.; Yin, X.; Luo, M. L.; Ng, S. C., *Biosensors and Bioelectronics* 2009, 25 (2), 488-492.
 9. Grieb, S. J. University of Warwick, 1995.
 10. Tang, Y.; Cohen, A. E., *Science* 2011, 332 (6027), 333-336.
 11. Goodall, D. M., *Trends in Analytical Chemistry* 1993, 12 (4), 177-184.
 12. Yashima, E.; Yamamoto, C.; Okamoto, Y., *Journal of the American Chemical Society* 1996, 118 (17), 4036-4048.
 13. Hung, C.-Y.; Huang, H.-H.; Hwang, C.-C., *Eclética Química* 2005, 30, 67-73.
 14. Mahadevan, S.; Palaniandavar, M., *Bioconjugate chemistry* 1996, 7 (1), 138-143.
 15. Richter, M. M., *Chemical Reviews* 2004, 104 (6), 3003-3036.
 16. Wu, Y.; Li, X.; Tan, X.; Feng, D.; Yan, J.; Zhang, H.; Chen, X.; Huang, Z.; Han, H., *Electrochimica Acta* 2018, 282, 672-679.
 17. Zhang, M.; Ge, L.; Ge, S.; Yan, M.; Yu, J.; Huang, J.; Liu, S., *Biosensors and Bioelectronics* 2013, 41, 544-550.
 18. Du, F.; Chen, Y.; Meng, C.; Lou, B.; Zhang, W.; Xu, G., *Current Opinion in Electrochemistry* 2021, 28, 100725.
 19. Zanut, A.; Fiorani, A.; Canola, S.; Saito, T.; Ziebart, N.; Rapino, S.; Rebecani, S.; Barbon, A.; Irie, T.; Josel, H.-P., *Nature communications* 2020, 11 (1), 1-9.
 20. Han, D.; Goudeau, B.; Manojlovic, D.; Jiang, D.; Fang, D.; Sojic, N., *Angewandte Chemie* 2021, 133 (14), 7764-7768.
 21. Kim, J. H.; Kim, J. H.; Jegal, J.; Lee, K.-H., *Journal of Membrane Science* 2003, 213 (1-2), 273-283.
 22. Hart, B. R.; Rush, D. J.; Shea, K. J., *Journal of the American Chemical Society* 2000, 122 (3), 460-465.
 23. Easton, C. J.; Lincoln, S. F., *Chemical Society Reviews* 1996, 25 (3), 163-170.
 24. Attard, G. S.; Bartlett, P. N.; Coleman, N. R.; Elliott, J. M.; Owen, J. R.; Wang, J. H., *Science* 1997, 278 (5339), 838-840.
 25. Butcha, S.; Assavapanumat, S.; Ittisanronnachai, S.; Lapeyre, V.; Wattanakit, C.; Kuhn, A., *Nature communications* 2021, 12 (1), 1-9.
 26. Durán Pachón, L.; Yosef, I.; Markus, T.; Naaman, R.; Avnir, D.; Rothenberg, G., *Nature Chemistry* 2009, 1 (2), 160-164.
 27. Lin, F.; Peng, H.-Y.; Chen, J.-X.; Chik, D. T.; Cai, Z.; Wong, K. M.; Yam, V. W.; Wong, H. N., *Journal of the American Chemical Society* 2010, 132 (46), 16383-16392.
 28. Yutthalekha, T.; Wattanakit, C.; Lapeyre, V.; Nokbin, S.; Warakulwit, C.; Limtrakul, J.; Kuhn, A., *Nature communications* 2016, 7 (1), 1-8.
 29. Assavapanumat, S.; Ketkaew, M.; Kuhn, A.; Wattanakit, C., *Journal of the American Chemical Society* 2019, 141 (47), 18870-18876.
 30. Assavapanumat, S.; Butcha, S.; Ittisanronnachai, S.; Kuhn, A.; Wattanakit, C., *Chemistry—An Asian Journal* 2021, 16 (21), 3345-3353.
 31. Blaser, H. U.; Federsel, H.-J., John Wiley & Sons: 2011.
 32. Subramanian, G., John Wiley & Sons: 2008.
 33. Zhou, Y.; Tan, J.; Chong, D.; Wan, X.; Zhang, J., *Advanced Functional Materials* 2019, 29 (33), 1901202.

-
34. Wattanakit, C.; Côme, Y. B. S.; Lapeyre, V.; Bopp, P. A.; Heim, M.; Yadnum, S.; Nokbin, S.; Warakulwit, C.; Limtrakul, J.; Kuhn, A., *Nature communications* 2014, 5 (1), 1-8.
 35. Wattanakit, C.; Kuhn, A., *Chemistry-A European Journal* 2020, 26 (14), 2993-3003.
 36. Assavapanumat, S.; Yutthalekha, T.; Garrigue, P.; Goudeau, B.; Lapeyre, V.; Perro, A.; Sojic, N.; Wattanakit, C.; Kuhn, A., *Angewandte Chemie International Edition* 2019, 58 (11), 3471-3475.
 37. Assavapanumat, S. Université de Bordeaux; Vidyasirimedhi Institute of Science and Technology, 2020.
 38. Tao, F. F., *Chemical Society Reviews* 2012, 41 (24), 7977-7979.
 39. Zinna, F.; Voci, S.; Arrico, L.; Brun, E.; Homberg, A.; Bouffier, L.; Funaioli, T.; Lacour, J.; Sojic, N.; Di Bari, L., *Angewandte Chemie International Edition* 2019, 58 (21), 6952-6956.
 40. Voci, S.; Zinna, F.; Arrico, L.; Grass, S.; Bouffier, L.; Lacour, J.; Di Bari, L.; Sojic, N., *Chemical Communications* 2020, 56 (44), 5989-5992.
 41. Zhao, C.; Xu, S.; Su, Y.; Zhao, G., *Analyst* 2002, 127 (7), 889-891.
 42. Łukaszewski, M.; Soszko, M.; Czerwiński, A., *Journal of Electrochemistry Science* 2016, 11 (6), 4442-4469.
 43. Klymenko, O. V.; Svir, I.; Amatore, C., *ChemPhysChem* 2013, 14 (10), 2237-2250.
 44. Sentic, M.; Milutinovic, M.; Kanoufi, F.; Manojlovic, D.; Arbault, S.; Sojic, N., *Chemical Science* 2014, 5 (6), 2568-2572.
 45. Miao, W.; Choi, J.-P.; Bard, A. J., *Journal of the American Chemical Society* 2002, 124 (48), 14478-14485.
 46. Devadas, B.; Periasamy, A. P.; Bouzek, K., *Coordination Chemistry Reviews* 2021, 444, 214062.
 47. Rebecani, S.; Zanut, A.; Santo, C. I.; Valenti, G.; Paolucci, F., *Analytical Chemistry* 2021.
 48. Olsson, L.; Fridell, E., *Journal of Catalysis* 2002, 210 (2), 340-353.
 49. Zu, Y.; Bard, A. J., *Analytical chemistry* 2000, 72 (14), 3223-3232.
 50. Majd, M. M.; Farrokhpour, H.; Chermahini, A. N.; Dabbagh, H. A., *Journal of Molecular Structure* 2021, 130904.



Conclusions and Perspectives

The studies presented in this thesis aim at introducing new concepts related to ECL, photo-induced electrochemiluminescence on semiconductor electrode based on its photoelectrochemistry character under illumination in model ECL systems, and the chiral ECL for enantiomeric discrimination on chiral compound imprinted metal electrode.

In chapter 2, a new concept, named photo-induced electrochemiluminescence were firstly investigated on two kinds of n-type semiconductor electrodes. In the first part of this chapter, it was demonstrated that ECL of the $[\text{Ru}(\text{bpy})_3]^{2+}/\text{TPrA}$ system obtained on n-Si/SiO_x/Ni(1.5 nm) electrode under 810 nm illumination is at a rather low potential, 0.5 V vs. SCE, which is far smaller than 1.1 V vs Ag/AgCl on glassy carbon electrode. In addition, brighter ECL signal on n-Si/SiO_x/Ni was obtained than ECL on n-Si/SiO_x and can keep constantly for 15min, confirming that Ni layer can help to stabilize electrode and increase conductivity. As a comparison, ECL on non-photoactive p-Si/SiO_x/Ni(1.5 nm) without illumination is at 0.9 V, indicating that n-Si/SiO_x/Ni(1.5 nm) is in depletion with a flat band potential that is very cathodic with respect to the ECL onset potential. The upconversion process occurred in this PECL system, which combines photoactivation at SC with electrochemistry, gives a remarkably stable and intense ECL emission in water. This finding shows the recent developments on photoelectrode protection can be beneficial for applications outside energy, opening exciting opportunities in various fields such as ECL. This P-ECL job may find application for the design of new detection strategies, light-addressable systems, or infrared imaging devices. In the second part of this chapter, another n-type SC, BiVO₄ was introduced as the photoanode in the L-012/NaOH system by using a suitable light source for L-012 luminescence as well as generation of P-ECL. Because of the low oxidation potential of L-012 and the high photovoltage of the electrode and the chemical stability of BiVO₄, amplified luminescence induced by photogenerated holes on the surface of BiVO₄ photoanode under 375 nm illumination was observed when the applied potential is at as low as -0.4 V vs. Ag/AgCl. Brighter emission is obtained with a significant PECL contribution, which increases with the potential, to the overall light intensity. Due to the chemical stability of BiVO₄, PECL can be induced on the electrode surface at a low potential for several hours. This strategy can be employed to precisely tailor L-012 emission and this report constitutes

the first example of “fluorescence type” PECL where $\lambda_{\text{exc}} < \lambda_{\text{emi}}$. This P-ECL job may find potential applications in biosensing and light-addressable devices.

In total, the concept of P-ECL can be applied to other types of reactions (including cathodic ones) on a variety of absorbing n- and p-type SCs, and thus, a wide range of P-ECL systems with different absorption/emission characteristics should be readily accessible. Besides being beneficial in terms of electrochemical potential gain, the adaptable P-ECL systems coupled with suitable irradiation can be designed as new detection strategies or used for bio-analysis. As we all know, tissues are relatively transparent to near-infrared light, which can reduce the scattering of themselves in such wavelength region, thus, P-ECL concept with up-conversion system can be developed for biomedical imaging.

In chapter 3, electrochemiluminescent enantiomeric discrimination is introduced on chiral imprinted Pt-Ir alloys electrode for the first time. The selected amino acid, L and D-PA enantiomers used as chiral compound and the co-reactant to generate the stereoselective emission of ECL signals in $[\text{Ru}(\text{bpy})_3]^{2+}/\text{PBS}$ system were discriminated by ECL difference on PA imprinted mesoporous Pt-Ir alloys. Enantioselective adsorption of chiral molecules on metal surfaces is controlled by the chirality of the recognition sites imprinted in metal alloys structure, thus, leading to the difference in ECL signals. These chiral-imprinted mesoporous metals combined with mesoporosity which can improve mass transportation, and with recognition sites can enhance preferable molecule lifetime to increase ECL intensity, demonstrated efficient enantiomeric discrimination through ECL sensitivity difference and outstanding stability after many catalytic cycles. This strategy illustrates the power of using an ECL-based readout, extending the application of ECL technique and this concept as a chiral detection introduces many advantages, like simply operated, low background signal, high sensitivity with low concentration. This concept overcomes many limitations of other techniques, like high cost for advanced instrumentations, time-consuming analytical processes and so on.

The finding of these first proof-of-principle experiments open up interesting perspectives for the development of other molecular encoded metal structures able to be used for such an optical detection. Besides, it can be developed as an effective detection technique for discrimination of enantiomers in (bio)analysis, food and environment investigations.

Acknowledgements

It is memorable to have four years PhD study in Bordeaux, France, which will be a precious experience in my life. I am the second Chinese student in the NsysA group supported by the China Scholarship Council (CSC) and University of Bordeaux Ph.D program. I would like to thank my supervisor Prof. Neso Sojic, not only for the continuous support in the study and research but also for help in life. He is patient, knowledgeable, motivated, enthusiastic. His guidance and the manner of thinking for researching helps me in all the time of research and writing of this thesis, also guide me subtly to renew the thinking way for doing research.

I deeply appreciate the collaborations with Gabriel Loget. Thanks for his ideas, helpful discussions, paper writing, let me improve quickly and get many publications on the new topic related to ECL. Therefore, I am not only focused on ECL, but learn other topics, become more flexible on researching after 4 years. And also thanks Yiran Zhao and other colleagues in the Institute of Chemical Sciences for the work of photo-electrochemiluminescence. My first PhD lecture about electrochemistry was with Prof. Alexander Kuhn, his lectures was passionate and understandable. He is a knowledgeable professor who I show deep respect from heart. Also thanks his guidance and collaborations for the last work in thesis. Hope one day I can be a knowledgeable person like him or like my supervisor. Thanks Sopon Butcha, the best Tai friend for doing collaboration and many contributions on the last work in thesis.

For the NsysA family, I want to thank all members in the lab. It is a pleasure to work with all of you. I would like to thank Dr. Zhanglin and Silvia Voci, who are the persons of the group that I met at the first time and helped me to deal with the problem of a apartment; thanks to Dr. Silvia Voci who led and taught me to use many instruments, like Photomultiplier, ECL spectrometer, UV-Vis absorption spectrometer and so on; thanks to Gerardo Salinas for teaching me fundamentals of electrochemistry and all the helps from him; thanks Mohsen for modification and comments for my thesis and always nice to me. Thanks to Patrick Garrigue and Stephane Reculosa for their technical supports on HF and Nova,spectrometer and other helps; thanks to Dr. Laurent Bouffier for teaching me UV-vis spectrum and fluorescence spectrometer knowledge; thanks to Véronique Lapeyre for helping me order chemicals; thanks to Aline Simon-Lalande and Laëtitia Debord for the administration works in the lab.

Thanks to all my colleagues in NsysA group, Sunpet Assavapanumat and Maciej Mierzwa for directing me many points for living, thanks to all Tai friends, Sapon butcha, Marisa Ketkaew, Thitapond, Aoy, Best, Dan and Fond for kind smiles and many helps to me. Thanks Lea, Julie, Youness and Remi for sharing and teaching me French.

For my family, to my parents, I thank both for raising me and supporting me no matter where I am. It is first time for leaving far from home and feel sorry for the absence of accompanying with my parents.

For my friends, thanks my good beautiful friends Wenjuan Wang and Mengjia Wang for support and accompany. Thanks to my roommates Xiaojun Li, Jialun Zhou and my friend Xinhao Zou for supporting and helping me in my whole PhD, especially in the quarantine time in 2020 which is the darkest period. Also thank Junjin Che, Xinyi Liu, Tingting Zhang, Lu Zhao, Chunxiao Lv and MengLiu for helping me at that time. Thanks to all my Chinese friends in Bordeaux, in China, France and Europe.

Hope friends, all colleagues, my family and me all have a good future and magnifique life.